Static and Ultrafast Optical Response of Metal-Semiconductor Hybrid Nanostructures

By

Sabina Gurung

PHYS03201504003

Raja Ramanna Centre for Advanced Technology, Indore

A thesis submitted to the

Board of Studies in Physical Sciences

In partial fulfillment of requirements

for the Degree of

DOCTOR OF PHILOSOPHY

of

HOMI BHABHA NATIONAL INSTITUTE

March, 2021

Homi Bhabha National Institute[1]

Recommendations of the Viva Voce Committee

As members of the Viva Voce Committee, we certify that we have read the dissertation prepared by Ms Sabina Gurung entitled "Static and Ultrafast Optical Response of Metal-Semiconductor Hybrid Nanostructures" and recommend that it may be accepted as fulfilling the thesis requirement for the award of Degree of Doctor of Philosophy.

Chairman - Dr. Aparna Chakrabarti	Aparna Chakrabarti 29.06.2021
Guide / Convener - Dr. J. Jayabalan	
Examiner - Dr. P. K. Datta	
Member 1- Dr. T. K. Sharma	
Member 2- Dr. A. K. Sinha	
Member 3- Dr. M. K. Chattopadhayay	29-06-2021
External Expert Member- Dr. G. Ravi Kumar	29/6/2021.

Final approval and acceptance of this thesis is contingent upon the candidate's submission of the final copies of the thesis to HBNI.

I/We hereby certify that I/we have read this thesis prepared under my/our direction and recommend that it may be accepted as fulfilling the thesis requirement.

Date: 01-07-2021 NA

Place: Indore **Signature** **Signature**

Co-guide (if any) **Guide**

---

[1] This page is to be included only for final submission after successful completion of viva voce.

STATEMENT BY AUTHOR

This dissertation has been submitted in partial fulfillment of requirements for an advanced degree at Homi Bhabha National Institute (HBNI) and is deposited in the Library to be made available to borrowers under rules of the HBNI.

Brief quotations from this dissertation are allowable without special permission, provided that accurate acknowledgement of source is made. Requests for permission for extended quotation from or reproduction of this manuscript in whole or in part may be granted by the Competent Authority of HBNI when in his or her judgment the proposed use of the material is in the interests of scholarship. In all other instances, however, permission must be obtained from the author.

SABINA GURUNG
Sabina

Name & Signature
of the student

DECLARATION

I, hereby declare that the investigation presented in the thesis has been carried out by me. The work is original and has not been submitted earlier as a whole or in part for a degree / diploma at this or any other Institution / University.

SABINA GURUNG

Sabina

Name & Signature

of the student

List of Publications Arising From The Thesis

Journals

1: "The optical response of self-organized Ag-CdTe metal-semiconductor hybrid nanostructures: Change in interaction vs number density variation", **Sabina Gurung**, Asha Singh, Rama Chari, J Jayabalan, Journal of Applied Physics, **2018**, 124(20), 204305.

2: "Counting the Electrons Hopping in Ultrafast Time Scales in an Ag–CdTe Hybrid Nanostructure", Asha Singh, **Sabina Gurung**, Rama Chari, J. Jayabalan, The Journal of Physical Chemistry, **2019**, 123(47), 28584-28592.

3: "Static and Ultra- fast Optical Response of Two Metal Nanoparticles Glued with a Semiconductor Quantum Dot,", **Sabina Gurung**, Asha Singh, Durga Prasad Khatua, Himanshu Srivastava, J Jayabalan, Photonics and Nanostructures-Fundamentals and Applications, **2020**, 43, 100869.

4: "Ultrafast Carrier Dynamics in Ag-CdTe Hybrid Nanostructure: Non-radiative and Radiative Relaxations", **Sabina Gurung**, Durga Prasad Khatua, Asha Singh, J Jayabalan,Journal of Physics: Condensed Matter, **2021** 33 (18), 185702.

5: "Effect of Spectral Overlap and Mixing Ratio on the Photoluminescence Kinetics of CdTe Quantum Dot in Metal-Semiconductor Mixed Colloid", **Sabina Gurung**, Asha Singh, J Jayabalan, (Under Review).

6."Electromagnetic Response of Metal-Semiconductor Hybrid Nanostructures", **Sabina Gurung**, J Jayabalan, (Manuscript under preparation).

Conferences

7: "Effect of Silver Nanoparticle on the Normal Photoluminescence and Upconversion Photoluminescence of CdTe Quantum Dots", **Sabina Gurung**, Asha Singh, J. Jayabalan, Salahuddin Khan, and Rama Chari, National Laser Symposium-25, **2016**.

8: "Ultrafast charge carrier transport in a metal-semiconductor hybrid nanostructure and its effect on transient absorption signal", **Sabina Gurung**, Asha Singh, Rama Chari, and J. Jayabalan, ULTRAFAST SCIENCES , **2018**.

9: "Signature of particle-particle interaction in plasmon peaks of Ag-CdTe hybrid nanostructures", **Sabina Gurung**, Asha Singh, Rama Chari, and J. Jayabalan, The International Conference on Fiber Optics and Photonics – PHOTONICS, **2018**.

SABINA GURUNG

Sabine

Name & Signature

of the student

To, Geeta Gurung

"Thank you for your endless love, sacrifices, prayers, support and advices."

This thesis is proudly dedicated to my mother.

All that I am, or hope to be, I owe to my mother.

Sabina Gurung

ACKNOWLEDGEMENTS

First and foremost, I would like to express my gratitude to my supervisor Dr. J. Jayabalan for guiding me since day 1 and providing me with wonderful research environment. Dr. Jayabalan's skilful guidance, innovative thinking and constructive criticisms have always helped me develop the scientific integrity, approach and communication in an efficient manner. I greatly appreciate his patience (lots of it) throughout my Ph.D. period. I am also extremely thankful to Mrs. Asha Singh for her valuable input that helped to shape this thesis alongwith her continuous support, and encouragement. I would like to thank Dr. Sallaudin Khan for his valuable suggestions whenever needed. I thank Dr. Tarun Kumar Sharma and Dr. Rama Chari for fruitful discussions and constant support in both academic as well as administrative work, as my section head. I express my gratitude to my doctoral committee members, Dr. Aparna Chakrabarti, Dr. T. K. Sharma, Dr. A. K. Sinha, Dr. M. K. Chattopadhyay, and Dr. G. Ravi Kumar and acknowledge their valuable suggestions through out my annual progress presentations. I would also like to thank our deans, Dr. C. P. Paul and Dr. Arup Banerjee, for their support throughout. I thank my senior Arijit Chakrabarti for his guidance and my junior Durga Prasad Khatua for constantly being there for me. I would like to acknowledge HBNI and Director, RRCAT for the financial support. These acknowledgement would not be complete without mentioning my friends in hostel and sitting place, Dhanshree, Preeti, Ramjan, Shantanu, Charu, Mangalika, Azam, Sabyasachi, who gave me collection of memories from this journey.

Above all, this would not have been possible for me to achieve without the encouragement and support from Mr. Monee Ram Rai who always stood beside me and my family. Lastly, no words are enough to thank my mother for her love and sacrifice.

Sabina Gurung

Contents

List of Figures

List of Tables

Chapter 7

Conclusion

In this thesis, optical properties of specially designed and sythesized metal-semiconductor hybrid nanostructure (HNS) has been studied. Specifically the dependence of static and ultrafast optical properties of the hybrid on the shape and size of the constituent nanoparticles and the ratio between number of metal nanoparticles (MNP) and semiconductor quantum dot (SQD) in a given HNS. Both experimental and theoretical methods were used for this purpose. The general methodology used was to synthesize the individual component of HNS i.e. MNP and SQD, by wet chemical method and then form different HNSs by mixing them in certain number density ratio. The number density ratio was chosen such that the final HNS formed is stable. Once a given HNS colloid is formed, its static response like absorption and PL spectra were measured and compared with that of the individual colloidal constituent that are used to form the HNS. These results were then compared with that of theoretically modelled, to understand the effect of synergistic interaction like charge transfer, energy transfer, electromagnetic interaction, etc on its optical properties. A single type of metal (Ag) and semiconductor (CdTe) was chosen so that the effect of the shape, size and number of density ratio on the final optical property of HNS could be studied.

Since there was neither theory nor an experimental method reported earlier to form unique HNS colloid, therefore first such theory was developed. This theoretical prediction was then confirmed by experiments to grow stable and unique HNS colloids. This was done by first showing that colloids prepared by mixing MNP and SQD colloids at different number density ratios result in a mixture composed of a single MNP-SQD hybrid and one kind of unattached original particles. With this, it has been shown that the properties of hybrid samples prepared by such self-organized growth are decided by the variation in number density of the hybrid and the unattached particles and not due to a continuous change in the interaction between MNP and SQD as was assumed earlier. This method has enabled preparation of specifically designed Ag-CdTe structure of various types and allowed structural characterisation of self-organised HNS by optical measurements itself. These studies are crucial for the advancement in the area of colloidal self-organisation.

Using this result, we prepared a specific HNS such that there are two Ag NPs per CdTe QD. The extinction spectra measured during growth suggests that the final HNS have two touching Ag NP and a CdTe QD in between them close to the point of contact. Typically it was always thought first one has to bring two Ag NPs close to each other to form the hot spot and then place the SQD at that location. The technique presented here to place CdTe QD at the hot spot is completely reverse. Here the two Ag NPs were brought together and glued by the CdTe QD there by forming large number of Ag\CdTe/Ag HNS by self-assembly. This method of placing the SQD could be used to form similar structures using any metal and semiconductor combination thus finds wide application towards harnessing the enhanced field for various applications. By the very nature of structure itself, the Ag\CdTe/Ag HNS is expected to show a strong plasmonic response. This was conformed by comparing the calculated plasmonic optical response with that of the measured. Ultrafast transient measurements also showed that the response of Ag\CdTe/Ag to a short pulse is majorly plasmonic. However, it was demonstrated that the presence of CdTe QD strongly influences the dynamics when the probe excites the gap plasmon. This is because the probe field gets enhanced in the gap plasmon and sense the presence of CdTe QD. The plasmonic response was so dominant in this structure that the CdTe

QD could not show any measurable photoluminescence (PL). On the other hand, a HNS with more number of CdTe QD compared to Ag NP should also be able to emit PL.

An Ag-nCdTe HNS formed by each Ag nanosphere covered by CdTe QDs could show PL. The emission strength as well as spectrum of the PL from the HNS was very different compared to that of bare CdTe QDs. The structure also allowed studies on the origin of radiative and non-radiative ultrafast optical response when Ag NP and CdTe QD interacts in a HNS. The ultrafast transient transmission of HNS, when excited near to LSPR, showed a faster recovery of hot electrons at a shorter time scale (few picoseconds) while it showed a slower recovery at longer time scale (few tens of picoseconds). This is because of the dominance of plasmonic response of MNP in the shorter time scale and dominance a band-filling effect in CdTe QDs at longer time. Further it was also found that the contribution of CdTe QDs to the transient transmission was increased in the presence of Ag NP due to hot-electron transport and local field enhancement by Ag NP. The underlying mechanism of non-radiatiave and radiative relaxation in this HNS was also compared to that theoretically calculated using electromagnetic theory, two-temperature model and hot-electron transport. This work provided significant insight into the various relaxation processes and contribution of charge transport to its optical response and PL quenching mechanisms in metal-semiconductor hybrids.

Transfer of hot-carriers from the metal to semiconductor (or vice versa) has been observed in various HNSs. Several such charge transport were also observed to happen in ultrafast timescales and thus it was not straight forward to quantitatively estimate the number of carriers. It is well known that the plasmonic response of metal strongly depends on the density of carriers. Thus probing the plasmonic response of metal should give quantitative information about the charge transport between metal and semiconductor HNS. To quantify the charge transport in HNS, we prepared a specific HNS having a plasmon resonance well below the band gap of the CdTe QDs. This structure allowed selective excitation of plasmon resonance with hot-carrier transport from MNP to SQD and back to MNP. Using Drude model and the changes in the number density of free electrons, we found that the transient optical response of the hybrid is governed by both free-electron temperature and the number of carriers transported from or to the MNP. Using the linear absorption spectra as reference, this measurement allowed estimation of the number of carriers hopping between the two constituents of the hybrid. The estimate of the number of electrons hopping at ultrafast time scales will provide a way to optimize the design of a metal-semiconductor hybrid system for specific applications. Studies on similar HNS showed that PL kinetic in HNS depends strongly on the excitation photon energy.

To conclude, this thesis presents a general protocol to synthesize hybrid nanomaterials with desired structures and provided an understanding of the interactions that creates synergistic effects in HNS. This has been achieved by growing several self-organized HNS and characterizing them using static and ultrafast spectroscopic measurements and linking the results to its structure. These results were also supported by suitable theoretical models. The future interest of this work involves utilization of these HNS colloids and the models for achieving plasmon modulated emission, hot-electron transport in optoelectronics, solar energy harvesting and photocatalysis.

Summary

Metal-semiconductor hybrid nanostructure (HNS) is an emerging paradigm for construction of advanced materials having multiple functionalities that are derived from synergistic interactions between metal nanoparticles (MNPs) and semiconductor quantum dots (SQDs). Appropriately designed HNS materials can show better performance as sensors, energy harvesters, efficient emitters and as better photocatalyst. In this thesis, it has been demonstrated that in a mixed colloid of MNP and SQD, the properties of hybrid samples prepared by self-organized growth is decided by the variation in number density of hybrid vs unattached particles and not due to a continuous change in the interaction between them. This allowed structural characterization of self-organized HNS by optical measurements itself. These studies are crucial for the advancement in the area of colloidal self-organization. Using this method, a semiconductor quantum dot could be placed between two Ag nanospheres in the hot-spot region. This assembly technique can be extended to other noble metals and semiconductor quantum dots capped with thiols. This is an important step for the applications of hot-spot. The underlying mechanism of ultrafast response in HNS is modelled using electromagnetic theory, two-temperature model and hot-electron transport. Each of these variation plays an important role depending on the structure of Ag-CdTe hybrid. To quantify the hot-electron transport in HNSs, a method is developed that estimates the number of electrons hopping between the two constituents of the hybrid at ultrafast time scales. This provides a way to optimize the design of a metal-semiconductor hybrid system for optoelectronic and catalytic applications. Photoluminescence (PL) spectroscopy on this HNS revealed that PL kinetics depends on the excitation photon energy when the PL emission spectrum overlaps with plasmom peak. This opens up possibility of designing a material that is well suited for light-emitting devices.

Chapter 1

Introduction

Artificially prepared materials that are structured in nanometer length scales are becoming increasingly important for several applications. This is due to the fact that the properties of such materials can be modified by appropriately structuring them in nanoscale. The method of modifying the properties can be used to improve the efficiency, sustainability and speed of the existing technologies. Semiconductor quantum dots (SQD) are an excellent candidate for optoelectronics and light-harvesting devices due to their suitable tunable fluorescence and absorption properties[1–3]. On the other hand, metal nanoparticles (MNP) have ability to manipulate light in nanoscale beyond diffraction limit[4]. Hence, it finds wide applications in surface-enhanced Raman scattering (SERS), scanning near-field optical microscopy (SNOM), metamaterials, etc[5–8]. At present, intense research is being carried out on metal-semiconductor hybrid nanostructures (HNS) since it is possible to design them to show superior properties that can supersede the combined function of individual material because of its synergistic behavior[9–14]. The optical response of a hybrid material depends on several factors like the energy difference between emission wavelength of SQD and localized surface plasmon resonance (LSPR) peak of MNP, the band alignment between metal and semiconductor, the shape and size of both the particles, the distance between them and their spatial distribution around each other[9–14]. Due to the role of such large number of parameters, the possible interaction mechanisms in HNS are still under intense research.

A MNP can enhance the electromagnetic field around it when excited at wavelength, close to its LSPR. Therefore, the light-matter interaction in a SQD can be enhanced by placing it near to the MNP. Such enhancement can increase the efficiency of semiconductor devices like photodetector, solar cells, LED etc [15–17]. It is also possible that charges excited in the MNP can move to the SQD and such charge transfer can further increase the efficiency of light harvesting devices[18–20]. Thus, appropriately designed HNS materials can be made to make use of advantages of both individual materials for better performance as sensors, energy harvesters, efficient emitters and photo-catalysts[8, 12, 17, 21–30]. However, for designing such hybrid material targeted towards a specific application, it is essential to understand the possible interactions between the individual constituents. In the following segments, we will discuss the fundamentals of optical response of MNP and SQD.

1.1 Optical Response of Metal Nanoparticles

When a small MNP of arbitrary shape is embedded in a transparent host medium, the field distribution around the MNP and the field inside the particle are much different from that of the applied field due to the dielectric confinement. Such confinement can lead to resonances called as the LSPR. The number of LSPR peaks as well as its peak wavelength depends on the dielectric constant of the particle and host medium, shape and size of the particle, its orientation with respect to the applied field and distribution of particles in host medium[31–34].

The local field distribution in and around a spherical particle in presence of static field can be calculated by solving Laplace's equation along with the dielectric constants of the particle and the host. The results obtained with the static solution can also be used for non-static electromagnetic fields provided that the wavelength of the light is much larger than the size of the particle. Static solutions for the optical response of particles are limited only to few other shapes like coated spheres, ellipsoids, infinite rods, etc. The complete solution for the optical response of a spherical particle of arbitrary size derived using Maxwells equation is given by Mie theory[31, 35]. Currently, it is also possible to grow several other shapes like cubes, rods, thin particle having triangular or hexagonal cross-sections, etc[34, 36]. There are no analytic theory for estimating the optical response of such structures and one has to rely on numerical techniques. Different numerical techniques like finite element methods, coupled dipole approximation and discrete dipole approximations can be used for calculating the optical response of an arbitrary-shaped particle of any size [32, 37].

1.1.1 Optical response of a small dielectric sphere

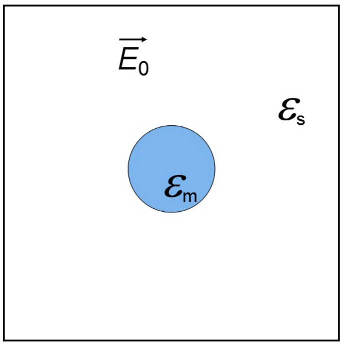

FIGURE 1.1: Schematic of a single dielectric sphere of dielectric constant ϵ_m embedded in a host medium of dielectric constant ϵ_s.

Consider a small homogeneous, isotropic and linear spherical particle of radius R and a dielectric constant ϵ_m, embedded in a medium of dielectric constant ϵ_s as shown in Fig.1.1. Let $\vec{E}_0 = E_0\hat{z}$, be the uniform static field applied on this particle. Using Maxwells equation, the potential inside the sphere can be written as,

$$V_{in} = -\left(\frac{3E_0\epsilon_s}{\epsilon_m + 2\epsilon_s}\right) z. \tag{1.1}$$

The corresponding electric field inside the particle is,

$$\vec{E}_{in} = \frac{dV_{in}}{dz}\hat{z} = \frac{3E_0\epsilon_s}{(\epsilon_m + 2\epsilon_s)}\hat{z}. \tag{1.2}$$

Thus, the field inside a small dielectric sphere embedded in a medium is constant and is proportional to the applied field. Further, if the dielectric constant of the sphere and the medium are such that $(\epsilon_m + 2\epsilon_s)$ is very small, then the electric field inside the medium can have much larger magnitude than that of the applied. In fact, this condition leads to the origin of LSPR in case of MNP embedded in a transparent host medium [31]. The potential outside the sphere can be written as,

$$V_{out}(r,\theta) = -E_0 z - \frac{1}{4\pi\epsilon_s r^3}\left[4\pi\epsilon_s R^3\left(\frac{\epsilon_s - \epsilon_m}{\epsilon_m + 2\epsilon_s}\right)E_0\right]z. \tag{1.3}$$

The above expression for the electric potential outside the sphere is identical to that of a ideal dipole with a dipole moment $\vec{p}$ given by,

$$\vec{p} = 4\pi\epsilon_s R^3\left(\frac{\epsilon_s - \epsilon_m}{\epsilon_m + 2\epsilon_s}\right)\vec{E}_0 \tag{1.4}$$

Thus, in a static electric field, a small dielectric sphere acts as a dipole having polarizability,

$$\alpha_s = 4\pi R^3\epsilon_s\left(\frac{\epsilon_m - \epsilon_s}{\epsilon_m + 2\epsilon_s}\right). \tag{1.5}$$

Using the Eq.1.3, the field outside the particle can be written as,

$$\vec{E}_{out} = E_0\left(1 + \frac{R^3(\epsilon_s - \epsilon_m)}{r^3(\epsilon_s + 2\epsilon_s)}\right)\hat{z}. \tag{1.6}$$

Figure 1.2 shows a typical field distribution near a small dielectric sphere which is similar to a dipole. If the sphere itself is considered as a collection of tiny dipoles,

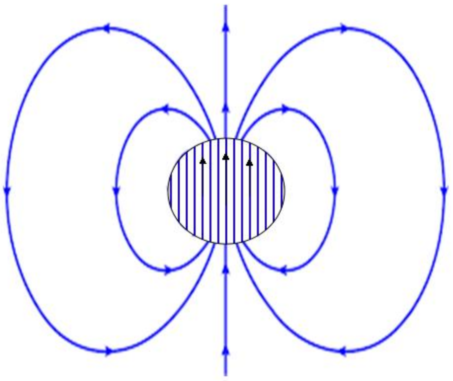

FIGURE 1.2: Field distribution in and around a dielectric sphere in static field approximation.

then the dipole moment of the sphere is given by,

$$\vec{p} = V\vec{P} \tag{1.7}$$

where V is the volume of the sphere and $\vec{P}$ is the polarization of the medium outside the sphere. Then

$$\vec{p} = V(\epsilon_m - \epsilon_s)\vec{E}_{in} \tag{1.8}$$

Therefore, the polarizability outside the sphere is,

$$\alpha_s = 3\epsilon_s V \left(\frac{\epsilon_m - \epsilon_s}{\epsilon_m + 2\epsilon_s} \right) \tag{1.9}$$

Thus, both the internal and external field distribution leads to the same expression for polarizability of a small sphere.

So far in this calculations, a uniform static field approximation was used for the estimation of the response of the sphere. Using this, we found that the response of the small particle to the applied field is same as that of a tiny dipole. Thus if the applied electric field is uniform over the particle, the same equations can be used even for a time varying electromagnetic field. In such cases the wavelength of the light has to be much larger than the size of the particle such that the whole particle experiences a uniform field at a given moment. This approximation is called as the quasi-static approximation.

In comparison with a point dipole, the cross-sections for the extinction, scattering and absorption by a single small sphere can be written as[31],

$$\begin{aligned} C_{ext} &= kIm\{\alpha_s\}, && (1.10) \\ C_{sca} &= \frac{k^4}{6\pi}|\alpha_s|^2, \text{ and} && (1.11) \\ C_{abs} &= C_{ext} - C_{sca}, && (1.12) \end{aligned}$$

respectively. Here, $k = 2\pi n/\lambda$ with n as the refractive index of the host medium and λ is the free space wavelength of light used.

In case of spherical particles, due to its spherical symmetry, the polarization is independent of its direction to the applied field polarization. However, for an asymmetric object, the polarization will strongly depend on the direction of the applied field with respect to the object. Thus, the electronic polarizability ,α, of such particle is no more independent of direction as in the case of sphere but can become a tensor. Even if a particle is spherical but if the dielectric constant of the material that forms the sphere is not isotropic, the particle polarizability has to be defined as a tensor. In the following we show one such case of common nonspherical particles, ellipsoid.

Ellipsoid

For ellipsoid, the three principal axis can always be chosen along the diameters of the ellipse such that, with respect to principle axis, the dielectric tensor has only three components that are non zeros as shown in Fig.1.3.

$$\alpha = \begin{bmatrix} \alpha_x & 0 & 0 \\ 0 & \alpha_y & 0 \\ 0 & 0 & \alpha_z \end{bmatrix} \tag{1.13}$$

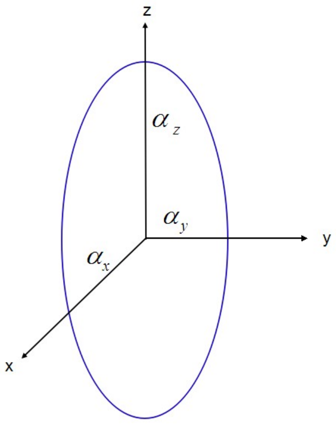

FIGURE 1.3: Various components of polarizability of a ellipsoidal particle.

When the electric field is applied to an ellipsoidal material, dipole is induced in it. Let us assume that the size of the ellipsoid is such that it satisfies quasi-static approximation in all three directions. The polarizability of the ellipsoid can be calculated by solving Laplace's equation but using ellipsoidal coordinates. From the solutions the polarizability component of the ellipsoid in x direction is given by [31],

$$\alpha_x = \frac{4\pi a_x a_y a_z}{3}(\epsilon_m - \epsilon_s)\left(\frac{\epsilon_s}{\epsilon_s + L_x(\epsilon_i - \epsilon_s)}\right), \tag{1.14}$$

where L_x is the depolarization factor given by,

$$L_x = \frac{a_x a_y a_z}{2}\int_0^\infty \frac{ds}{(s+a_x^2)\sqrt{(s+a_x^2)(s+a_y^2)(s+a_z^2)}}, \tag{1.15}$$

where a_i's are the radius of ellipsoid in ith direction. The depolarization factors for the other two directions, y and z, are also defined in the similar way and obey the relation $L_x + L_y + L_z = 1$.

1.1.2 Optical Response of Collection of Small Particles

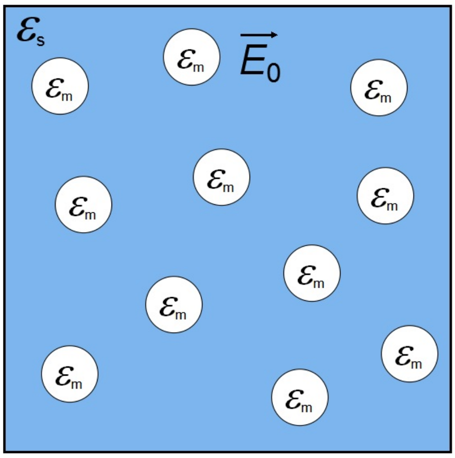

FIGURE 1.4: Schematic of dielectric spheres of dielectric constant ϵ_m embedded in a host medium of dielectric constant ϵ_s.

In the previous section, we have shown that a small dielectric sphere in the quasi-static approximation behaves as a dipole. Let us consider a medium consisting of several such small spheres of a different material as shown in Fig.1.4. Let ϵ_m be the dielectric constant of the material of the sphere and ϵ_s be the dielectric constant of the host material. In order to treat this composite as a smooth dielectric medium, it is essential to introduce the concept of volume averaged fields.

When an uniform field is applied in this material, as we have discussed earlier, the actual field experienced by a sphere may not be same as that of applied. This is due to the fact that the field experienced by a sphere at a given location has the contribution from the field induced by all the other spheres and the applied field. . Let $\vec{E}_s$ be the field inside the host medium. However, if the spheres are distributed sufficiently far away from each other then using Eq.1.2, the field inside the sphere, $\vec{E}_m$, can be written as,

$$\vec{E}_m = F\vec{E}_s, \tag{1.16}$$

where

$$F = \frac{3\epsilon_s}{(\epsilon_m + 2\epsilon_s)}, \tag{1.17}$$

where F is the local field factor which is defined as the ratio between the field inside a sphere to that of applied in the surrounding medium.

Assuming that the distribution of spheres in this medium is such that if we consider a sufficiently large volume, the average behavior of the medium remains same. In such case, it is possible to define a effective macroscopic permittivity for the medium (ϵ_{eff}) (in the same way as that we defined for dielectric medium containing molecules) such that

$$\left\langle \vec{D} \right\rangle = \varepsilon_{eff} \left\langle \vec{E} \right\rangle \tag{1.18}$$

here the $\langle\rangle$ represents an average over a large enough volume such that the local variations in the field can be averaged out. Let f be the fraction of the volume occupied by the spheres in the medium under consideration, then (1-f) is the fraction of volume occupied by the host medium. The average field inside the medium can be estimated by the weighing it with respect to the volume fraction. Thus the averaged flux density and electric field can be written as [38],

$$\left\langle \vec{D} \right\rangle = f\epsilon_m \vec{E}_m + (1-f)\epsilon_s \vec{E}_s \text{ and} \tag{1.19}$$

$$\left\langle \vec{E} \right\rangle = f\vec{E}_m + (1-f)\vec{E}_s, \tag{1.20}$$

respectively. Substituting these in Eq.1.18 and using Eq.1.17, we can arrive at an expression for the dielectric constant of the effective medium as

$$\epsilon_{eff} = \epsilon_s + 3f\epsilon_s \frac{\epsilon_m - \epsilon_s}{\epsilon_m + 2\epsilon_s - f(\epsilon_m - \epsilon_s)}. \tag{1.21}$$

This equation, which defines the effective dielectric constant in terms of the dielectric constants of inside material and the volume fraction, is called as the Maxwell

Garnett mixing formula [38]. For low volume fractions, $f << 1$, we can write,

$$\epsilon_{eff} \approx \epsilon_s + 3f\epsilon_s \frac{\epsilon_m - \epsilon_s}{\epsilon_m + 2\epsilon_s}. \tag{1.22}$$

In general, the host medium used in nanocolloid is transparent (non-absorbing) hence the imaginary part of ϵ_s is zero. However, the inclusions can be absorbing, hence the ϵ_m has both real and imaginary parts:

$$\epsilon_m = \epsilon'_m + i\epsilon''_m. \tag{1.23}$$

In such cases, the ϵ_{eff} also becomes complex and we can write,

$$\epsilon_{eff} = \epsilon_s + 3f\epsilon_s \frac{[(\epsilon'_m - \epsilon_s)(\epsilon'_m + 2\epsilon_s) + (\epsilon''_m)^2]}{(\epsilon'_m + 2\epsilon_s)^2 + {\epsilon''_m}^2} + i\frac{9f\epsilon_s^2\epsilon''_m}{(\epsilon'_m + 2\epsilon_s)^2 + {\epsilon''_m}^2}. \tag{1.24}$$

The absorption coefficient of a material is related to the imaginary part of dielectric constant and is given by,

$$\alpha = \frac{\omega}{c\sqrt{\epsilon_s}} \operatorname{Im}(\epsilon_{eff}), \tag{1.25}$$

where ω and c is the angular frequency and velocity of light, respectively. Thus for the effective medium, the absorption coefficient can be written as

$$\alpha = \frac{18\pi f \epsilon_s \sqrt{\epsilon_s}}{\lambda} \frac{\epsilon''_m}{(\epsilon'_m + 2\epsilon_s)^2 + {\epsilon''_m}^2}, \tag{1.26}$$

1.1.3 LSPR of Ag nanospheres in water

As an example, let us consider the case of small silver spheres dispersed in water. As noted from Eq.1.26, to calculate the wavelength dependent absorption coefficient of this composite medium, we should know the volume fraction of silver in water and the dielectric constants of the Ag NP and water. For large particle, size of the bulk dielectric constant could be directly used for this calculation. Figure

1.5(a) shows the experimental bulk dielectric constants of silver and water[39] and Fig.1.5(b) shows the calculated normalized absorption coefficient of Ag nanospheres dispersed in water. A single peak in the absorption coefficient occur at the wavelength when the real part of dielectric constant of silver (ϵ'_m) becomes equal to $-2\epsilon_s$ and the denominator in Eq.1.26 becomes zero. This resonance is called as the LSPR. Generally, LSPR occurs in the visible regime in metal NP since the real part of dielectric constant of metal can be negative in that regime. Recall that at $\epsilon'_m + 2\epsilon_s = 0$, the field inside the particle is much larger than the applied (Eq.1.16). Thus, although the silver has a low absorption coefficient at the LSPR wavelength, due to the dielectric confinement, the field inside the particle becomes large which inturn leads to large absorption by the particle, giving rise to LSPR.

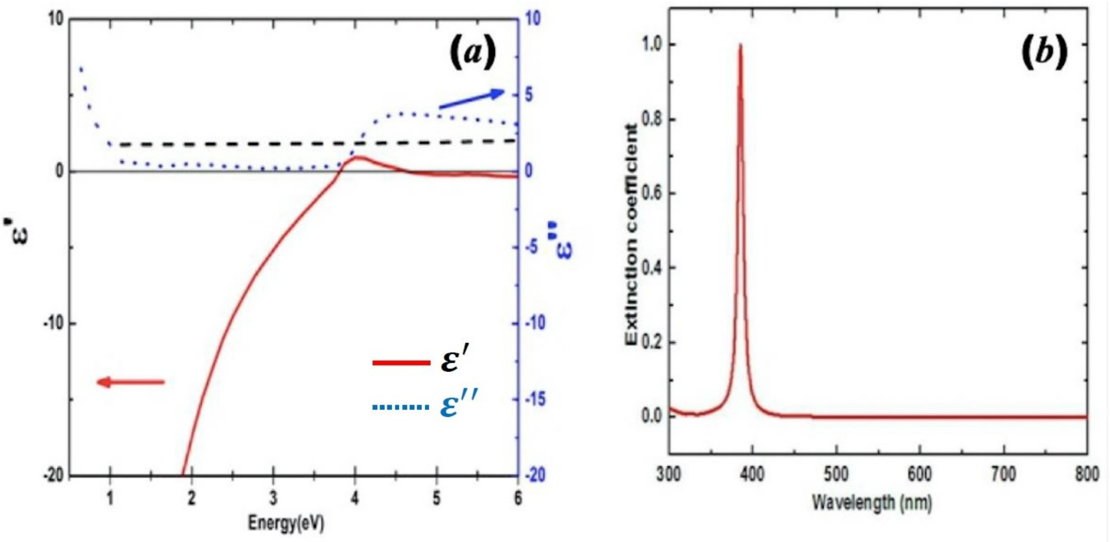

FIGURE 1.5: (a) Experimental bulk dielectric constants of Ag and water in the visible regime. (Ag real part: left axis; Ag imaginary part: right axis; Water: left axis) (b) Normalized absorption coefficient of silver particles dispersed in water calculated by using Eq.1.26.

Figure 1.6(a) shows the extinction, scattering and absorption spectrum of a 3 nm Ag sphere in water, calculated using Mie theory. For particles of small size the contribution to the extinction from scattering is negligible. Thus, for particles of size much smaller than 30 nm, only a single peak appears in the visible spectrum which is nearly at 400 nm. For particles of such smaller sizes, Maxwell Garnett

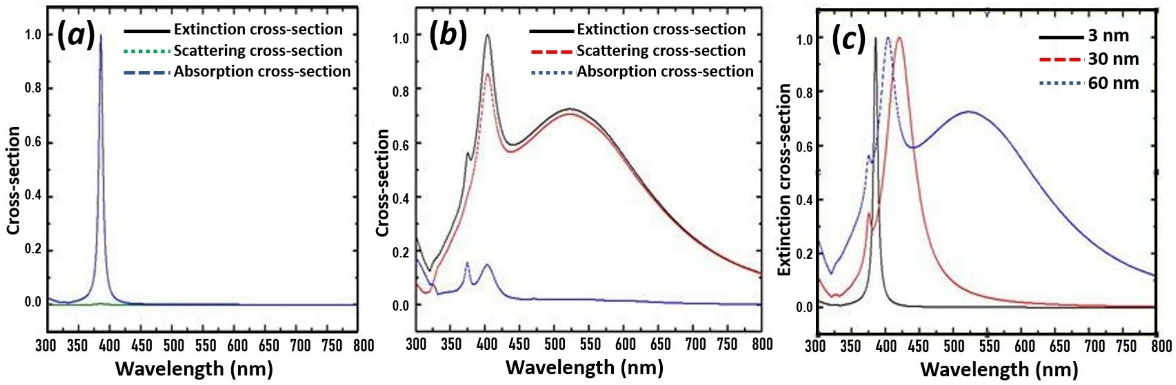

FIGURE 1.6: (*a*) The calculated extinction, absorption and scattering cross-sections of a 3 nm Ag particle in water. (*b*) The calculated extinction, absorption and scattering cross-sections of a 60 nm Ag particle in water. (*c*) The calculated extinction cross-section for Ag particle of size 3 nm, 30 nm and 60 nm immersed in water.

mixing formula can give the same result as that given by Mie theory. As the size of the particle increases, the contribution to the extinction from scattering increases. Figure 1.6(*b*) shows the absorption and scattering contributions to the extinction spectrum of a 60 nm Ag nanosphere in water. It can be observed that for larger spheres, the scattering efficiency dominates over the absorption efficiency. Figure 1.6(*c*) shows the comparison of extinction spectrum of some of the spherical Ag NPs of different sizes. As the size of the particle increases from 3 nm to 30 nm regime, the peak wavelength red-shifts. When the size of the particle is nearly 30 nm, an additional peak appears nearly at 370 nm in the spectrum which can be attributed to the higher order modes of sphere. For particles of this size, the Maxwell-Garnett mixing formula can no longer be used to predict the fine details in the absorption spectrum. This is because for larger sphere, the field distribution inside the particle is no more dipolar and has contribution from higher order modes. At even larger sizes, the number of modes increases along with the red-shift of the existing peaks in the spectrum.

1.1.4 Local field enhancement (LFE)

First generation LFE: As seen from Eq.1.17, when excited at LSPR, the MNP can significantly enhance the strength of electromagnetic field around them and such field enhancement is known as first generation LFE[31, 40]. First generation LFE can be as large as 20 times than that of the applied field and depends on wavelength, size and shape of MNP and their surrounding medium[41, 42]. By placing an analyte molecule at the high local field area created due to first generation LFE, the light matter interaction in analyte can be increased. Such first generation LFE opened up application of MNP in plasmonic sensing, optoelectronics, energy harvesting, nanolithography, nano-antennas and imaging[8, 17, 21–23, 43–46].

Second generation LFE: A second generation of local field enhancement can be realized when two MNPs are placed close to each other (dimer) with separation less than few nanometers. Excitation of the dimer at a specific wavelength with polarization along the line joining the centers of the two particles can excite a plasmon mode known as "gap plasmon"[47, 48]. When the gap plasmon is excited, the field in the gap between these two particles, known as the "hot-spot", can get enhanced by a factor of five orders of magnitude than that of the applied[49–51]. Theoretical studies on the generation of such high field using two MNPs of various size, shape, and orientation is being reported by various groups[51, 52]. Although dumble shaped MNP could be made experimentally, placing analyte like SQD at the hot-spot still remains a challenge. Thus, placing the analyte at the hot spot in the gap plasmon becomes challenging despite its potential application in energy harvesting and sensing applications.

1.2 Optical Response of Semiconductor Quantum Dot

Quantum dots, also known as artificial atoms, are particles of few nanometers in size that has electronic and optical properties different from that of its bulk counterpart.

Due to its very small size, QDs have bound, discrete electronics states like atoms and molecules. Over the past few decades, SQDs have become a valuable component in various optoelectronic application. When a photon is incident on SQD, the absorption of the photon will lead to the excitation of the system. Once excited, the system will tend to return back to the ground state by different relaxation processes both radiative and non-radiative[53]. The carriers excitation and relaxing in SQD depends on its size and plays an important role in deciding the efficiency of the optoelectronic devices like LED, laser diodes and light emission and light-harvesting applications [1–3]. Several methods are being attempted to enhance and control the photoluminescence (PL) emission kinetics of SQDs for the development of efficient optoelectronic devices[13, 54]. Therefore, it is essential to understand the origin the PL in SQD and how it varies with the size. To understand the effect of size of QDs on its properties, it is essential to first understand confinement effects in SQD and how the band gap or energy level distribution changes with the particle size.

1.2.1 Size Dependence of Band Gap

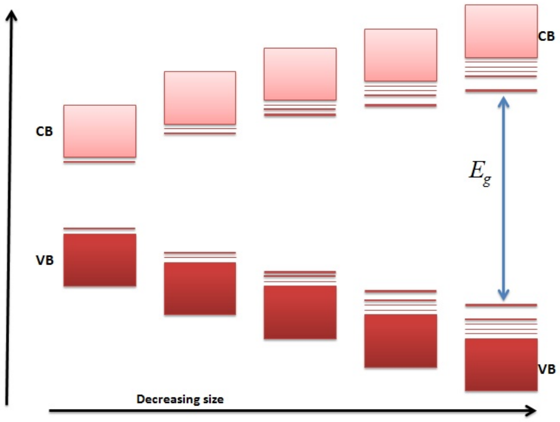

FIGURE 1.7: Schematic diagram showing the effect of reduction in size of a bulk semiconductor on the bang gap: Top-down approach.

The optical properties of SQD depends strongly on its size. This is primarily due to the size dependent bandgap of the SQD. In view of the top-down approach (schematic representation in Fig.1.7), the band gap energy of a QD of radius r is

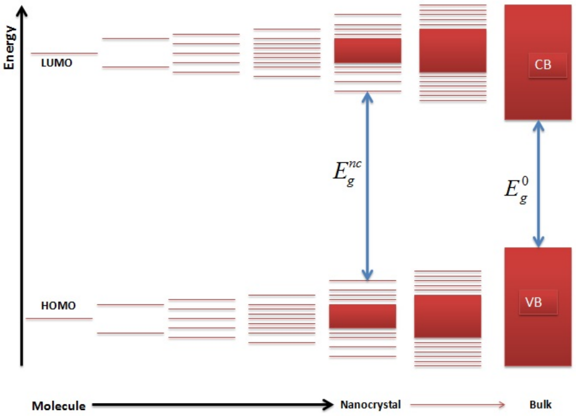

FIGURE 1.8: Schematic diagram showing the evolution of energy level from diatomic molecule to a bulk semiconductor: Bottom-up approach.

given by,

$$E_g(r) = E_g^0 + \frac{\hbar^2\pi^2}{2r^2}\left[\frac{1}{m_e^*} + \frac{1}{m_h^*}\right] - J_{e-h} + E_e^{pol} + E_h^{pol} - 0.248E_{Ry}^*, \qquad (1.27)$$

where,E_g^0 is the band gap energy of the bulk, the second term is the confinement energy of electrons and holes, J_{e-h} represents the effective coulomb interaction between electron and hole, E_e^{pol} and E_h^{pol} is the self polarization energy of the electron and hole respectively and E_{Ry}^* is the exciton Rydberg energy corresponding to spatial correlation between the electron and hole. Equation 1.27 describes the two important consequences of quantum confinements. First, the band gap energy of the QDs increases with decreasing size, as D^{-2}, when the coulombic interaction is negligible. Secondly, with quantum confinement, discrete energy levels arises at the edge of both conduction and valence band. These implies that by varying the size of the QD, the confinement energy can be varied and thus the optical band gap of QDs can be tuned as desired. Even if the QDs are viewed in terms of bottom up approach (schematic representation in Fig.1.8), we have seen that the gap between the HOMO and LUMO changes continuously with the size of the particle. Thus, as the size of the QDs decreases, the energy gap between highest level in valence band and lowest level in conduction band increases [55, 56]. Therefore more energy is needed to excite the electron and simultaneously, more energy is released when electron recombines with hole in the valance band.

1.2.2 Exciton

As mentioned earlier, in semiconductors, the absorption of light leads to an excitation of electron from the valence band to the conduction band, leaving behind a hole. In general, this electron and hole can experience a coulombic attraction which binds each other to form a hydrogen like atom, known as exciton. The main difference between a hydrogen atom and an exciton is the difference in the masses of carriers. First incase of hydrogen atom, mass of electron and proton are used while in case of exciton, effective masses has to be used. Further, in case of hydrogen atom, the electron mass m_e is very small compared to that of proton but in case of exciton, the effective mass of electron m_e^* is nearly equal to that mass of hole (m_h^*). Due to this difference, the centre of mass of the exciton lies nearly in between the hole and electron. Taking the analogy of the hydrogen atom, the most probable distance between the electron and hole in an exciton is defined as exciton Bohr radius and is given by,

$$a_0 = \frac{\hbar^2 \epsilon}{e^2} \left(\frac{1}{m_{ex}^*} \right), \tag{1.28}$$

where ϵ is the dielectric constant of the medium. The reduced effective mass of the exciton m_{ex}^* is defined as,

$$\frac{1}{m_{ex}^*} = \frac{1}{m_e^*} + \frac{1}{m_h^*}. \tag{1.29}$$

Further, the ionization energy of exciton is given by,

$$E_{ion} = -\frac{-m_{ex}^* e^4}{2\hbar^2 \epsilon^3} \frac{1}{n^2}, \tag{1.30}$$

where n is the quantum number that defines the energy state in with exciton is present.

1.2.3 Confinement Effects

In quantum dots the motion of electrons and holes are confined in all the three spatial dimensions [55–57]. The electronic properties of QD lies between those of bulk semiconductor and discrete atoms. The exciton Bohr radius a_0 is an appropriate length scale (given by Eq.1.28) to assess the impact of confinement in QD. The charge confinement in SQD can be categorized into different regimes:

1. Strong confinement regime: The QD radius, r, is smaller than the exciton Bohr radius, $r << a_0$. In this regime, the confinement energy dominates over the coulombic interaction between the electron and hole.
2. Weak confinement regime: The QD radius is much larger than the exciton Bohr radius, $r >> a_0$. The coulomb interaction is not negligible when compared to the confinement energy.
3. Intermediate confinement regime: The QD radius is larger than the hole Bohr radius but smaller than the electron Bohr radius.

1.2.4 Photoluminescence

In most semiconductors the excited electrons are free to move in the conduction band while the holes are free to move in the valence band at room temperature. With the excitation photon, if electrons are excited deep into the conduction band, the electrons relax to the lowest energy edge of the conduction band through generation of phonons. Once they reach the band edge, further non-radiative relaxation is not possible since there are no more close energy levels below the edge of the conduction band. Similarly, the holes in the valence band moves up until it reaches the top of

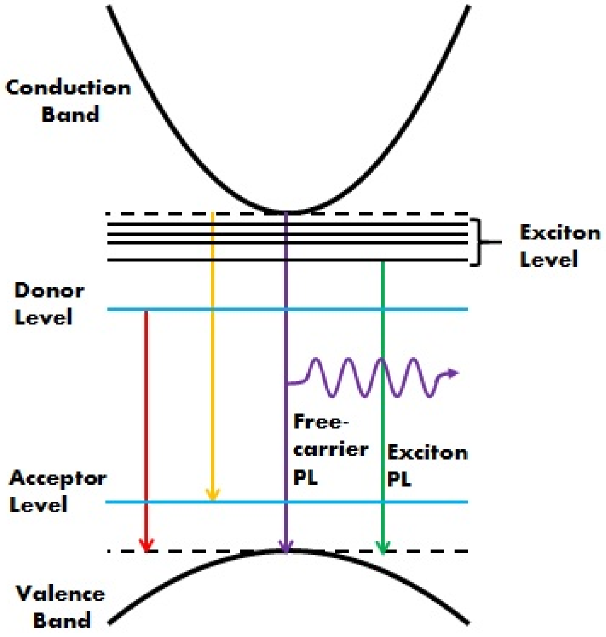

FIGURE 1.9: Schematic $E - k$ diagram and other possible energy states in a semiconductors. The various possible origin of photoluminescence (down arrows) is also shown.

the valence band. The free electron and free hole can recombine to emit photon which is equal to the energy gap between conduction and valence band. Origin of such emission is attributed to the free-carrier recombinations in semiconductor as shown in Fig.1.9. When an exciton is formed inside the semiconductor the energy of the electron hole pair is slightly lower than that of the free electrons and free holes (see Fig.1.9). The difference between these energies is given by Eq.1.30. The such electron-recombination also results in emission of photon but is slightly red-shifted when compared to the case of recombination of free electrons and holes [58, 59].

For example, in case of bulk GaAs the exciton binding energy is 4.8 meV and exciton Bohr radius is 11.6 nm, similarly in case of bulk CdTe the exciton binding energy is about 10 meV and the exciton Bohr radius is 6.8 nm. The thermal energy corresponds to room temperature is about 25 meV. Hence at room temperatures the excitons are broken and the electrons and holes are free to move independently. Thus, the PL from the bulk semiconductor samples at room temperature is most likely to be of free carrier origin. However, as the temperature is reduced, the PL from the sample smoothly blue-shifts due to the temperature dependence of band gap in semiconductors. At certain low temperature, the excitons would form when the thermal energy is not sufficient to break it. At this temperature, the measured PL from the sample will show a sudden red-shift. The origin of photoluminescence from the sample below this temperature is more due to the exciton recombination. In case of QDs, the electrons and holes are forced to interact with each other due to the confinement potential provided by the boundary of the particle [55, 57]. Thus, excitons can be observed in QDs even at room temperatures and the PL emission can originate from exciton recombination.

Lastly, in most cases, the material is always expected to have defects incorporated in them owing to the imperfections in the structural and chemical composition. The interaction between the defects and the trapped particles strongly affects the optical properties of the material. As the size of the semiconductor decreases, such interaction can also become stronger. The recombination of electron-hole pair via defect states can also result in emission of PL radiation (Fig.1.9).

1.3 Optical Response of Metal-Semiconductor Hybrid Nanostructures

It is possible to enhance the optoelectronic and light harvesting applicability of SQD when combined with LFE ability of MNP by placing them together to form metal-semiconductor HNS. However, the interaction between SQD and MNP can be complex due to the possible electromagnetic field interactions, charge exchange and electrostatic interactions[60–64]. Even, with a given combination of metal and semiconductor, it is possible to prepare several hybrid materials with very different properties by varying the shape and size of the individual materials, contact area and the separation between them[14, 62, 65–67]. Several types of hybrid for example core-shell, yolk-shell, Janus particles, heterodimers, etc have been developed in the past[68]. Self-organization method is one of the commonly used approach for building a wide variety of nanostructures because of its various benefits like scalability, flexibility in structural dimensions across orders of magnitude, highly stability as the process is self driven without any external perturbation and inexpensive. It is also possible to prepare HNS with different properties in a controlled manner by self-organization of the individually prepared nanostructures by optimizing the mixing ratio of MNP and SQD, changing the gap between them or by changing the linking molecule[66, 69–71]. In such HNS, a good control over shape and size of individual nanostructure is possible since well-established recipes exist for the preparation of SQDs and MNPs with excellent control over their size and shape by bottom-up techniques[6, 54, 72–74]. However, when the HNS forms by self-organization of MNPs and SQDs, correlating its properties to the possible structure which is forming in nanoscale becomes complicated. This is due to the fact that the number of MNPs and SQDs gets attached to form a single HNS for a given metal and semiconductor depend on the size, shape, and the properties of linking molecule. Several studies are being carried out to understand the properties of hybrid with an assumption that the mixing ratio would provide a way to control the interaction between MNP and SQD in nanoscale [20, 75, 76]. It has been reported that the presence of MNP can quench or enhance the PL and such changes depends on the mixing ratio of the MNP in SQD. Similarly, in the absorption spectrum, the exciton peak is wiped out while the defect state contribution also increases in incase of hybrid depending on the mixing ratio. However, there is no report on to establish a clear understanding of their properties when prepared under different mixing ratios, even for the case of linear optical response like PL and absorption. Further, the self-organized growth method lacks control over the final structure formed. In addition, formation of unique single HNS using self-organization growth method, is also not guaranteed. A development in the self-organization methods to form unique single structure would help in advancement of colloidal science.

The carrier dynamics that takes place between MNP and SQD plays a vital role in determining the final optical response of HNS[18, 77–79]. When a MNP is excited at its LSPR, LFE could be used for increasing absorption in a semiconductor that is placed close to the MNP thereby increasing the efficiency of light-semiconductor interaction[12, 24–29]. Hot electrons created in MNP can tunnel to the neighboring semiconductor thereby increasing its light harvesting efficiency. Similarly, carriers excited in SQD can go to MNP. Most of such carrier exchange happens at ultrafast time scales[63, 80–83]. At present lot of research is going on to understand such carrier exchange mechanisms. Most of such studies are being carried out by exciting the hybrid using an ultrafast pulse at a specific wavelength such that carriers are excited either in metal or in semiconductor[63, 80–83]. The consequent carrier dynamics in the hybrid is then studied at ultrafast time resolution to understand the charge exchange between the constituents. In case of isolated MNP, the ultrafast transient optical response could be explained by the increase in temperature of free electrons[84, 85]. On the other hand, in the case of isolated semiconductor QDs, it is explained by band to band absorption, band filling, inter and intra band relaxation, etc [86]. In semiconductor QDs, both radiative and non-radiative processes contribute to the total carrier dynamics, while in MNP only non-radiative processes contribute. Thus, the various dynamical processes that occurs in individual materials in HNS as well as their synergistic interaction complicates the understanding of its complete optical response. Nonetheless, it is important to comprehend the basic ultrafast interactions between these individual constituents for designing an HNS focused toward a particular application.

HNS can also allow a good control over the emission property compared to that of the constituent SQD[17, 70, 87]. The field enhancement due to LSPR can lead to an enhancement in the absorption and emission cross-section from the nearby

SQD[22, 40, 43, 88]. It is also possible that electron-hole recombination can occur in an excited SQD, non-radiatively through excitation of plasmon in the MNP. Such relaxation will cause an reduction in PL emission[20, 75, 89]. On the other hand, a plasmon excited in the MNP can decay by exciting a electron-hole pair in SQD and thereby contribute to an increase in PL[19]. Such energy exchange between MNP and SQD strongly depends on several factors like shape, size, properties of the individual elements and its distribution[90–94]. Most of these studies in HNSs have been focused on exploring distance or size-dependent plasmon-exciton coupling between MNP and SQD[17, 70, 87]. However impact of excitation energy on the relaxation process in SQD in the presence of MNP still remains unclear.

Finally, the rest of the thesis is structured in the following way: In chapter 2, we discuss about the different techniques used to characterize the individual components and HNS under study. In chapter 3, we demonstrate a method to prepare a single type of HNS by measuring only its optical response. The required theory is also presented in this chapter. The method developed in chapter 3 is used to synthesize HNS where a SQD is placed between two Ag nanospheres. The static and ultrafast properties of this Ag\Cdte/Ag HNS is discussed in chapter 4. In chapter 5, we present the static and ultrafast optical response of HNS in which each MNP of spherical shape is completely surrounded by SQDs and discuss about the origin of the observed properties. In chapter 6, we discuss about the static and ultrafast optical response of HNS formed by each MNP nanoplate covered by SQD. In this chapter, we use this HNS to develop a formalism to quantify the charge transport between the two constituents of the HNS at ultrafast time scales. Lastly, chapter 7 gives the conclusion of the thesis.

Chapter 2

Experiment Details and Methodology

Due to recent growth in nanotechnology, nanoparticle of a single material could be sythesized with good control over shape and size. There are two kinds of approach in growing nanoparticles, the top-down approach and the bottom-up approach. In top-down approach, the nanoparticles are formed by slicing or fragmenting bulk material down to nanoscale size by using technique like lithography, milling, machining, etc. On the other hand, in bottom-up approach, nanoparticles are build up from bottom, atom by atom, molecule by molecule and cluster by cluster by self-organization using wet-chemical method, vapour phase deposition, sol-gel, etc. Both of these approaches have their own set of advantages and disadvantages. Top down approach is good for producing relatively larger structures with long range order and for making macroscopic connections. However, these methods are often destructive which causes significant crystallographic damage resulting in pronounced surface and structural imperfections. Bottom-up approach, on the other hand, is best suited for preparing nanoparticles in few nanometer scale dimensions with good control over their size & distribution with less defect. Thus, with the umpteen advantages, the bottom-up approach is widely chosen for the production of nanoparticles. Figure 2.1 shows the schematic of these two synthesis methods for nanoparticle preparation.

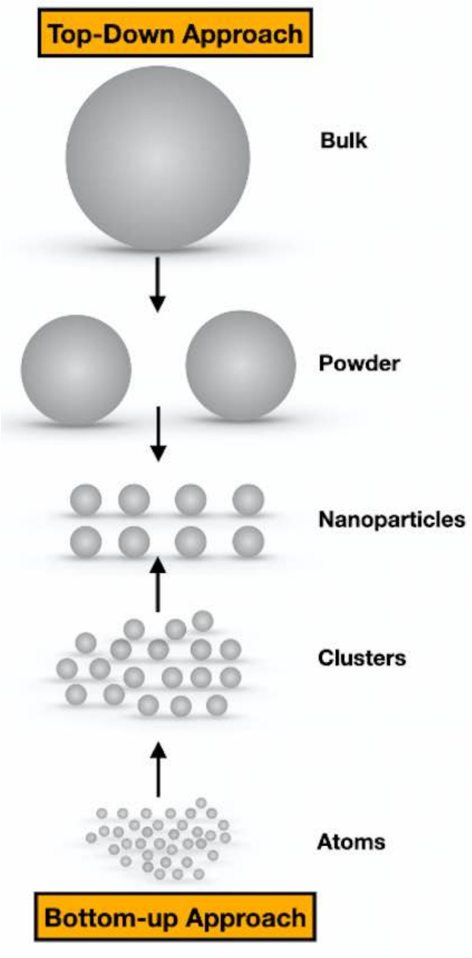

FIGURE 2.1: Schematic representation of the top-down and bottom-up methods of nanoparticle synthesis.

Once the nanoparticles are synthesized, they need to be characterized to understand their true structure, and optical properties. For example, microscopic technique like atomic force microscope (AFM) and transmission electron microscope (TEM) can be used to explore the structural properties of the particles. These techniques are also useful for determining morphology, particle average size distribution and it's shape. Spectroscopic techniques like ultraviolet-visible (UV-Vis) and PL are employed for confirming the concentration of particles and their electronic transitions, studying emission and absorption properties and monitoring time-dependent luminescence. Similarly, ultrafast pump-probe measurements is used for monitoring the time-dependent carrier dynamics that occurs in ultrafast time scales (femtoseconds) and is analysed using two-temperature model (TTM) and band filling effect. Each of these techniques has its own advantages and disadvantages, therefore combination of different techniques are used for obtaining complementary results.

Many times, it is essential to understand the modification in the static optical response of the particles with respect to its bulk. In case of spherical particles, Mie theory could be used to calculate the expected optical response of nanoparticles[95]. On the other hand, general theory similar to Mie theory does not exist for optical response of particles of arbitrary shape and even aggregates of spheres. Hence, one has to rely on numerical techniques like DDSCAT or T-matrix. Using the results obtained by these numerical simulations, it is possible to calculate the expected optical response of a nanoparticle. This theory can also be used for estimating the size of the particles. By comparing the C_{ext} estimated by the calculation with that of the experimentally measured, it is also possible to estimate the number density of particles in the sample.

2.1 Sample Preparations

In this thesis, silver (Ag) and cadmium telluride (CdTe) are used as model MNP and SQD, respectively. The idea is to fix the material and study the changes in the static and ultrafast optical response with respect to the structure of hybrid. Ag NP are the most commonly used, highly commercial nanoparticles. This is due to their unique properties like high chemical stability, size and shape tunable LSPR in visible regime, and are also very cost effective. On the other hand, CdTe QDs are being reconsidered extensively in the field of laser, LED and biomedical applications due to their size tunable optical properties and narrow emission width in the visible regime and also have higher photostability.

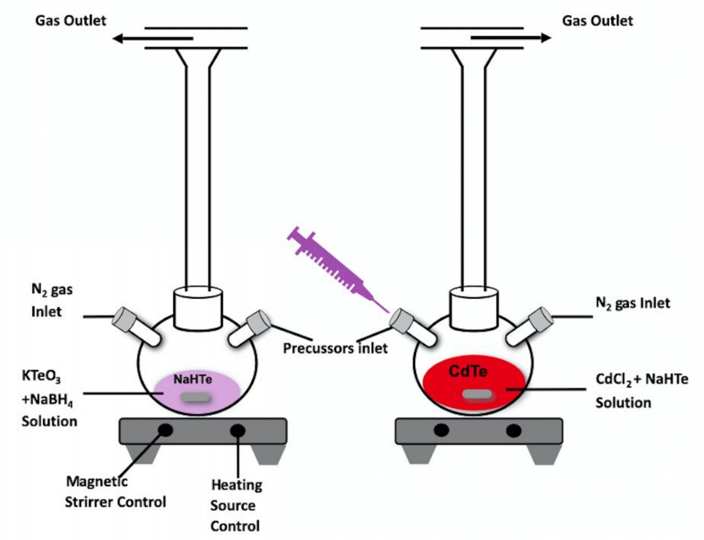

FIGURE 2.2: Schematic of CdTe QD growth setup.

FIGURE 2.3: Photographs of PL emission from CdTe QDs of different sizes when excited by 400 nm.

2.1.1 Preparation of CdTe quantum dots

The two pot synthesis method was adopted for the preparation of CdTe QDs. Figure 2.2 shows the schematic illustration of CdTe QD growth setup . This process required cadmium chloride ($CdCl_2$) and potassium tellurate ($KTeO_3$) as precursors.

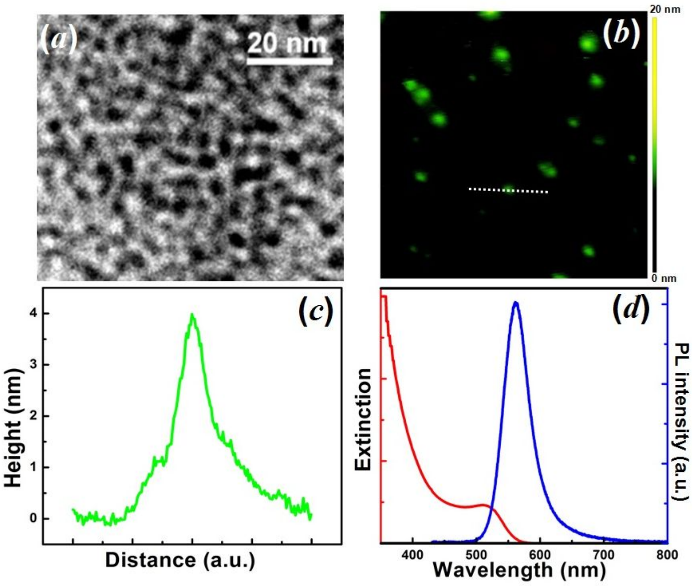

FIGURE 2.4: (*a*) TEM images and (*b*) the pseudo color images of AFM height profiles of CdTe QDs. The height profile along the straight lines marked in the AFM images is shown in (*c*) which is obtained from the AFM images for the CdTe QDs. (*d*) The extinction and PL emission of CdTe QD of size $\sim$ 4 nm in water.

2.3 mM of $CdCl_2$ was dissolved in 100 ml of ultrapure water with resistivity 18 M Ω followed by 0.8 ml of thiolglycolic acid (TGA). The solution was kept under Nitrogen atmosphere and was constantly stirred by magnetic stirrer. The pH value of the solution was adjusted to be in the range 10.5-11 using 1 M sodium hydroxide (NaOH) solution. The Cd source was then transferred to a three-necked flask. Alongside, 1 mM of $KTeO_3$ was dissolved in water in another three-necked flask. $KTeO_3$ source solution was reduced by ice cold sodium borohydride ($NaBH_4$) solution and then heated at 80^o C under constant stirring. The $KTeO_3$ then reduces to NaHTe which was indicated by the pink colour of the solution. This solution was then quickly transferred to Cd solution. The mixture was then heated at 90^oC for hours to form CdTe QD of desired size. Figure 2.3 shows photograph of PL from CdTe QD of different sizes in water when excited by 400 nm laser. Figure 2.4(*a*), and (*b*) shows the typical TEM and AFM image of CdTe QD, respectively. The average size estimated from these images is $\sim$ 4 nm. A typical extinction and PL spectrum of as prepared CdTe QDs colloid is shown in Fig.2.4(*d*).

2.1.2 Preparation of Ag nanospheres

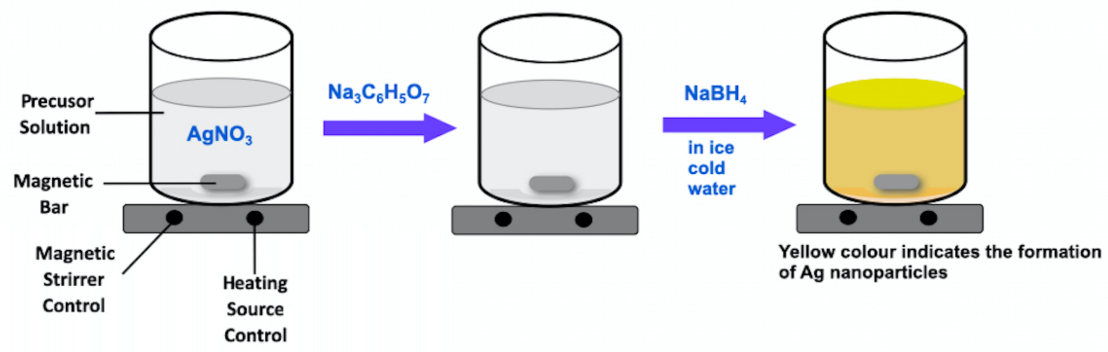

FIGURE 2.5: Schematic of Ag NP growth process.

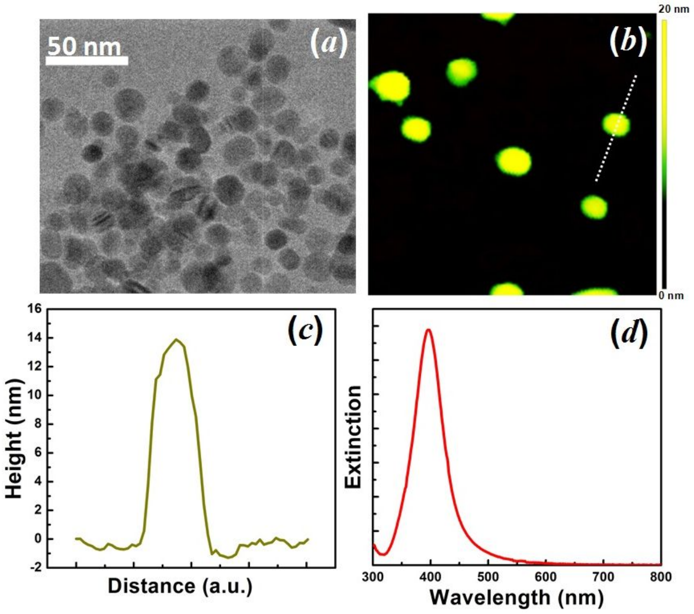

FIGURE 2.6: (*a*) TEM images and (*b*) the pseudo color images of AFM height profiles for Ag nanoshperes. The height profile along the straight lines marked in the AFM images is shown in (*c*) which is obtained from the AFM images for the Ag nanoshperes. (*d*) The typical extinction of small Ag nanoshperes of size ∼ 15 nm in water.

Colloidal solution of Ag nanospheres in water was prepared chemically by a method similar to that reported by Jin et.al[96]. Figure 2.5 shows the schematic illustration of Ag nanosphere growth process. In this process, 5 mM $AgNO_3$ was dissolved in 100 ml of ultrapure water. 30 mM trisodium citrate was then added into the solution. After 45 mins, 1 ml of $NaBH_4$ in ice cold solution was added to the mixture. The solution turned yellow, indicating the formation of Ag nanospheres. Over next 10 mins, few more drops of $NaBH_4$ solution were added for the complete reduction of the $AgNO_3$. The solution was stirred by magnetic stirrer at room temperature during the entire preparation procedure. Figure 2.6(*a*), and (*b*) shows the typical TEM and AFM image of Ag nanospheres, respectively, of size nearly 15 nm. The extinction spectrum of the same Ag nanospheres colloid is shown in Fig.2.6(*d*).

2.1.3 Preparation of Ag nanoplates

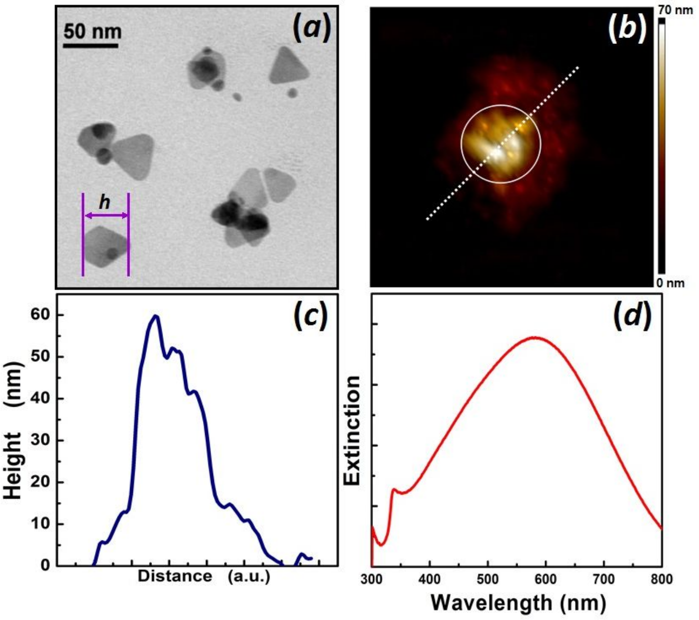

FIGURE 2.7: (*a*) TEM images and (*b*)The pseudo color images of AFM height profiles for Ag nanoplates. The height profile along the straight lines marked in the AFM images is shown in (*c*) which is obtained from the AFM images for the Ag nanoplates (encirlced). (*d*)The typical extinction spectrum of Ag nanoplates in water.

Colloidal solution of silver nanoplates in water was prepared chemically by a method similar to that reported by Metraux[97]. In this method, 1 mM of silver salt ($AgNO_3$) was dissolved in 100 ml of ultra pure water. To this, 1.2 M solution

FIGURE 2.8: Photograph of Ag NP colloid (left: yellow color - nanospheres, Right:blue color- nanoplatelets).

of tri-sodium citrate and 10 mM of Polyvinylpyrrolidone (PVP, MW 40000) in water were added and stirred vigoursly at room temperature. A measured amount of hydrogen peroxide (H_2O_2, 30 wt % 1.2 ml) was added to it. After some time, 8 mM solution of $NaBH_4$ was added to the above solution which reduces the silver salt. The solution shows a series of color changes as soon as the reducing salt is added to it. The solution was stirred by magnetic stirrer during the entire preparation procedure at room temperature. The solution turned blue which indicates the formation of Ag nanoplates. Figure 2.7(*a*), and (*b*) shows the typical TEM and AFM image of Ag nanoplates, respectively. It shows particles of an average diameter and thickness of 34 nm and 5.2 nm, respectively. The typical extinction spectrum of this Ag nanoplates in water is shown in Fig.2.7(*d*). Figure 2.8 shows photograph of nanospheres (yellow coloir) and nanoplates (blue color) dispersed in water.

2.1.4 Preparation of Hybrid Nanostructures

The HNS in colloidal solution were prepared by mixing individually prepared colloidal solution of Ag NP capped with trisodium citrate and CdTe QD capped with TGA. During synthesis, citrate ions attach loosely to the Ag cluster which provides the particle surfaces with a negative net charge. This is one of the common way to

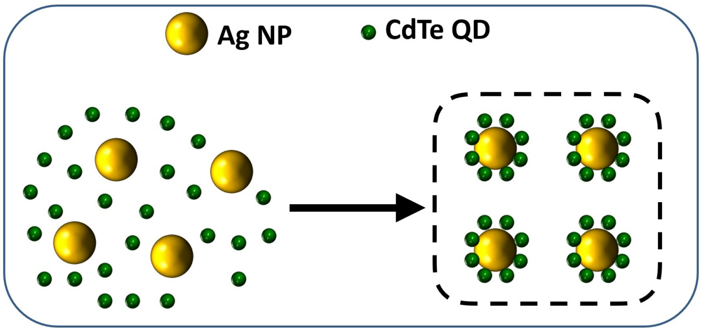

FIGURE 2.9: Schematic representation of the self-organization process in hybrid sample.

stabilizes the particles solution against vanderWaals attraction. Similarly, the TGA also provides negative net charge to CdTe QD core, providing the stabilization of the CdTe QD colloid. This type of stabilizing the particles, using electrostatic repulsion, is called electrostatic stabilization. In the mixed solution of Ag NP and CdTe QD colloids, both the Ag and CdTe particles are negatively charged. When TGA capped CdTe QDs are brought near to Ag NP, TGA replaces citrate in Ag NP via ligand exchange because citrate layer in Ag NP is loosely bound and Ag core has better affinity towards TGA than citrate. Thus HNS of CdTe QD and Ag NP is formed in the aqueous solution. Such process of forming HNS are called self-organization. Figure 2.9 shows the schematic of self-organization process that forms hybrid particles. We prepared the hybrid sample by mixing the SQD colloid with MNP colloid in a ratio γ, where γ is defined as the ratio between the volume of the MNP colloid (V_P) to that of the SQD colloid (V_D). Figure 2.10(a) shows the typical AFM image of HNS. AFM scans of HNS shows a broader wing (Fig.2.10(b)) corresponding to the CdTe QDs surrounding the Ag NPs. Figure 2.10(c), shows the extinction spectrum of HNS colloid in comparison to non-interacting mixture of Ag NP colloid and CdTe QD colloid. The non-interacting mixture of CdTe QD and Ag NP does not match with the hybrid which implies that there is some kind of synergistic interaction between CdTe QD and Ag NP. Figure 2.10(d) shows the PL emission spectrum from HNS which is quenched when compared to PL emission spectrum from CdTe QD.

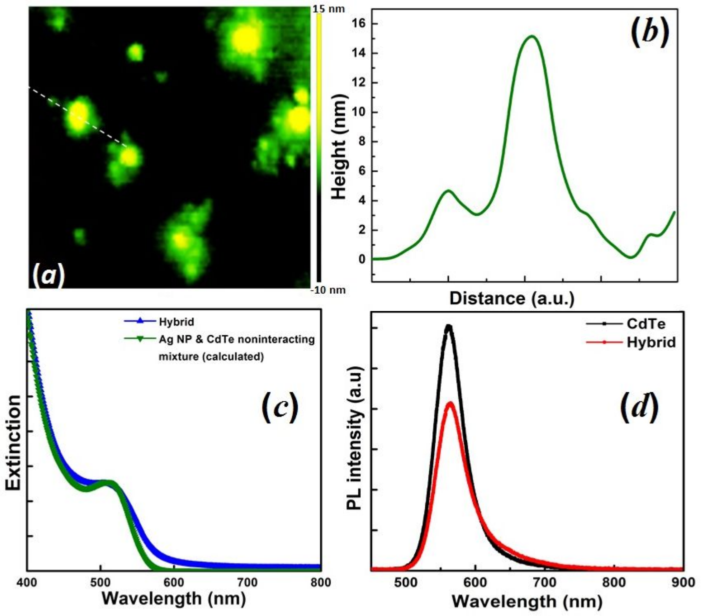

FIGURE 2.10: (*a*) The pseudo color images of AFM height profiles for HNS. The height profile along the straight lines marked in the AFM images is shown in (*b*) which is obtained from the AFM images for the HNS. (*c*) The extinction of HNS colloid in comparison with non-interacting mixture. (*d*) The PL emission from HNS in comparison with CdTe QDs in colloidal form.

2.2 Structural Characterization of Nanoparticles and Hybrid

For structural characterization, a few drops of individual colloid and hybrid colloid were dried on mica substrates and used for AFM and TEM studies[98]. The AFM is a type of scanning probe microscope based on non-optical surface investigation. It uses a physical probe (a nanoscale tip) attached to a cantilever to measure the surface morphology. When it comes in contact with surface, the cantilever bends and the bending is detected by laser diode and photodetector. The bending of cantilever gives the information of the tip-sample interaction force. There are two common ways of AFM imaging that are widely used; contact mode and tapping mode. In contact mode, the tip and sample touches each other constantly throughout the scanning. In tapping mode, the contact between tip and sample are limited by moving the tip up and down. In this thesis, the AFM measurement were done in a tapping mode because both constituent particles and HNS particles are loosely held to mica substrate and can get easily damaged during topography imaging.

In TEM microscopy technique, a beam of electrons is transmitted through sample. As the beam is transmitted, these electrons interact with sample and forms an image. In this thesis work, the presence of the capping agents (polymers) in MNP (nanospheres and nanoplates), CdTe QDs and HNS samples makes the process of capturing TEM images very difficult. Removal of these polymers by centrifuging would destroy the HNS present in the colloidal solution. Further, we find that during TEM studies, the measurement had to be performed at very low irradiation, and the images had to be accrued quickly to reduce the damage. Even then sometimes during the measurement, it was found that the particle disappear during image accusation.

2.3 UV-Vis Spectroscopy

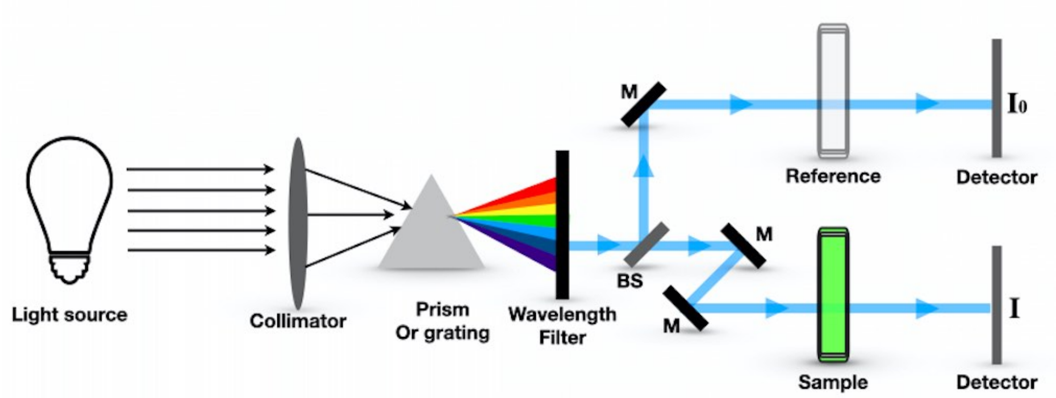

FIGURE 2.11: Schematic diagram of the UV-Vis spectroscope.

UV-Vis spectroscopy is an absorption/reflection based technique that involves measuring intensity of absorption or reflection at different wavelengths[99]. In this thesis work, absorption spectra was measured with a double beam UV-Vis Spectrometer, the schematic of which is shown in Fig.2.11. The basic parts of spectrometer consists of a light source in the wavelength range of 200-1200 nm, a sample holder, a grating and a detector. In this technique, a single wavelength from source is isolated using monochromator. This beam is split into two beams, one that passes through the samples and another passes through the reference. The colloidal samples are poured in cuvette, typically 1 mm thickness, and placed in sample holder. A reference sample, usually water, of same thickness is chosen as reference. The ratio between the two intensities passing through reference (I_0) and samples (I) are related to absorbance(A) as $A = log_{10}(I/I_0)$ and gives the final spectrum. Further, the absorbance (A) can be used to extract the quantitive information about the concentration of absorbing particles in the solution using the Beer-Lambert law, $A = \epsilon c b$, where, ϵ is the molar extinction coefficient ($M^{-1}mm^{-1}$), c is the concentration of absorbing particles (M) and b is the path length of sample cuvette (mm). The peak in the absorption spectrum can also be used to identify the properties of the absorbing particles in the sample. In particular, Ag NP shows a distinct LSPR absorption peak due to collective oscillation of free electrons as shown in Fig.2.6(d) and CdTe QD is determined by characteristic absorption peak arising due to electron transition to exciton energy level, shown in Fig.2.4(d).

2.4 Photoluminescence Spectroscopy

Measurement of the time and spectral dependence of the magnitude of PL from the SQD or MNP-SQD hybrid can provide many information about the dynamic processes happening in these materials[99]. In a simplistic picture, at time $t = 0$ i.e. when the excitation is off, the rate at which the excited QDs/nanostructures decay to the ground state is given by the rate equation,

$$\frac{dN(t)}{dt} = -kN(t). \tag{2.1}$$

This rate equation is solved to describe the decrease in the population of the excited state at all time after $t = 0$ and is given by,

$$N(t) = N(0)e^{-kt}, \tag{2.2}$$

where $N(0)$ is the initial population in the excited state (at t = 0), τ is the lifetime of the excited state, defined as the time for the population to decay by $1/e$ times that of the initial population and k is the relaxation rate which is the sum of rates of all the possible deexcitation path,

$$k = k_f + k_{nr}. \tag{2.3}$$

Here, k_f is the rate of radiative decay and k_{nr} is the sum of rate of non-radiative decays. Therefore,

$$\tau = \frac{1}{k_r + k_{nr}}. \tag{2.4}$$

The PL lifetime, τ, thus depends also on the non-radiative decay mechanisms. One of the important parameter in PL measurement is the fluorescence quantum yield (ϕ). The ϕ is defined in terms of rate constant as,

$$\phi = \frac{k_r}{k_r + k_{nr}}. \tag{2.5}$$

It can be seen that as the non-radiative path for the deexcitation process increases, the quantum yield decreases and hence the PL lifetime decreases. In general, the growth and decay of the PL depends on several energy states and excitation mechanism. Therefore, the transient PL will have complicated rise and decay which can also be non-exponential.

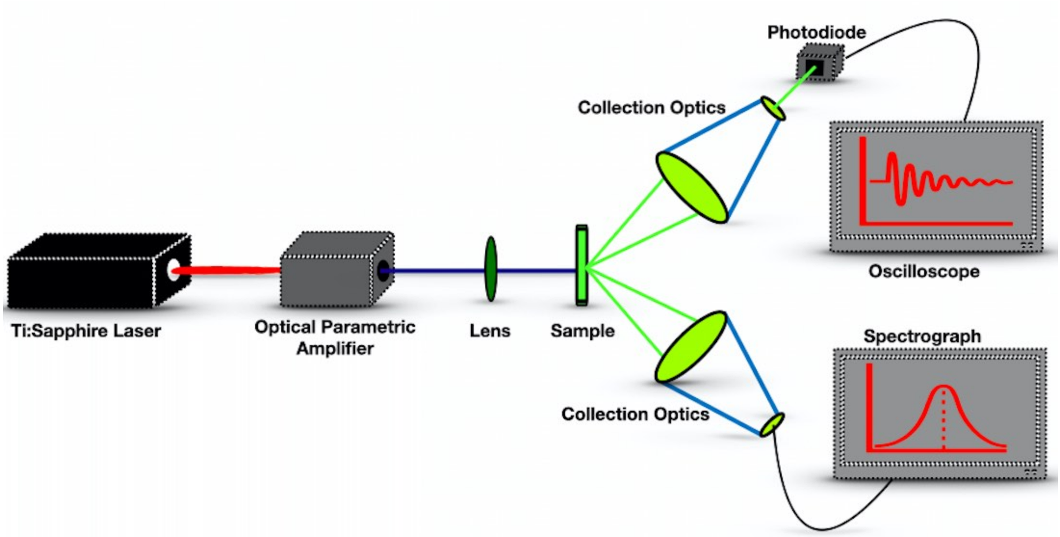

FIGURE 2.12: Schematic representation of the setup used for the steady-state and time-resolved photoluminescence measurements from the samples.

In this thesis, the steady-state PL and time-resolved PL measurements were carried out by exciting the samples using the output of an optical parametric amplifier (OPA) (schematic shown in Fig.2.12). The OPA was pumped by a 1 kHz Ti:Sapphire amplifier system with a pulse duration of 35 fs at 800 nm wavelength. The OPA output with a pulse width of nearly 80 fs were tuned to different wavelength for the selective excitation of the samples. The PL emitted by the sample was then collected using combination of lens and detected by a spectrograph for spectrum measurement and a fast photodetector-oscilloscope system for dynamics measurement. The photodetector-oscilloscope system consists of photodetector with a rise time of 300 ps and the oscilloscope with a bandwidth of 1 GHz and a sampling rate of 20 GS/s. The decay time estimated for the later part of the instrument response function (IRF) is 350 ps. The entire measurement was carried out at room temperature.

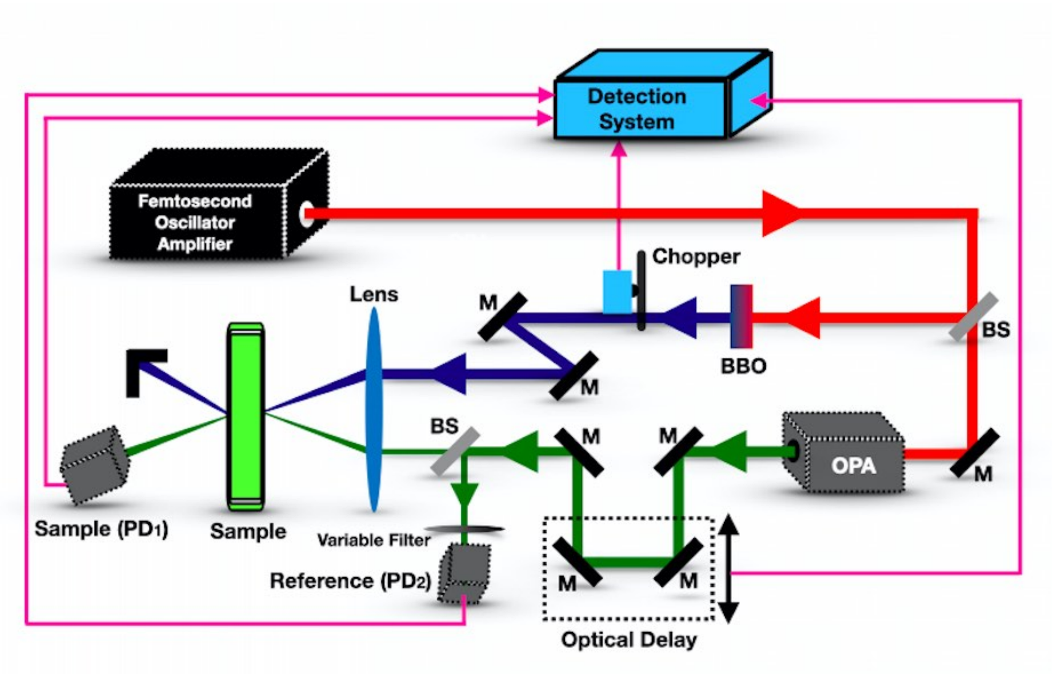

FIGURE 2.13: Schematic representation of the pump-probe setup used for the measurement of transient transmission from the samples. M, BS and PD represents mirror, beam splitter and photodetector, respectively

2.5 Ultrafast Spectroscopy

Ultrafast spectroscopy involves studying temporal changes in the optical properties of a sample that occurs in materials induced by short optical pulse[100]. In this technique, materials are excited by intense ultrashort laser pulse (pump pulse) which excites the samples to its excited state. This changes the optical constant(dielectric constant) of the sample. Simultaneously, another ultrashort laser pulse with very low intensity is made to fall on the material with variable time delay with respect to the first exciting pulse. The lifetime of the excited state is short lived, therefore the optical constant eventually returns back to their initial value same as before excitation by pump pulse. The low intensity laser pulse probes the changes occurred by pump beam. The final result is basically the change in the transmitted probe pulse energy with respect to delay between pump and probe. In a mathematical picture, the transmitted probe intensity depends on the delay, τ, and is given by,

$$I_T = I_I e^{-(\alpha_0 L + \Delta\alpha_0(\tau))L)}, \tag{2.6}$$

for $\Delta\alpha_0 L << 1$,

$$I_T \approx I_I e^{-\alpha_0 L}(1 + \Delta\alpha_0(\tau)L), \tag{2.7}$$

$$I_T(\tau) \approx I_T(\tau < 0)(1 + \Delta\alpha_0(\tau)L), \tag{2.8}$$

where, I_T and I_I are the transmitted and incident probe intensity, respectively and L is the sample cuvette length. Now, the relative change in transmitted intensity with respect to τ also known as transient transmission, is given by,

$$\frac{\Delta T(\tau)}{T_0} = \frac{I_T(\tau) - I_T(\tau < 0)}{I_T(\tau < 0)} \tag{2.9}$$

$$\Rightarrow \frac{\Delta T(\tau)}{T_0} \approx -\Delta\alpha_0(\tau)L \tag{2.10}$$

Thus, using Eq.2.10 and measuring the change in probe intensity with time delay between pump and probe, the dynamics of the system can be calculated.

In this thesis, to study the ultrafast transient properties of the samples, transient transmission measurements were carried out in two-color pump probe geometry using a 1 kHz Ti-sapphire laser of pulse duration 35 fs operated at 800 nm wavelength (schematic shown in Fig.2.13)[101]. In this setup, the output of the femtosecond oscillator-amplifier system was split into two beams using a beam splitter. One of these beams was converted to 400 nm using second harmonic generation in Beta-barium Borate (BBO) crystal which was then used as the pump beam. The other beam from the beam splitter was fed to an OPA. The output of the OPA, centred at different wavelength, was used as the probe beam. The intensity of the laser beam at the sample position was varied using neutral density filter. The signal was detected using the combination of boxcar and lock-in amplifier. We also carried out similar measurement using high repetition rate laser (80 MHz). The entire measurement was carried out at room temperature.

2.6 Optical Response Calculation

To understand the modification in the optical response of HNS with respect to their constituent MNP and SQD, we use numerical technique, T-matrix and DDSCAT. These techniques predicts the optical response of HNS governed by electromagnetic interaction. For such calculation, dielectric constant ϵ of Ag NP and CdTe QD are required as an input. For Ag NP sizes used in this thesis, bulk ϵ is sufficient. Therefore we use the bulk ϵ of Ag NP as reported by Johnson and Christy[39]. However, for CdTe QD, due to the quantum confinement, the ϵ gets modified and hence needed to be estimated from the experiment.

2.6.1 Dielectric constant of CdTe QD

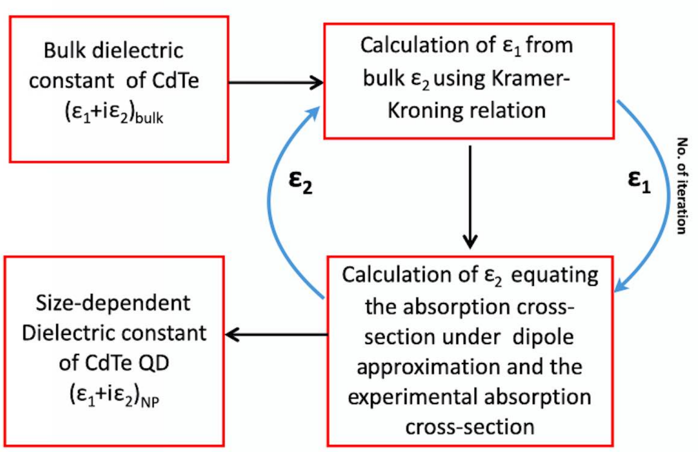

FIGURE 2.14: Schematic representation of the iterative method to calculate the size dependent dielectric constant of CdTe QD.

We have used the technique reported by Marcelo Alves-Santos et.al for obtaining ϵ(E) from the optical absorption spectrum[102]. It uses trial and error procedure in which absorption spectrum is calculated using initial value of ϵ from the bulk CdTe and then iteratively improving it until the theoretical absorption spectrum matches with the experimental spectrum within a specified accuracy. The obtained ϵ is then converted into refractive index for T-matrix calculation. Figure 2.14 shows the schematic representation of this method to calculate the size dependent ϵ of CdTe QD.

2.6.2 T-matrix Calculation

T-matrix is a numerical method to calculate the scattering and absorption of electromagnetic field by any arbitrary shaped particle formed by any collection of spherical particles. In T-matrix calculation, the incident and scattered electric fields are expanded in series of vector wave function. These incident and scattered fields are related by transition matrix or in short, T-matrix. The T-matrix elements are then obtained by solving Maxwell's equations using boundary condition. Initially, the T-matrix was introduced by P.C. Waterman in 1965 and later developed by various group[103, 104]. Numerical codes for the evaluation of the T-matrix are available online in public-domain package of FORTRAN computer programs `https://www.giss.nasa.gov/staff/mmishchenko/t_matrix_database.html`.

2.6.3 Discrete Dipole Approximation

Discrete Dipole Approximation (DDA) is a numerical method to calculate the scattering and absorption of electromagnetic field by an arbitrary shaped particle with arbitrary composition. As the name suggest, the DDA replaces the smooth dielectric particle by discrete array of dipoles that interact with the incident field. These dipoles acquire dipole moments in response to the local electric field. Initially the

DDA was proposed by Purcell and Pennypacker[105]. Using Clausius-Mossotti relation, the dielectric constant of a substance can directly be related to polarizability of individual elements which it is composed of. All the measured scattering quantities can be obtained from these polarization. As the number of array increases, the accuracy of the approximation increases but becomes computationally challenging. Numerical codes for the evaluation of the DDSCAT are available online in public-domain package of FORTRAN computer programs `http://ddscat.wikidot.com/`.

2.7 Summary

In this thesis, Ag NP and CdTe QD are prepared in water by bottom-up approach using wet chemical method. For the structural characterization, AFM and TEM have been used to determine the size and shape of the particles. UV-Vis spectroscopy and photoluminescence spectroscopy have been employed to understand the optical properties of the hybrid samples as well as individual component . On the other hand, the electron dynamics in the samples are obtained using ultrafast pump-probe spectroscopy. All the studies are carried out at room temperature. In theoretical methodology, T-matrix and DDSCAT have been employed to predict the electromagnetic interaction between the particles. Such predictions will give the information about the various interactions taking place between MNP and SQD. In this thesis, the comparative studies between the experimental observations and the model will be carried out.

Chapter 3

Theory of optical response of Mixed Samples

The optical response of metal-semiconductor hybrid can exhibit unique properties, that depends on the numerous parameters like size, shape, and the properties of linking molecule[66, 69–71]. It is possible to prepare HNS with different properties in a controlled manner by self-organization of individually prepared MNP and SQD colloid. Several groups have prepared different HNS by changing the mixing ratio to control the synergistic interaction between MNP and SQD and observed a gradual change in the optical response for each mixing ratio[20, 71, 75]. They have attributed it to a change in the interaction between the MNP and SQD, implying that at different mixing ratios, different HNS may be formed. It is not clear whether this mixing can be controlled to get a single type of hybrid rather than a distribution of various structures. Also, after mixing, the mixed colloid may contain the hybrids formed as well as unattached MNPs and SQDs. In such a case, a methodology is required to unambiguously determine the optical response of the hybrid from measurements done on the mixed sample. In this chapter[**] , using experimental results and an empirical model, we show that if the mixing of the MNP and SQD is carried out by gradually increasing the mixing ratio and measuring their optical response,

---

[**] This work is published by the author of this thesis and reproduced from "The optical response of self-organized Ag-CdTe metal-semiconductor hybrid nanostructures: Change in interaction vs number density variation", **Sabina Gurung**, Asha Singh, Rama Chari, J Jayabalan, Journal of Applied Physics, **2018**, 124(20), 204305, with the permission of AIP Publishing.

it is possible to get a mixture of one type of HNS. We demonstrate a method to determine the true optical response of HNS from measurements on mixed colloids.

3.1 Optical Response and Structural Characterization of Mixed Sample

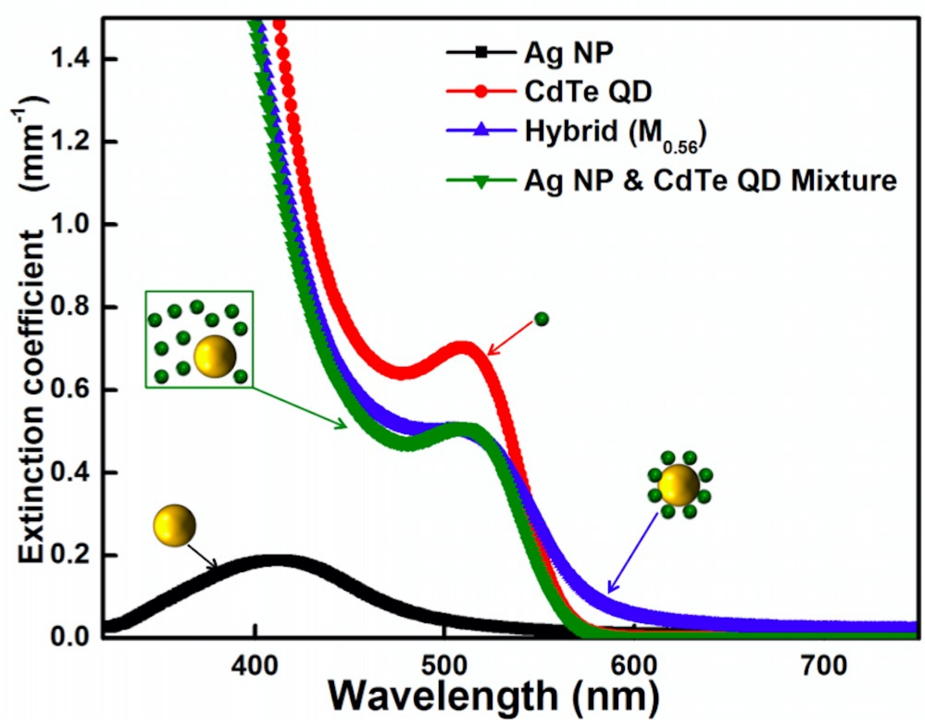

FIGURE 3.1: Experimental extinction spectra of pure Ag nanosphere colloid, pure CdTe QDs colloid and a Ag-CdTe hybrid ($M_{0.56}$). An estimated extinction spectrum of non-interacting mixture of Ag NP colloid and CdTe QD colloid of the same ratio of that of $M_{0.56}$ is also shown.

Figure 3.1 shows the extinction spectra of the as prepared Ag NP colloid, CdTe QD colloid and the spectrum of a mixed sample $M_{0.56}$ (the subscript indicates the γ value as defined above.). The extinction spectrum of the Ag NP colloid shows a single LSPR peak at 412 nm which are typical for small Ag NPs in water [20, 106]. The optical absorption spectrum of the as prepared colloidal CdTe QD sample shows that the onset of absorption occurs at ∼570 nm corresponding to an energy of ∼

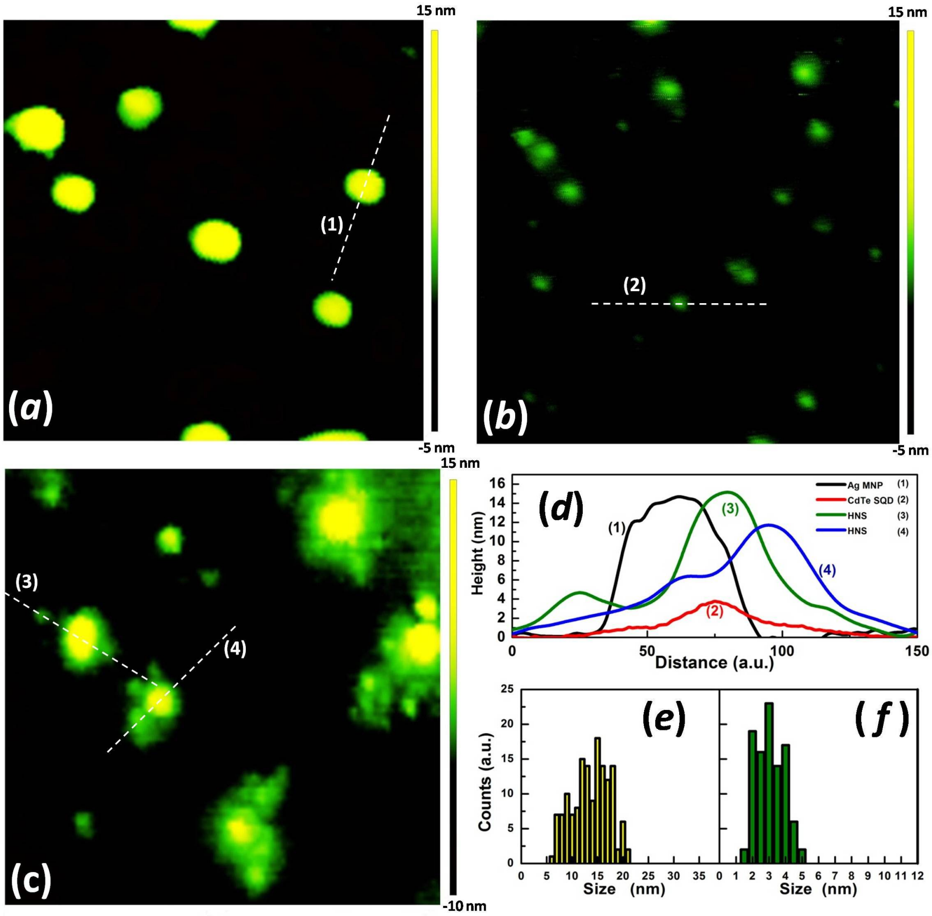

FIGURE 3.2: The pseudo color images of AFM height profiles for (*a*) Ag NPs, (*b*) CdTe QDs and (*c*) Ag-CdTe HNS. The height profile along the straight lines marked in the AFM images are shown in (*d*). (*e*) and (*f*) are the histogram of height (diameter of the particle) obtained from the AFM images for the Ag NPs and CdTe QDs respectively.

2.17 eV. This onset is much blue shifted when compared to bulk CdTe (∼1.5 eV) indicating the quantum confinement effect. The spectrum also shows a clear excitonic peak at ∼ 511 nm, which is due to the 1s(e)-1s(h) transition. The average size of the QDs in the colloid estimated from this excitonic peak is 2.6 nm [107]. The extinction spectrum of the hybrid sample, $M_{0.56}$, is expectedly quite different from either of the two colloids. If the MNPs and SQDs were not interacting in the colloid, then the transmission spectrum of the mixed sample would have been a product of the measured individual transmissions scaled to the respective mixing volumes. Figure 3.1 also shows this calculated absorption spectrum and it does not match with the measured one indicating that there is an interaction between Ag NPs and CdTe

QDs in the mixed colloidal solution. We propose that the Ag NPs and CdTe QDs form hybrid nanoparticles. Earlier, different groups have studied various properties of such Ag-CdTe hybrid samples prepared in different mixing ratios and had shown that interaction does happen in nanometer length scales[11, 20, 75]. This was further confirmed by characterizing the samples using an atomic force microscope (AFM) (Fig. 3.2). AFM has been reported to be a more suitable method of imaging the hybrids of particles linked by polymers[108, 109]. For comparison, we have also performed AFM measurements on the individual colloids. A few drops of each solution were dried on mica substrates and used for the AFM studies. The AFM images of the pure SQDs and MNPs samples show isolated particles. In the colloidal form, the Ag NPs and CdTe QDs are stabilized by citrate and TGA capping, respectively. Hence, after drying it is expected that these particles will have the coating of the capping agents. In case of CdTe QDs such coating can lead to an increase in size in the range of 0.4 nm to 0.8 nm if measured by AFM[69].

The average diameter estimated for Ag NPs coated with citrate and CdTe QDs coated with TGA from the AFM profile height are 13.7 and 3.1 nm, respectively. The difference of 0.5 nm between the AFM estimate for the size of coated CdTe QDs with that estimated from Peng's formula is within that expected for TGA coating[69]. For the mixed sample, the image shows large particles surrounded by smaller particles and the size corresponds to that expected if each Ag NP was surrounded by the smaller CdTe QDs. In the present hybrid sample, the Ag NPs and CdTe QDs could be identified by AFM due to their difference in size range [see Figs.3.2(*c*) and (*d*)]. Further, AFM scans of pure Ag NP show a sharp edge while the Ag NPs in the hybrid sample show a broader wing (see also the height profile plots of Fig.3.2). We attribute the wing to the CdTe QDs surrounding the Ag NPs. It is to be noted that the AFM image of the hybrid structures can only be indicative of what is present in a colloidal solution as the process of drying out can distort the true morphology

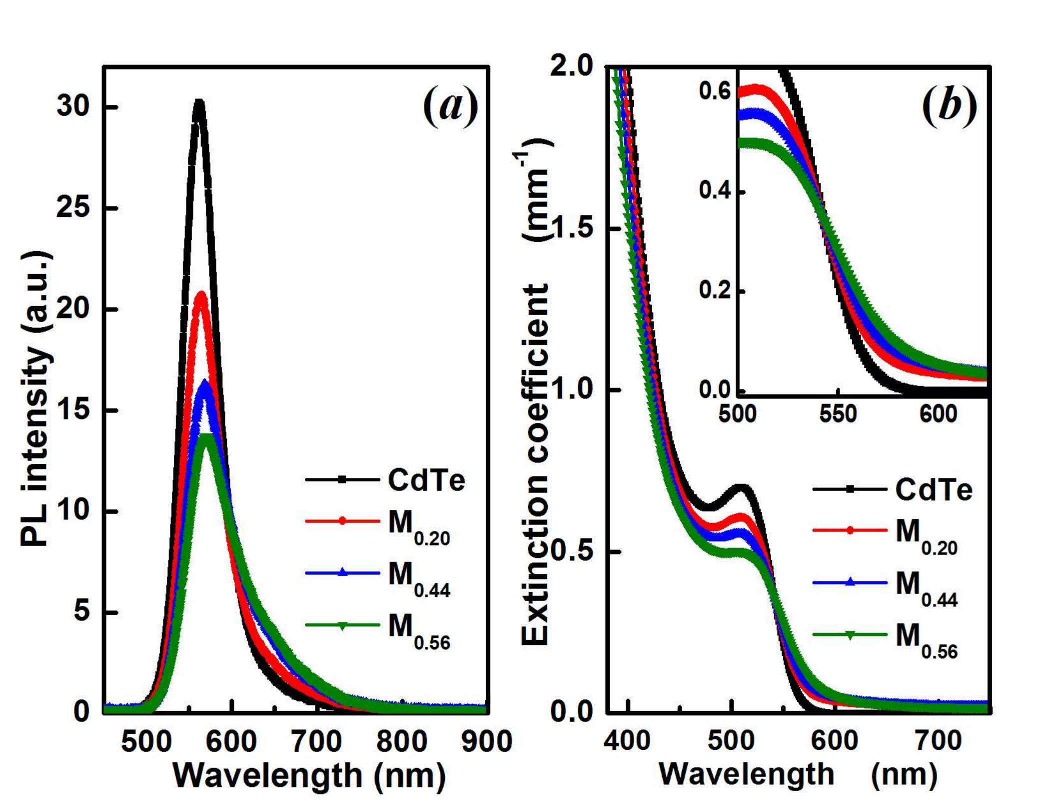

FIGURE 3.3: Optical response measured for the mixed hybrid samples of different mixing ratios along with that of pure CdTe colloid: (*a*) PL spectra and (*b*) extinction spectra. Inset shows the expanded view of the extinction spectra near the band edge.Excitation wavelength is 405 nm

Figure 3.3(*a*) shows the measured PL spectra of pure CdTe QD colloid and several mixed colloids prepared with different mixing ratios. The PL spectrum of the pure CdTe QD sample shows a peak at wavelength $\sim$ 560 nm and has a full width at half maximum (FWHM) of $\sim$ 38 nm. As the Ag NP colloid is gradually added, the PL spectrum of the mixed sample also shows gradual changes. With increasing fraction of MNPs in the mixture, the PL starts reducing. For example the PL emission strength of the sample $M_{0.56}$ is reduced by 54% of the pure CdTe QD colloid. Part of the reduction in intensity could be due to the addition of a solvent (water in the present case) that gets added along with MNPs. However this dilution accounts for only about 36% reduction in PL. With increase in Ag NP colloid fraction there is also a red-shift in PL peak. The PL peak wavelength of the sample $M_{0.56}$ is red-shifted by about 10 nm to 570 nm when compared to that of pure CdTe QD colloid. As the fraction of Ag NP colloid increases the PL spectra of the mixed sample becomes increasingly asymmetric with an increase in emission on the red-side of the spectra [Fig.3.3(a)]. The increase in red-side of the spectra can also be observed in the extinction spectra of the mixed colloid (Fig.3.3(b)). The nearly sharp feature of exciton peak washes out with increase in the amount of Ag NP colloid. We also find that if the fraction of Ag NP colloid is increased beyond 0.56, there is a sudden quenching of PL and large aggregated particles are observed in the sample.

In case of self-organized growth of HNS where MNPs and SQDs are prepared separately and mixed, the capping agents used in both of these particles play a crucial role in deciding the interaction between them. In the present case, the capping agent used for stabilizing the CdTe QDs, TGA, has a strong affinity to get attached to metal surface. It forms complexes with metal ions[69, 71]. When Ag NPs are mixed with the much smaller CdTe QDs, due to the chemical interaction between TGA and Ag NPs, it is expected that several of CdTe QDs will get attached to the silver surface [70, 75]. For the case when the number of Ag NPs are very small compared to CdTe QDs, we expect that the CdTe QDs would completely surround the MNP and prevent further attachments. Thus, Ag NPs, which are now covered with CdTe QDs, will become noninteracting among themselves as well as with other SQDs. In such case, the optical response of the resulting sample should be interpreted as a mixture rather than formation of hybrids with different interaction strength between MNPs and SQDs. In the following, we develop the theory of optical response of mixed samples.

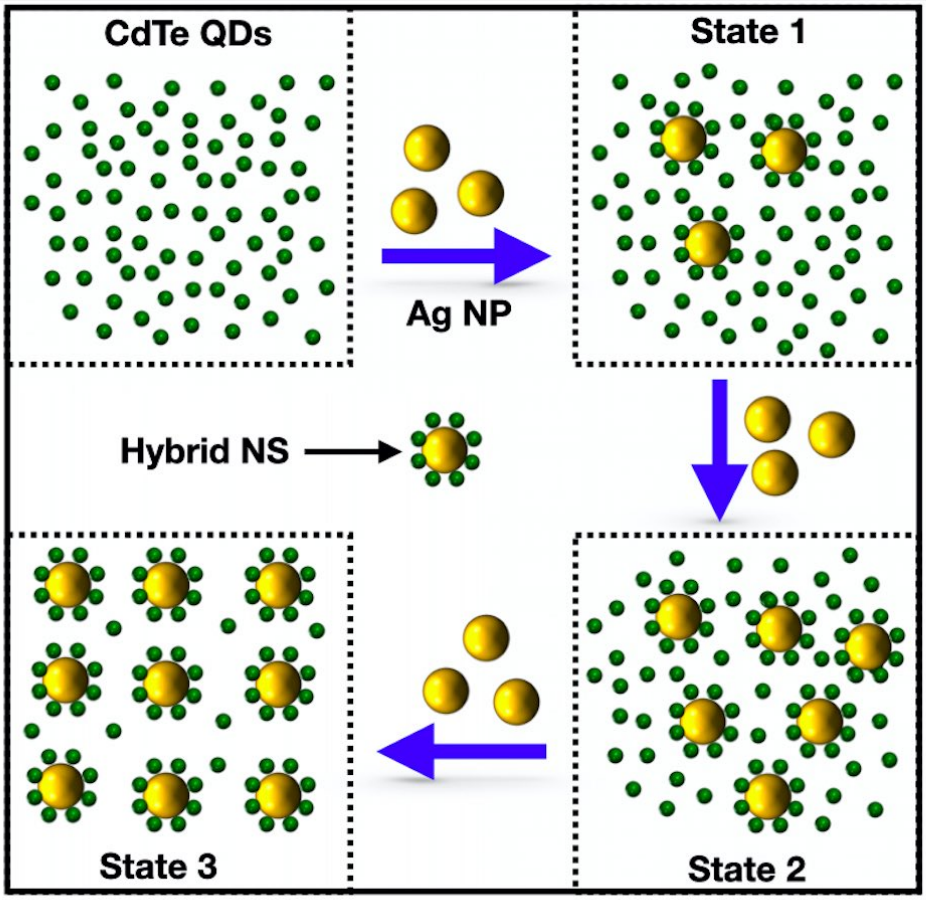

FIGURE 3.4: Schematic of formation of mixed hybrid sample. State of the colloid for three different mixing ratios are shown.

3.2 Theory of Optical Response of a Mixed Hybrid system

Consider the process of formation of HNS by mixing a MNP colloid with a SQD colloid. It is assumed that the individual colloids are of sufficient dilution to be stable and have little or no aggregation. Although the present model can be used for any size and shape of the MNP and SQD, for simplicity and to match with the present experiment, we consider a specific situation when the SQDs are much smaller than the MNPs. Let a small quantity of MNP colloid is added to a colloid containing a larger number of SQDs. Figure 3.4 shows the schematic of the process of formation of HNS. The hybrid will form by self-organization which depends on the properties of individual particles and the corresponding capping agents. Due to their relatively small size, several SQDs will get attached to the surface of a single MNP. Since individual SQDs are capped, once the MNP is covered fully, further attachment of SQD will be prevented. The resultant mixed sample will then have the excess unattached SQDs and the hybrid MNP-SQD nanostructures (Stage 1 of Fig.3.4). If more number of MNPs are added, the similar process will follow and the number of HNS in the mixed colloid would increase (Stage 2) until almost all the SQDs are utilized in the formation of hybrids (Stage 3). We propose that up to this stage only one type of HNS is formed. By stopping this process at different stages, it is possible to get mixed colloids with varying ratio of HNS and SQDs.

The optical response of such a mixed sample can be evaluated as follows. Let R_D and R_P be the optical response of the individual colloidal solution of SQDs and MNPs, respectively. Let Q_D and Q_P be the optical response of a single SQD and a single MNP, respectively. In a dilute sample, where the interaction between individual entities can be neglected, the optical response of the colloid can be expressed as

$$R_D = N_D Q_D, \quad \text{and} \tag{3.1}$$

$$R_P = N_P Q_P, \tag{3.2}$$

where N_D and N_P are the number densities of SQDs and MNPs in their respective colloids. Consider a sample prepared by mixing the SQD colloid with MNP colloid in a ratio γ. Here, γ is the ratio between the volume of the MNP colloid (V_P) to that of the SQD colloid (V_D). Let n be the average number of SQDs that join with an MNP to form a single HNS. Each MNP will result in the formation of one HNS. As stated above, once formed, the HNS will not interact further with the remaining

SQD's. The response of the mixed colloid can be expressed as,

$$R_{M\gamma} = \frac{(N_D - n\gamma N_P)\, Q_D + \gamma N_H Q_H}{(1+\gamma)}. \tag{3.3}$$

Here Q_H is the response of a single HNS and N_H is the number density of HNS. Note that in the present case the total number of HNS in the mixed solution will be the same as the number of MNPs added in the mixture. In a dilute dispersion, the optical response of a colloid depends on the optical response of the individual entity and its number density. The interaction between the MNP and the SQDs will define the response of a HNS, Q_H. In case of other hybrid systems where the physical interactions and the number of particles attached to form a hybrid (n) are different, Q_H will also be different correspondingly. The value of n is decided by the nature of bonding between the MNP and SQDs and hence depends on the capping agents, the shape, size, and material of the MNPs and SQDs. In the present case, since we are considering the regime where the number of CdTe QDs are always in excess, thus n will remain constant.

In the following we show that the optical response of the mixed colloid with a given ratio ($R_{M\gamma'}$), where γ' is any given mixing ratio, can be expressed in terms of spectra of the pure QDs colloid and a mixed sample with another γ value. For known R_D and $R_{M\gamma}$, $R_{M\gamma'}$ can be written as,

$$R_{M\gamma'} = rR_D + sR_{M\gamma} \tag{3.4}$$

where r and s are arbitrary constants. Using Eq.3.3, we can write,

$$\frac{(N_D - n\gamma' N_P)\, Q_D}{(1+\gamma')} + \frac{\gamma' N_P Q_H}{(1+\gamma')} = \left[rN_D + \frac{s\,(N_D - n\gamma N_P)}{(1+\gamma)} \right] Q_D + \frac{s\gamma N_P Q_H}{(1+\gamma)}. \tag{3.5}$$

Since Q_D and Q_H are independent parameters, their coefficients on left and right side should be equal.

$$\frac{1-\beta\gamma'}{1+\gamma'} = r + s\frac{1-\beta\gamma}{1+\gamma} \tag{3.6}$$

$$\frac{\gamma'}{(1+\gamma')} = \frac{s\gamma}{(1+\gamma)}. \tag{3.7}$$

We have defined a "hybrid structure parameter", β as the ratio between nN_P and N_D. Using these above two equations the constants r and s can be expressed in terms of the mixing fractions as,

$$s = \frac{\gamma'}{(1+\gamma')}\frac{(1+\gamma)}{\gamma}, \tag{3.8}$$

$$r = \frac{1}{(1+\gamma')}\left[1-\frac{\gamma'}{\gamma}\right]. \tag{3.9}$$

Interestingly, the constants r and s are related to each other by,

$$r + s = 1 \tag{3.10}$$

For a particular mixing ratio (Γ) where all the SQDs are used up for the formation of HNSs, contribution of SQDs to the optical response of HNS colloid should vanish. Hence the coefficient of Q_D on the right hand side of Eq.3.3 should be zero,

$$N_D - n\Gamma N_P = 0. \tag{3.11}$$

Thus, the mixing ratio of a pure hybrid sample will be $\Gamma = 1/\beta$. For sample containing only HNSs, the microscopic "hybrid structure parameter" can be directly related to the macroscopic mixing ratio. Addition of excess MNPs beyond this ratio would result in the formation of HNSs with partially covered MNPs. At this stage, n, the number of SQDs getting attached to the MNP will change with the mixing ratio and the optical response of the mixed sample will not follow the relation3.4 and can be checked by whether $r + s$=1. In some cases, the unsaturated structures (not fully covered with SQDs) can join together forming larger aggregates destabilizing the entire colloid. Formation of such large aggregates has been observed experimentally by other authors also[70, 75]. By estimating the number density of particles (N_D and N_P) in the original colloids and by identifying Γ, it is possible to estimate the number of SQDs per MNP utilized to form a HNS. It may be noted that, in general, the above model applies for a mixture that is formed by any two kinds of entities and not restricted to MNP or SQD and can also be used for responses other than optical. If the trend proposed here is not followed by the optical response of a mixed sample, it implies that the hybrid forming at each mixing ratio has a different superstructure and hence has a different optical response.

In general, it is possible that the response of one of the entities in the mixture is zero. Such a situation can arise if the physical interaction between MNP and SQD is such that the hybrid does not emit any PL. For such cases, the response of the mixed colloid can be written as

$$R_{M\gamma} = N_D \frac{(1-\gamma\beta)}{(1+\gamma)} Q_D. \tag{3.12}$$

Using Eq.3.2, we can write,

$$\frac{R_{M\gamma}}{R_D} = \frac{(1-\gamma\beta)}{(1+\gamma)}. \tag{3.13}$$

By estimating this ratio from the measured optical response for a given γ, it is possible to estimate “hybrid structure parameter” β. In following section, we analyze our experimental results based on the model proposed here.

3.3 Experimental Results vs Theory of a Mixed Hybrid System

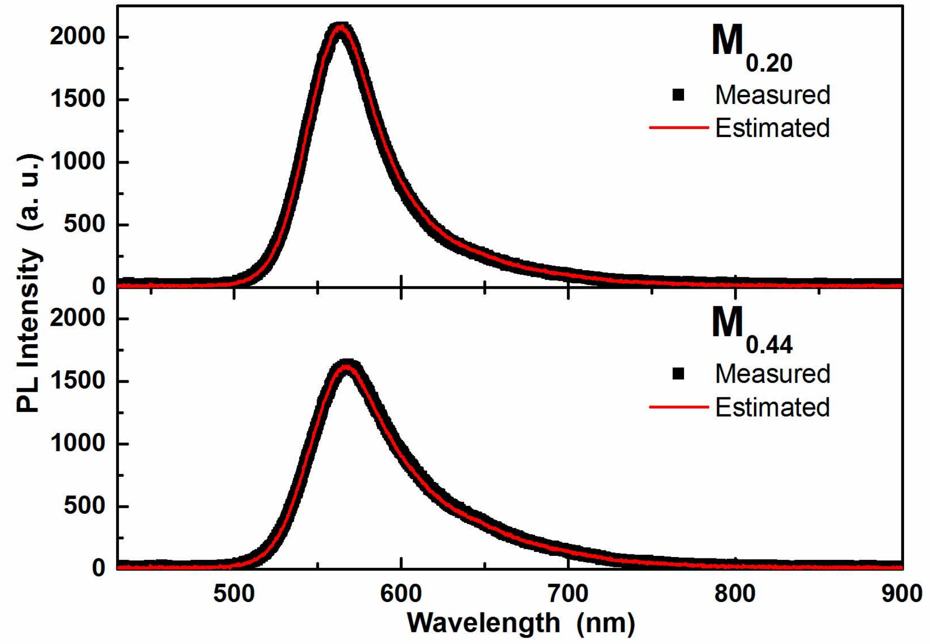

FIGURE 3.5: The PL spectra of mixed hybrid samples $M_{0.20}$ and $M_{0.44}$ along with best fit using Eq.3.4 using experimental PL spectrum of pure CdTe colloid and $M_{0.56}$

If the model of formation of the mixed hybrid proposed in the previous section applies to the Ag-CdTe hybrid nanocolloid system, then the PL of the hybrids prepared with different mixing ratios should be related to each other by Eq.3.4. Using the measured PL spectrum of pure CdTe QD colloid and the PL spectrum of the hybrid $M_{0.56}$, we try to fit the PL spectrum of the intermediate mixtures. Figure.3.5 shows the best fit obtained for the PL spectra of samples $M_{0.20}$ and $M_{0.44}$. The values of coefficients r and s estimated from the mixing ratios and that obtained from the best fit are given in Table-3.1. Since there is no PL spectrum for Ag NPs, therefore R_P is 0 while considering the optical response as PL spectrum. The fact that the PL spectrum of a mixed hybrid sample of a particular mixing ratio could be estimated using that of two other solutions having different mixing ratios and the sum of r and s is nearly one (Table-3.1) in every case, suggests that the proposed model for

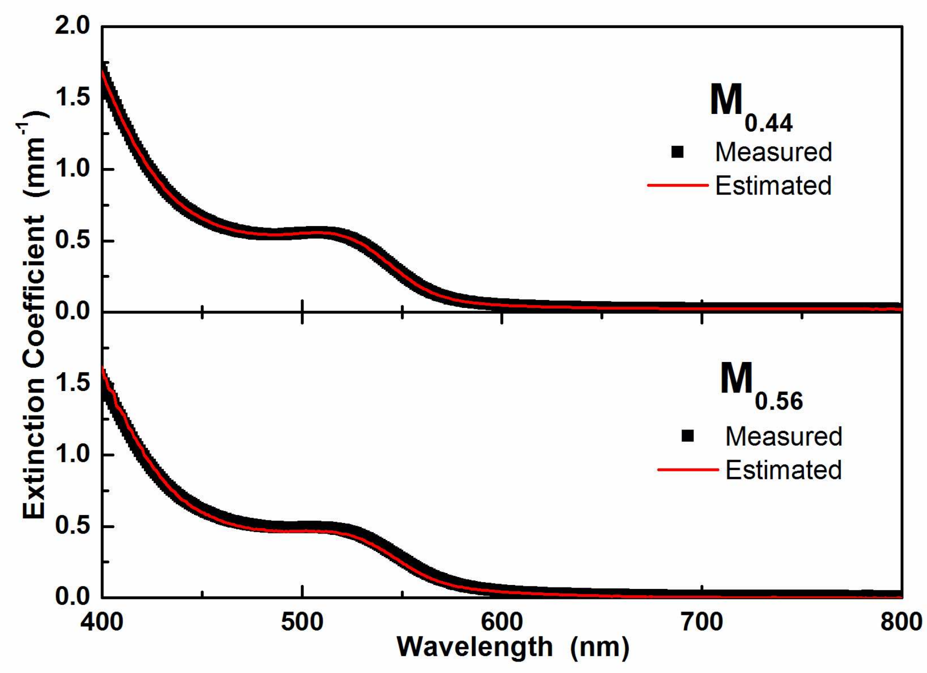

FIGURE 3.6: The extinction spectra of mixed hybrid samples $M_{0.44}$ and $M_{0.56}$ along with best fit using Eq.3.4 using experimental extinction spectra of pure CdTe colloid and $M_{0.20}$

the formation of mixed hybrids works well in the present case. We also performed the similar fitting for the extinction spectra of the mixed colloids. For the same γ and γ', the best fit obtained from fitting the extinction spectra is similar to that of PL fitting (Table-3.1). This confirms that the model correctly predicts the ratio of mixing irrespective of the optical process under study. To further confirm the proposed model, we have performed similar fit for the extinction spectra with other mixing ratios. In this case we have used $M_{0.20}$ and pure CdTe QD colloid to estimate the extinction spectrum of other two mixed hybrid samples. Figure 3.6 shows the best fit curve and the coefficients r and s are also given in Table-3.1. These results once again confirm the model proposed for the formation of mixed hybrids. Thus although the optical response of the hybrids having different mixing ratios looks to be changing gradually, it only reflects the fact that the number density of a basic hybrid unit is increasing with the increasing number of Ag NPs. We find that such a model works well for different Ag-CdTe hybrid systems with stable CdTe

QD colloids having a well distinguishable exciton peak. Any optical responses that satisfies Eq.3.8, Eq.3.9 and Eq.3.10 for every γ, the model is valid and hence the observed change in experiment can be interpreted as number density variation rather than change in interaction between the individual component forming a hybrid.

TABLE 3.1: The coefficients r and s estimated using the mixing ratios as well as that estimated by fitting the experimental optical responses of the mixed hybrid samples.

Optical Response	γ	γ'	Estimated		Best Fit		
			r	s	r	s	$r+s$
PL	0.20	0.56	0.54	0.46	0.49	0.46	0.95
	0.44	0.56	0.15	0.85	0.15	0.87	1.02
Extinction	0.20	0.56	0.54	0.46	0.50	0.49	0.99
	0.44	0.56	0.15	0.85	0.17	0.87	1.04
	0.44	0.20	-0.17	1.17	-0.17	1.17	1.00
	0.56	0.20	-1.15	2.15	-1.25	2.28	1.03

Based on the observation that beyond $\gamma = 0.56$, the nanoparticles show aggregation, we expect that the sample $M_{0.56}$ is the case where nearly all CdTe QDs are consumed for the formation of hybrids. If the number of Ag NPs are further increased then there are not sufficient CdTe QDs to form the same stable HNS. Thus, we propose that the optical response of the sample $M_{0.56}$ corresponds to that of a Ag-CdTe hybrid. From Eq. 3.11), we estimate that n $\sim$ 45, i.e., the hybrid is formed by $\sim$ 45 CdTe QDs attached to one Ag NP. This number is 30% less than that expected if the TGA coated CdTe QDs had covered the citrated coated Ag NP in a single closely packed layer. Thus, by measuring the optical response and by using the model presented here certain features in the hybrid structure can be estimated.

The model proposed above is quiet general and can apply to a mixture of any two entities provided only one kind of hybrid superstructure is formed. This can be ensured in practice by starting with a single entity and gradually increasing the ratio of the other component. The model will also apply to responses other than the linear optical response. For example, the transient optical response of the mixture would also follow the same pattern. It is to be noted that the formation of a new nanostructure is indicated by the extinction spectrum and the proposed model would work irrespective of which new nanostructure was being formed as a result of mixing. For example, even if the MNPs and SQDs combine such that individual particles disappear and a new material is formed, the model presented here will still work since in the model optical response measured by experiment is directly used.

3.4 Summary

To summarize, in this chapter we have shown that if self-assembly of metal- semiconductor HNS takes place when MNP and SQD colloids are mixed, the measured optical response of the sample can be shown to have two components, one arising from the HNS and one from any leftover unattached SQD or MNP species. We have also shown that it is possible to extract the correct optical response of the HNS by performing measurements on a series of samples with varying mixing ratios. By using the method described in this paper, it is possible to determine the optimum mixing ratio at which almost all the particles in the sample would be only HNS. Any study undertaken to understand the properties of the HNS (e.g. interaction between the MNP and SQD, linear, nonlinear and transient optical response of the hybrid etc) should be carried out only on the sample with the optimum mixing ratio that falls under the regime proposed here.

Chapter 4

Static and Ultrafast Optical Response of Two Metal Nanoparticles Glued with a Semiconductor Quantum Dot

A second generation LFE can be created between two closely placed MNPs, known as hot-spot, and by irradiating them with an appropriate wavelength and polarization of incident light. The strength of the field at the gap between the particles is expected to get enhanced by several orders of magnitude higher than that of the applied field. Placing a SQD or an analyte molecule at the hot-spot is an essential step towards harnessing the enhanced field for various applications. Using the method described in previous chapter, it is now possible to determine the mixing ratio at which the mixture contains only the hybrid of unique structures. In this chapter**, we show that by mixing Ag NP colloid with TGA capped CdTe QD colloid in a particular mixing ratio, it is possible to prepare HNS with CdTe QD stuck in between the two Ag NPs. By comparing the measured extinction spectra during self-organized growth of the HNS with that of the calculated, we explain the process of hybrid formation. Ultrafast pump-probe measurements can provide quantitative

---

This work is published by the author of this thesis as "Static and Ultrafast Optical Response of Two Metal Nanoparticles Glued with a Semiconductor Quantum Dot,", **Sabina Gurung, Asha Singh, Durga Prasad Khatua, Himanshu Srivastava, J Jayabalan, Photonics and Nanostructures-Fundamentals and Applications, **2020**, 43,100869.

information regarding complex processes that occurs between the metal and semiconductor nanocomposites. Using ultrafast transient transmission measurements, it has been shown that the carrier dynamics in the hybrid colloid is effected only when probed by a light that generates a high field in between Ag NPs. The method demonstrated here to place the semiconductor QD in between the two Ag NPs is an important step in the area of colloidal self-assembly and for application of gap plasmon in plasmonic sensing, optoelectronics, energy-harvesting, nanolithography and optical nano-antennas.

4.1 Measured Time Evolution of Extinction Spectrum of the Mixed Colloid

The individual constituents of the HNS, citrate capped Ag NPs and TGA capped CdTe QDs dispersed in water, were prepared separately by wet-chemical methods[3, 96, 110]. The procedure followed for the preparation of this individual colloids and hybrid have been discussed in Chapter 2. Figure. 4.1(a) shows the extinction spectrum of the individual Ag NP colloid and CdTe QD colloid. The extinction spectrum of the Ag NP colloid shows a single peak at 413 nm, which corresponds to the LSPR of small silver nanospheres dispersed in water[20, 106]. The extinction spectrum of the CdTe QD colloid shows an exciton peak at 635 nm due to 1s(e)-1s(h) transition[107, 111]. For structural characterization, few drops of these samples were dried on a mica substrate, and the topography of the surface was measured using an AFM. Some representative AFM images of the individual colloids are shown in Fig.4.2. The AFM images that corresponds to individual Ag NP colloid and CdTe QD

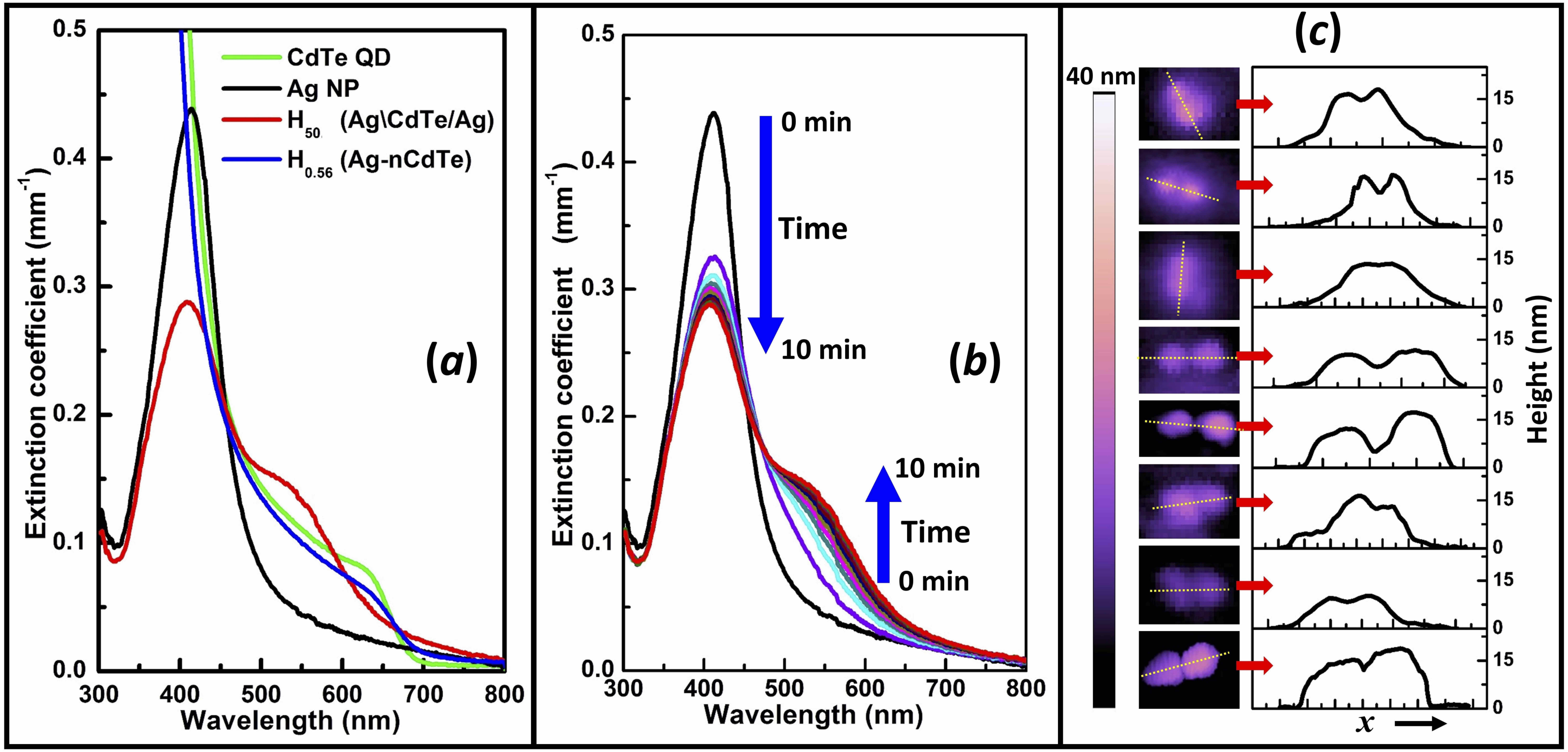

FIGURE 4.1: Static optical and structural characterization of individual, mixed and hybrid colloids: (*a*) Extinction coefficient of CdTe QD, Ag NP, H_{50} hybrid and $H_{0.56}$ hybrid colloids. (*b*) The time evolution of extinction spectrum of the mixed colloid from just after mixing to about 10 min. (*c*) Representative AFM images of HNSs present in the H_{50} hybrid colloid. x is the distance along the substrate surface.

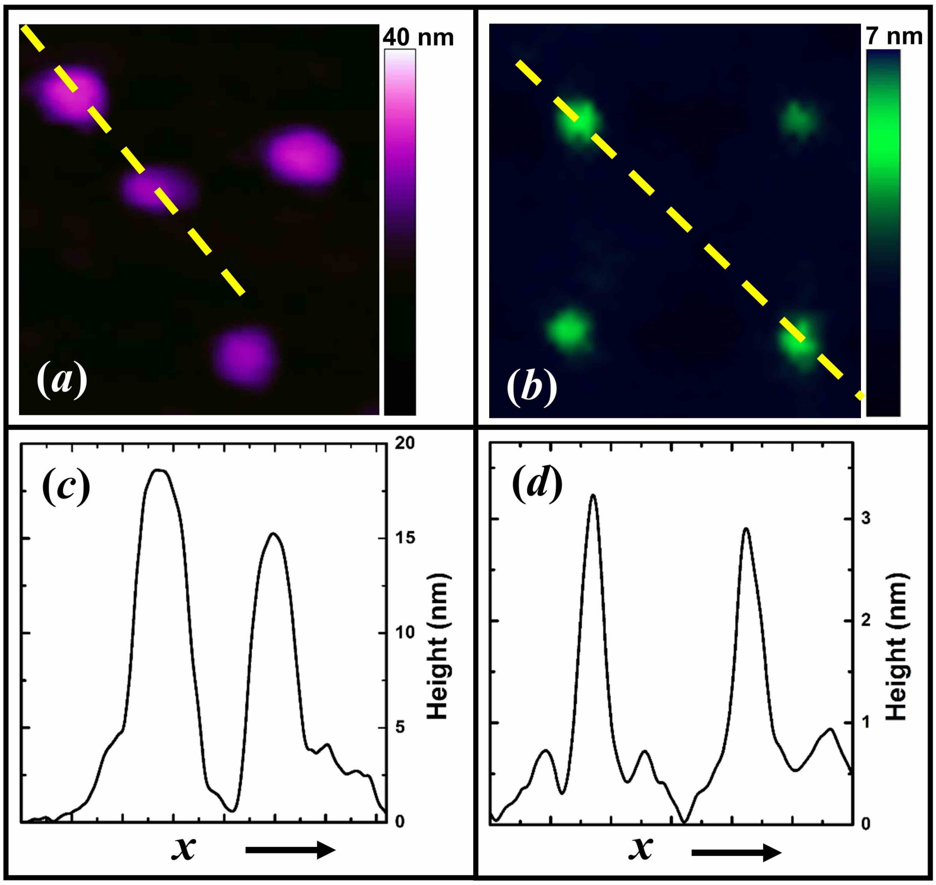

FIGURE 4.2: AFM images of (*a*) Ag NPs and (*b*) CdTe QDs. The height profile along the straight lines marked in the AFM images are plotted in (*c*) and (*d*) respectively..

colloid show the presence of mostly well-separated particles. The average diameter of the Ag NPs and CdTe QDs measured using the height profile from these AFM images is 17 nm and 3.5 nm, respectively.

At the mixing ratio of $\gamma = 50$, there are about two Ag NPs for each CdTe QDs in the mixed colloid (see Appendix-I for detail). The concentration of SQDs and MNPs in the individual colloids can be estimated by using procedures reported by Yu *et al.* and Sriram *et al.* respectively[107, 112]. The estimated number densities of CdTe QDs and Ag NPs in the corresponding individual colloids used in the preparation of hybrid are 4.8×10^{15} mL^{-1} and 1.2×10^{14} mL^{-1} respectively. These densities are also in agreement with the 2:1 number ratio of Ag NPs and CdTe QDs. The hybrid sample, H_{50}, was prepared by mixing CdTe QD colloid with Ag NP colloid

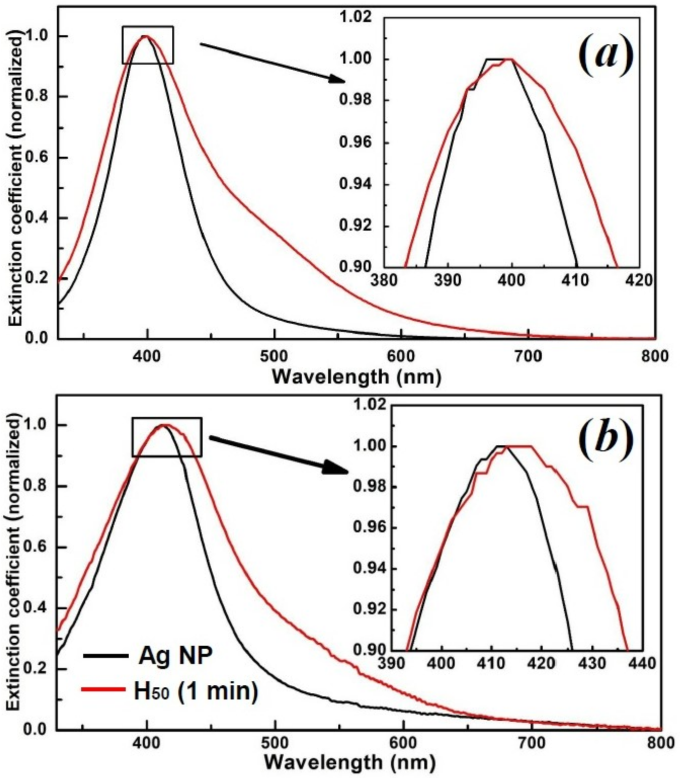

FIGURE 4.3: The extinction spectra of bare Ag NP colloid and mixed colloid containing Ag NPs and CdTe QDs 1 min after mixing (*a*) and (*b*) shows representative of two different attempts of preparing the hybrid with different sets of Ag NP and CdTe QD colloids. Inset shows the enlarged graph near the peak. A small shift in the LSPR peak can be seen due to the increase in the width more towards the red-side of the spectrum.

at a mixing ratio of γ = 50. Immediately after the addition, the LSPR peak red-shifts slightly and at the same time the extinction peak height reduces to about 74% of that before addition (Fig.4.1(*b*)). Although the red-shift is very small, repeated preparation shows that the red-shift does occur at about 1 min after mixing (Fig.4.3). Over the period of the next few minutes, another peak appears on the red-side. For example, the spectrum of the sample taken after 2 min could be fit well with two Gaussian peaks (Fig.4.4(*a*)). From 2 min to 10 min, the original LSPR peak blue-shifts and continues to reduce in strength. Whereas the longer wavelength peak red-shifts and grows (Fig.4.1(*b*)). After about 10 minutes, the mixed colloid shows no further change in the spectrum. The final stable hybrid sample thus formed (H_{50})

has peaks at 410 nm and 535 nm with strength 65% and 32% of that of bare Ag NP colloid, respectively. Note that the sample would be continuously evolving during the measurement of the spectra. Nevertheless, the measured spectra can be used for gaining insight into the hybrid formation process.

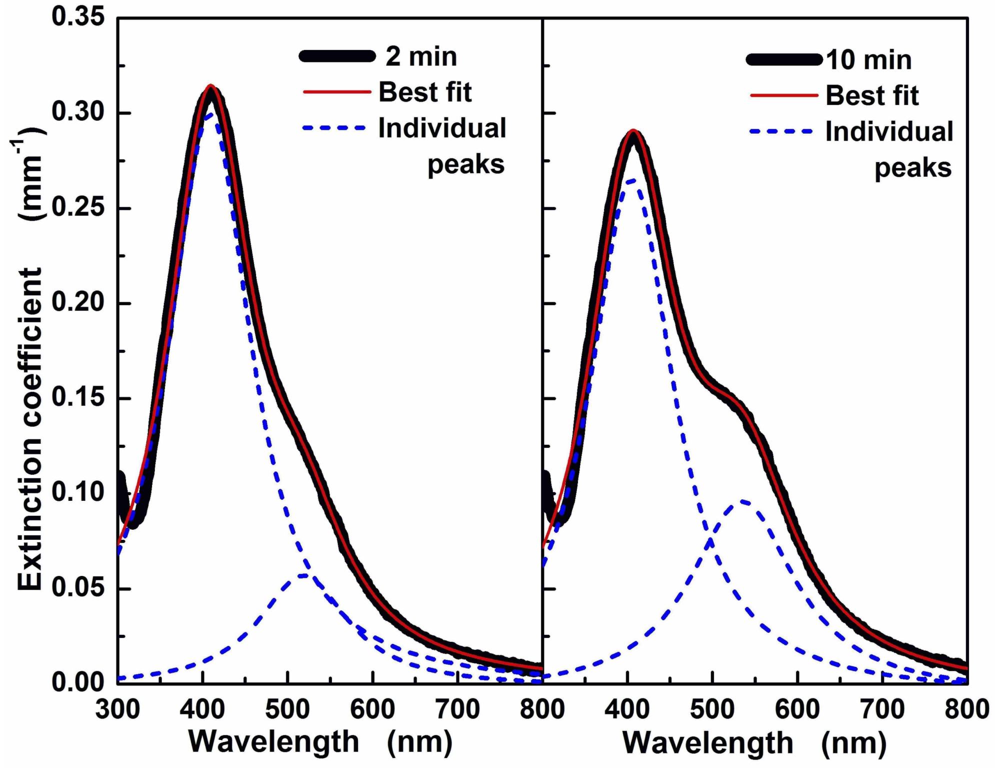

FIGURE 4.4: Extinction spectrum of the mixed sample (black lines) after (*a*) 2 min and (*b*) 10 min. Best fit to these experimental spectra using two Gaussian peaks (red lines). The contribution from individual peaks are also shown (blue lines).

A self-organized growth of Ag-CdTe HNS is expected in the mixed sample because of the tendency of TGA to get attached to the surface of Ag NP[69, 71, 89]. As the TGA is already attached to the CdTe QD, these QDs are also brought in close proximity to the Ag NP[69, 71, 89]. When Ag NP and CdTe QD colloids are mixed in a ratio of $\gamma = 0.56$, HNSs of Ag NP surrounded by nearly 45 CdTe QDs ($H_{0.56}$ or Ag-nCdTe) are formed[89]. Once the CdTe QDs surround the Ag NP completely, it prevents further attachment of CdTe QD to the Ag NP, thus making the final hybrid structure stable. The extinction spectrum of the $H_{0.56}$ sample thus formed is also shown in Fig.4.1(*a*) for comparison. Clearly the extinction spectrum of this $H_{0.56}$

sample is very different from that of the H_{50} sample. The $H_{0.56}$ has an increasing absorption strength towards UV similar to that of bare CdTe QD colloid. On the other hand the H_{50} sample shows a dip in absorption around 320 nm, which resembles more of an Ag NP colloid. The AFM images of the H_{50} sample dried on mica shows several twin particles of each having nearly 17 nm height (Fig.4.1(c)). Based on the height, each of these particles should be the Ag NPs present in the mixed colloid. Further, based on the number density ratio and the tendency of TGA to get attached to the Ag surface, we propose that in the final hybrid colloid, there are nanostructures with two Ag NPs attached to a single CdTe QD.

We find that if a mixed hybrid sample was prepared with a mixing ratio γ higher than 50, stable colloids do get formed. The final extinction spectrum of these hybrid colloids ($\gamma > 50$) has an extinction spectrum that looks similar to that observed in the intermediate stages (Fig.4.1(b)). For these γ values, there will not be enough CdTe QDs to join all the Ag NPs leaving several unattached Ag NPs along with few H_{50} hybrids[89]. On the other hand, if the mixing ratio is lower than 50, aggregated nanostructures were found to settle down at the bottom of the sample. This can be explained by the presence of excess CdTe QDs, which can link several H_{50} forming large chain-like structures that eventually become heavy enough to settle down[113, 114].

4.2 Time Evolution of Extinction Spectrum of Mixed Colloid

To understand the time evolution of the measured extinction spectra after mixing and to further understand the structure of the final hybrid formed, optical response of various Ag-CdTe HNSs were numerically calculated using T-matrix technique (Fig.4.5). T-matrix is a numerical method for computing the optical response of a collection of spherical particles, the detail has been discussed in Chapter 2 [103,

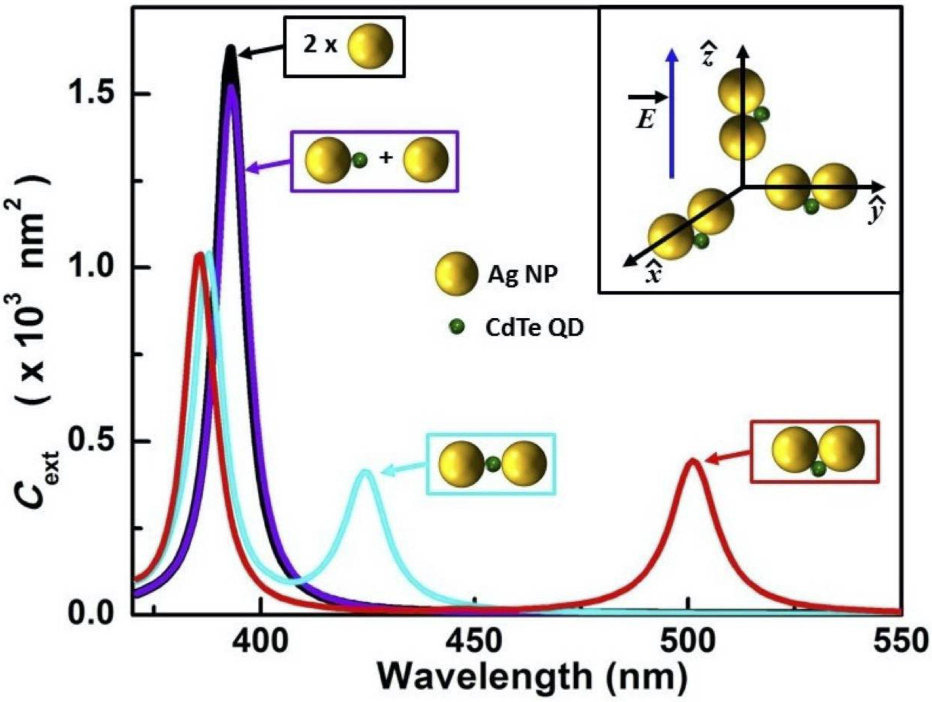

FIGURE 4.5: Calculated extinction cross-section of two non-interacting Ag NPs, attached Ag-CdTe particles, chain of Ag-CdTe-Ag particles and touching Ag-Ag particles with CdTe QD on one side.

104]. For Ag NPs of the size of the order of 17 nm, quantum confinement effects can be neglected, and hence experimental bulk dielectric constants were used for the optical response calculations[115]. On the other hand, the dielectric constant of a CdTe QD of size 3.5 nm will be substantially different from that of its bulk because of the quantum confinement effect[102]. The dielectric constant of CdTe QD was estimated using the method reported by Marcelo Alves-Santos *et al.* and has already discussed in Chapter 2[102]. In the colloidal solution, it is expected that particles will be oriented in all possible directions. To mimic that situation with minimal computational cost, the extinction spectrum is estimated by averaging the responses calculated for a given field direction and particles aligned along the three Cartesian directions (see inset of Fig.4.5)[32, 104].

The calculated extinction cross-section of the Ag NP shows a single peak at 393 nm (Fig.4.5). To compare with the other structures, where there are two Ag NPs are involved, C_{ext} of the two isolated Ag NPs (same as the cross-section of single

Ag NP multiplied by two) is plotted in Fig.4.5. Once the Ag NP and the CdTe QD colloids were mixed, the most possible situation would be that a single CdTe QD will get attached to a single Ag NP. The second Ag NP would not have joined yet. To mimic such a situation, we have calculated C_{ext} of a single CdTe QD attached with an Ag NP and another Ag NP placed sufficiently away from it. The C_{ext} thus obtained shows a red-shift of about 1 nm when compared to that of isolated Ag NP. Further, the peak height also reduces to about 90% of that of two isolated Ag NPs. Attaching a higher refractive index material to a metal NP is known to red-shift its LSPR peak[33, 116]. The changes in C_{ext}, the red-shift and the reduction in peak strength, when CdTe is attached to one of the Ag NP matches well with the observed change in the extinction spectrum measured at nearly a minute after mixing Ag NP and CdTe QD colloids (Fig.4.1(b)). When another Ag NP is attached to the other end of CdTe QD which is already attached to an Ag NP, it will result in the formation of a linear Ag-CdTe-Ag structure. The C_{ext} of this structure shows a new peak at 424 nm and the original LSPR peak, which was at 393 nm blue-shifts by 5 nm to 388 nm. These LSPR peaks, 424 nm and 388 nm, appear when the field is aligned along the line joining the centers of the two Ag spheres (longitudinal axis) and perpendicular to it (transverse axis) respectively (Fig.4.5). Fitting the measured extinction spectrum at 2 min after mixing shows a double peak structure, which matches well with that of C_{ext} of Ag-CdTe-Ag (Fig.4.4). The final spectrum (> 10 mins) of the hybrid has a second peak at 535 nm which is much more red-shifted than that calculated for the Ag-CdTe-Ag structure. Although capping prevents Ag NPs to join together, once brought in close proximity to each other, the metal NP do tend to join and restructure themselves[117–119]. Thus, once joined by the CdTe QD it is possible that over time the linear Ag-CdTe-Ag hybrid changes its structure to that with two Ag NPs touching each other with CdTe QD pushed to one side (Ag\CdTe/Ag) as shown in Fig.4.5. The calculated C_{ext} of Ag\CdTe/Ag hybrid match closer to the experimentally observed final extinction spectrum which has peaks at 408 nm and 535 nm (Fig.4.1(*a*)). When two metal NPs are brought close to each other in nanometer length scale, the two independent plasmon of each metal NP start to interact with each other. This leads to hybridization between the two free plasmon modes of metal NPs. The strength of this hybridization determines shifts of the plasmon energies which depends on the particle separation. When the particles separation is large, the plasmon resonance of two Ag NPs is same as that of single particle. As the separation is reduced, the interaction between the particles starts leading to shifting of energy levels to bonding and antibonding plasmon. The higher energy mode i.e peak at 408 nm corresponds to the LSPR originating when the field is aligned along the transverse axis (T-LSPR) while the lower energy mode at 535 nm peak corresponds to the LSPR when field is aligned along the longitudinal axis (L-LSPR). Another effective tool to understand the origin of various plasmon peaks arising in a collection of interacting small metal NPs like dimer, trimer, etc., is plasmon hybridization model[120]. However, this model cannot in general be used for estimating the optical response of metal NPs in presence of CdTe QDs [121]. The result of T-Matrix calculations (which is applicable for a collection

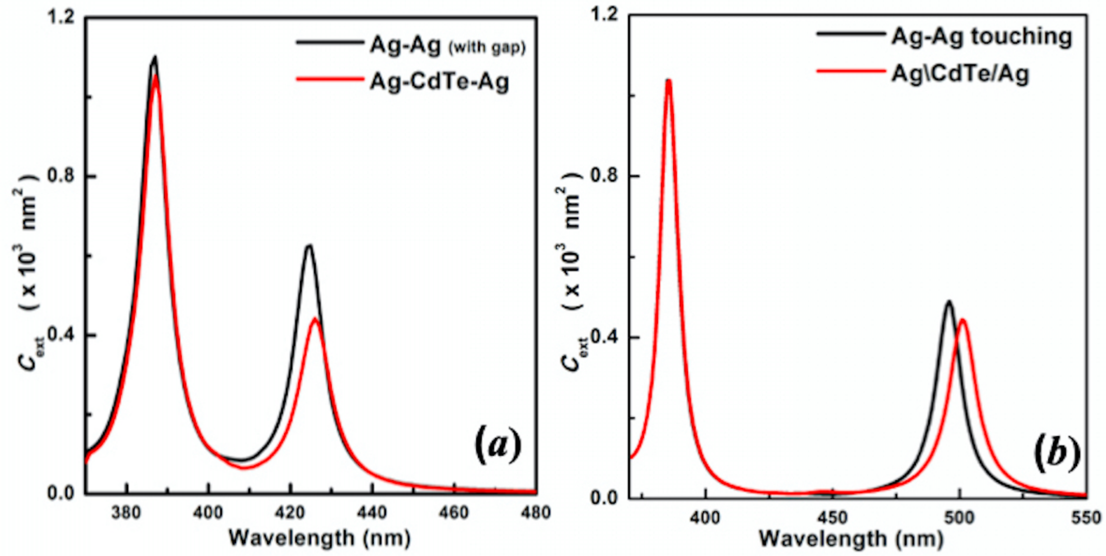

FIGURE 4.6: Calculated extinction cross-section of Ag-CdTe-Ag (left) and Ag\CdTe/Ag (right) with and without the CdTe QD. The gap between the two Ag NPs without CdTe QD (left) is taken to be same as that of the original structure..

of spheres of any materials[104]), shows that the extinction spectrum of Ag-CdTe-Ag and Ag\CdTe/Ag is slightly different from that of the corresponding structures without CdTe QD (Fig.4.6). Although plasmon hybridization model could be used to understand the final response of interaction between metal NPs, more realistic modes and resonance of the dimer like structures in the presence of CdTe QDs requires calculation like T-matrix or finite-difference time-domain. Comparing the

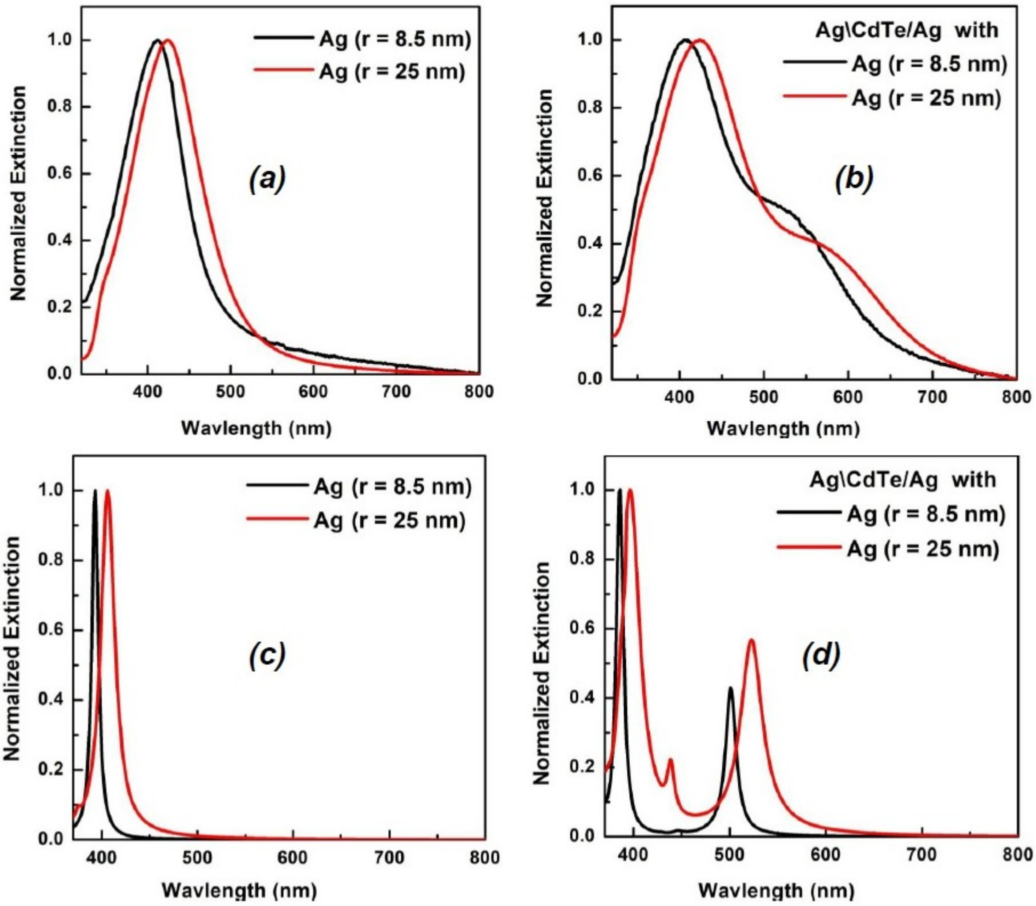

FIGURE 4.7: Measured and estimated extinction spectrum for two different Ag NP sizes. Measured extinction spectrum of (*a*) Ag NP colloid with small and large Ag NP and (*b*) Ag\CdTe/Ag hybrid colloid with small and large Ag NP. Calculated extinction spectrum of (*c*) Ag NP and (*d*) Ag\CdTe/Ag with Ag NP radius, $r = 8.5$ nm and $r = 25$ nm.

measured temporal evolution of the extinction spectra (Fig.4.1(*b*)) and the calculated optical responses of the Ag NP and HNS (Fig.4.5), the growth of the final HNS can now be explained. Just after mixing, CdTe QD gets attached to Ag NP forming a large number of HNS each with one Ag NP and one CdTe QD. Such an Ag-CdTe

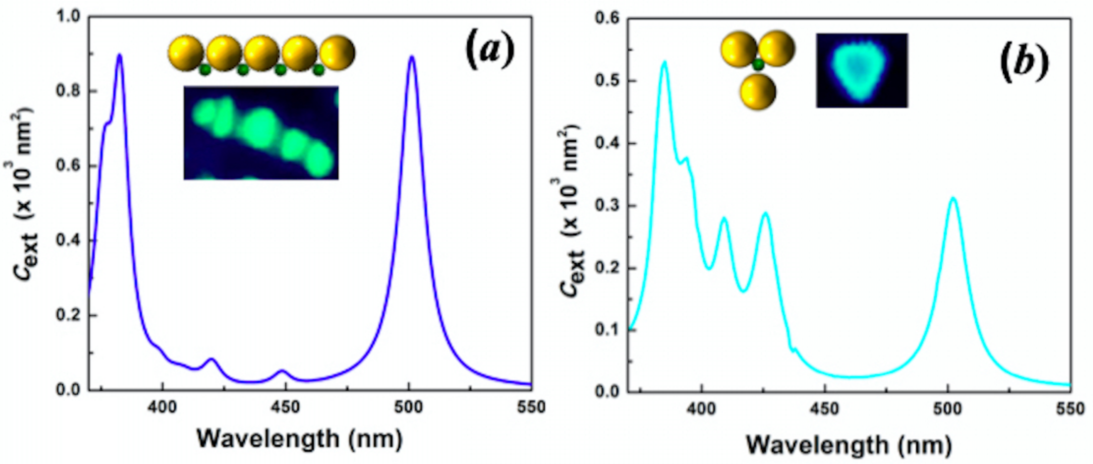

FIGURE 4.8: Calculated extinction cross-section of (*a*) a chain like structure formed with Ag NPs and CdTe QDs (as shown in the inset) and (*b*) a triangle like structure formed with three Ag NPs and a CdTe QDs (as shown in the inset). The inset in these figures also shows their corresponding schematic structures.

hybrid structure coexists in the colloidal solution along with an almost equal number of unattached Ag NPs. This is indicated by the observed small red-shift and reduction in strength of the LSPR peak when measured 1 min after mixing (Fig.4.3). As time progresses, another Ag NP also gets attached to the Ag-CdTe nanostructure to form an Ag-CdTe-Ag linear HNS. The observed second peak on the red-side of the extinction spectra measured in the first few minutes indicates the formation of such structures. Followed by this, the linear Ag-CdTe-Ag structure realign themselves to form a Ag\CdTe/Ag structure. This explains the observed red-shifting of the long-wavelength peak, which finally settles down at 535 nm. To further confirm these observations, we have also prepared Ag\CdTe/Ag hybrids with larger Ag NPs with a diameter of nearly 50 nm (Fig.4.7). Once again, the experimental results match well with that of the calculated spectra using T-matrix. Thus the final stable colloid, H_{50} should have hybrid NPs of Ag\CdTe/Ag structure. The size of the CdTe QD is much smaller and is now in between two large Ag NPs, thus further attachment of Ag NP to the same CdTe QD is prevented. Because of the limitation in resolution, the AFM image could not resolve the presence of small CdTe QD sitting between the larger Ag NPs. Hence the AFM images of the Ag\CdTe/Ag hybrid could only show a Ag NP dimer-like structure (Fig.4.1(*c*)). In some of the AFM images of H_{50}, we also find few hybrid structures with Ag NPs attached to each other in a triangular formation and few Ag NPs in chain-like structure (inset of Fig.4.8). The T-matrix calculation shows that these triangular and chain-like structures have a very different extinction spectra than those observed in the experiment (Fig.4.8). TEM could also be used for studying the structure of final self-aggregated Ag\CdTe/Ag nanostructures. Figure. 4.9 shows some of the TEM images of the colloid containing Ag\CdTe/Ag HNS. The TEM images of Ag\CdTe/Ag HNS clearly shows the presence of a smaller particle (size in the range of CdTe QDs) in between two larger-sized particles (size of the order of Ag NPs) which matches well with that of expected from optical characterization (Fig.4.9).

The efficiency of Ag\CdTe/Ag nanostructure formation in this synthesis process could be obtained by the number density of nanostructures observed in AFM images as well as by comparing the calculated extinction spectra of the individual nanostructures with that of experimentally measured hybrid colloid. Note that the AFM measurements were performed on a mica substrate over which few drops of the hybrid colloid is dried. The structure of the nanoaggregates found on the mica substrate could depend on the number density of particles in colloid, the properties of the colloid and substrate and also on the drying process itself. Thus, AFM image only gives a representation of the nanostructures floating in the colloidal solution. On the AFM images, we find that the ratios of monomers:dimers:trimers:chain to be 4:16:2:1. The T-Matrix calculation shows that in case of dimers, the ratio between the peak strengths of the two LSPR peaks is 0.43. For trimer and chain of particles, the ratio between the two strongest peaks (which are also close to the LSPR peaks of dimer) is 0.6 and 1 respectively. While for the monomer there should not be any longer wavelength peak. The ratio between the two peaks in the experimental extinction spectrum of Ag\CdTe/Ag hybrid is 0.49, which is close to that of dimer. Meanwhile, an estimated spectrum of mixed colloid containing monomers, dimers etc in the number ratios measured by AFM image is completely dominated by that of dimers.

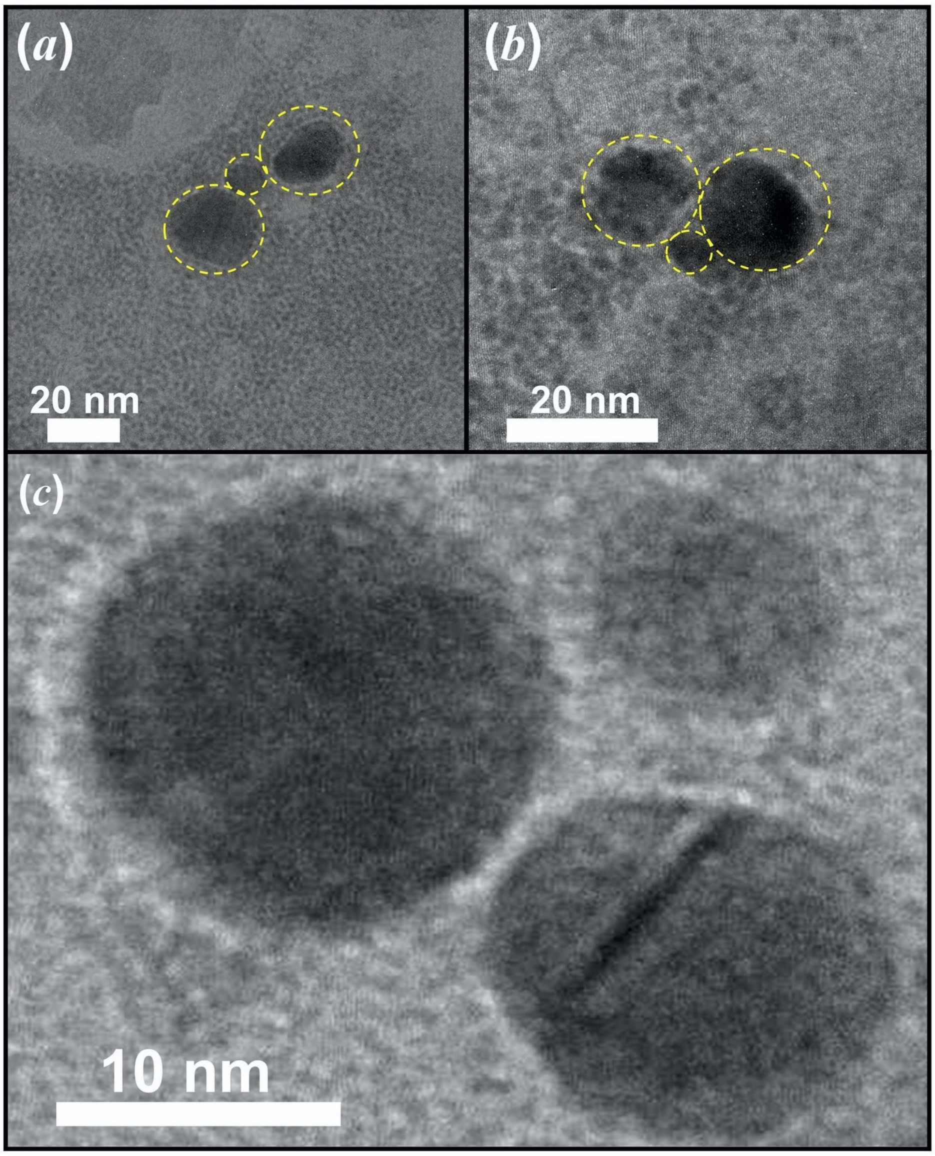

FIGURE 4.9: TEM images of Ag\CdTe/Ag HNSs.

4.3 Ultrafast Response of Ag\CdTe/Ag Hybrid Nanostructure

Figure. 4.10 and Figure. 4.11 shows the transient transmission signal ($\Delta T/T$) measured for the bare Ag NP and Ag\CdTe/Ag hybrid when probed at 408 nm and 550

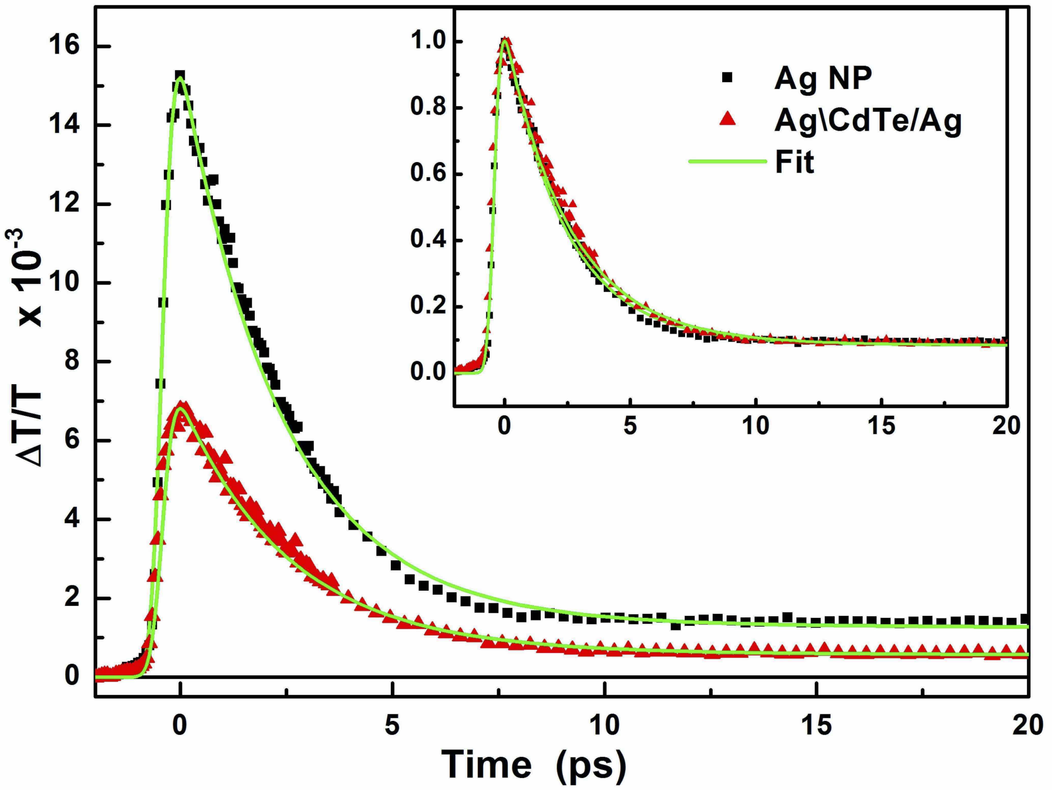

FIGURE 4.10: The measured transient transmission of Ag NPs and Ag\CdTe/Ag colloidal samples when excited at 400 nm and probed at 408 nm. Inset shows the same but normalized.

nm, respectively. In all these measurements, the pump wavelength (400 nm) and pump fluence (2.1 μJmm^{-2}) at the sample place were kept the same. For both the samples and at both probe wavelengths, the magnitude of $\Delta T/T$ ($|\Delta T/T|$) increases, reaching a maximum by about 400 fs. With further increase in the pump-probe delay, $|\Delta T/T|$ starts recovering, reaching a very low value by about 20 ps. Further, we find that sample containing bare CdTe QD colloid of concentration similar to that used in the preparation of the Ag\CdTe/Ag hybrid colloid did not show any measurable $\Delta T/T$ signal.

The origin of the ultrafast optical response of the bare metal NP colloid has been reported by several groups[85, 122–124]. When an ultrashort pulse excites a metal NP at its LSPR, the free-electrons in the particles are set to oscillate in phase with

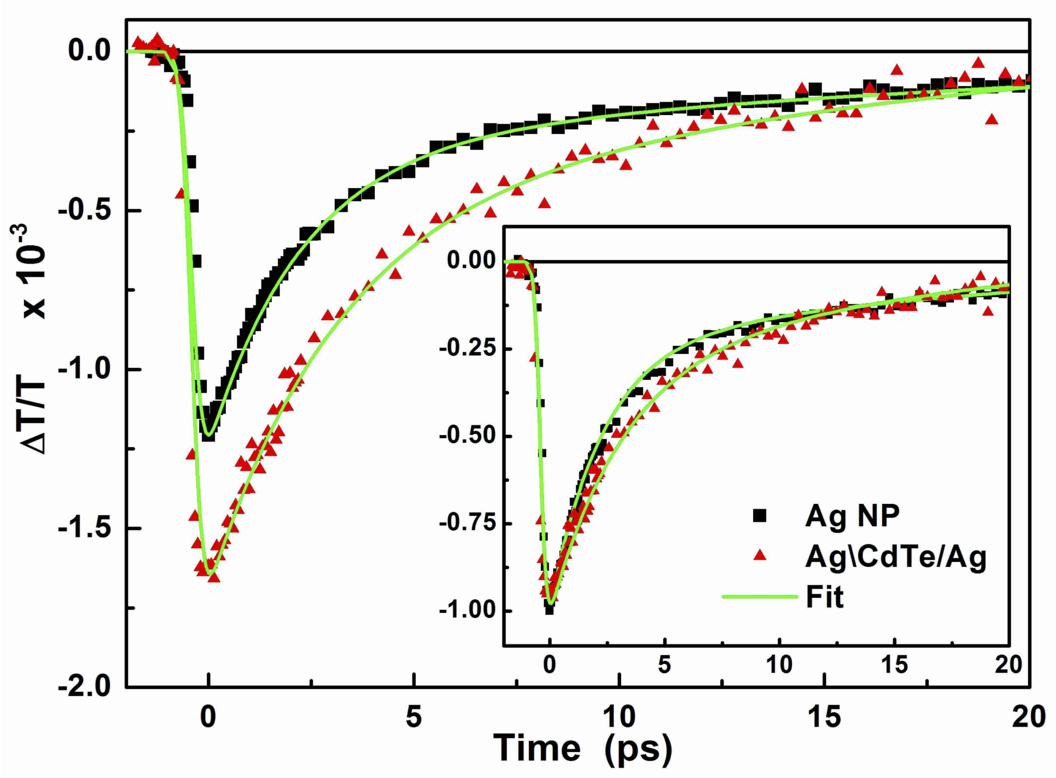

FIGURE 4.11: The measured transient transmission of Ag NPs and Ag\CdTe/Ag colloidal samples when excited at 400 nm and probed at 550 nm. Inset shows the same but normalized.

the applied field. Within the next few femtoseconds, these electrons decay to single-particle states through Landau-damping[122]. The energy distribution among electrons at this stage will be non-thermal. These electrons relax to a thermalized high-temperature state mainly through electron-electron scattering by about a few hundreds of femtoseconds[123]. With the increase in temperature of free-electrons, the real part of the dielectric constant of Ag also increases which red-shifts the LSPR peaks[85, 123, 124]. This shift causes a change in the transmission of a metal NP colloid. The peak change in the transient transmission occurs at the time when there is a maximum change in temperature of the free-electrons. In the present case of bare Ag NP colloid, when excited at 400 nm, the peak in $|\Delta T/T|$ occurs nearly after 400 fs irrespective of probe wavelength. Further, the red-shift of LSPR will cause an increase in transmission, when probed at 408 nm (blue-side of LSPR), and reduction in transmission when probed at 550 nm. Thus, the difference in probing wavelength with respect to LSPR causes the change in the sign of the measured $\Delta T/T$ in the case of Ag NP colloid (Fig.4.10 and Fig.4.11).

At the end of thermalization, the temperature of free-electrons is much higher, whereas the lattice still remains almost at room temperature. Over a time of next few picoseconds, electron-phonon interaction leads to the thermalization of electrons and lattice to a much lower temperature. This is because the specific heat capacity of the lattice is much higher than that of electrons. The thermalization process of electrons and lattice can be quantitatively understood using two-temperature model[85, 123, 124]. However, the two-temperature model would not be, in principle, directly applicable for HNSs. In the present case, because HNSs are also understudy, the complete temporal evolution of $\Delta T/T$ was fitted to,

$$F(t) = \frac{1}{2}\left[\mathcal{E}\left(t/t_r\right) + 1\right]\left[\sum_k A_k e^{-t/t_k}\right] \tag{4.1}$$

where $\mathcal{E}(x)$ is the Gauss error function of x, A_k and t_k are the amplitude and decay time respectively. The best fit to the experimental data using Eq.4.1 is also shown in Fig.4.10 and Fig.4.11. In the case of the bare Ag NP colloid, the best fit value of electron-phonon thermalization time (τ_{ep}) probed at 408 nm and 550 nm are 2.3 ps ± 0.1 ps and 2.4 ps ± 0.1 ps respectively.

Similar to the bare Ag NP colloid, the sign of $\Delta T/T$ of Ag\CdTe/Ag hybrid colloid also changes from positive to negative when probe wavelength is changed from 408 nm to 550 nm. This shows that the transient response of Ag\CdTe/Ag is strongly similar to that of pure Ag NP colloid. To compare the temporal response, $\Delta T/T$ normalized to the peak change in $|\Delta T/T|$ ($|\Delta T/T|_{pk}$) are also shown in the inset of Fig.4.10 and Fig.4.11. The best fit to the decay times of $\Delta T/T$ for Ag\CdTe/Ag hybrid colloid when probed at 408 nm and 550 nm are 2.6 ps ± 0.1 ps and 3.2 ps ± 0.1 ps , respectively. Clearly, when probed at 408 nm, the recovery of change in transmission of the Ag\CdTe/Ag hybrid colloid is slightly slower than Ag NP colloid, whereas, at 550 nm, it takes much longer to recover.

Electron-phonon relaxation takes a longer time in a single crystal Ag NP compared to that of a crystal having twin defects because of the additional scattering of electrons at the lattice defects[54]. In the present case, the lattice quality of the bare Ag NPs and Ag\CdTe/Ag hybrid colloids should be the same because the later is derived from the former. Further, the simple linking of Ag NPs by the CdTe QD should not change its crystal quality. Thus the increase in the relaxation time of the Ag\CdTe/Ag hybrid colloid cannot be explained by assuming a modification in Ag crystal quality. At low temperatures, the electron-phonon relaxation time also depends on its temperature itself, increasing linearly with it. Thus if the increase in the temperature of Ag in the Ag\CdTe/Ag HNS is more, then it can also show an increased electron-phonon relaxation time. The comparison between the measured $|\Delta T/T|_{pk}$ for different samples will be able to give some information about the maximum temperature reached by the free-electrons in the Ag NPs. If $\Delta\varepsilon_m^{'}$ is the small change in real part of dielectric constant due to the change in electron temperature, then the change in transmission at the probe wavelength ($\Delta T/T$) of a colloid having randomly oriented ellipsoidal particle can be written as[85],

$$\frac{\Delta T}{T} = \frac{2\pi p}{3\lambda_{pr}\sqrt{\varepsilon_s}} \sum_{j=x,y,z} Im\left[f_j^2(\lambda_{pr})\right] \Delta\varepsilon_m^{'}(\lambda_{pp}, \lambda_{pr}). \tag{4.2}$$

where p is the volume fraction, ε_s is the dielectric constant of the surrounding medium, f_j is the local field factor for j^{th} principle axis[31]. Because the change in dielectric constant is induced by the pump pulse and is sensed at probe wavelength, $\Delta\varepsilon_m^{'}$ should depend on both the pump and probe wavelengths and their polarizations with respect to the orientation of the particle. For sufficiently small absorbed pump energies, $\Delta\varepsilon_m^{'}$ depends linearly on absorbed power per unit volume of the particle[85]. For small particles, the contribution to the extinction cross-section is mainly dominated by absorption. Thus, $\Delta\varepsilon_m^{'}$ is expected to be directly proportional to the extinction cross-section of the particle.

The $|\Delta T/T|_{pk}$ of Ag NP colloid when probed at 550 nm is much lower (only 9%) than that when probed at 408 nm. When pumped at 400 nm, irrespective of the polarization, all the Ag NPs absorbs the light. The change in the temperature of free-electrons will be proportional to the C_{ext} of a single Ag NP. When probed at 408 nm, all the Ag NPs will contributes to the $|\Delta T/T|_{pk}$ and the contribution from $Im\left[f_j^2\right]$ is also strong near to the LSPR (Fig.4.12(a)). However, when probed at 550 nm which is far separated from LSPR, the contribution to $|\Delta T/T|_{pk}$ from $Im\left[f_j^2\right]$ reduces considerably, reducing the measured $|\Delta T/T|_{pk}$[85, 125, 126]. Because the pump fluence is the same in both of these cases, the decay time will also remain the same irrespective of the probe wavelength.

4.4 Random Orientation Model

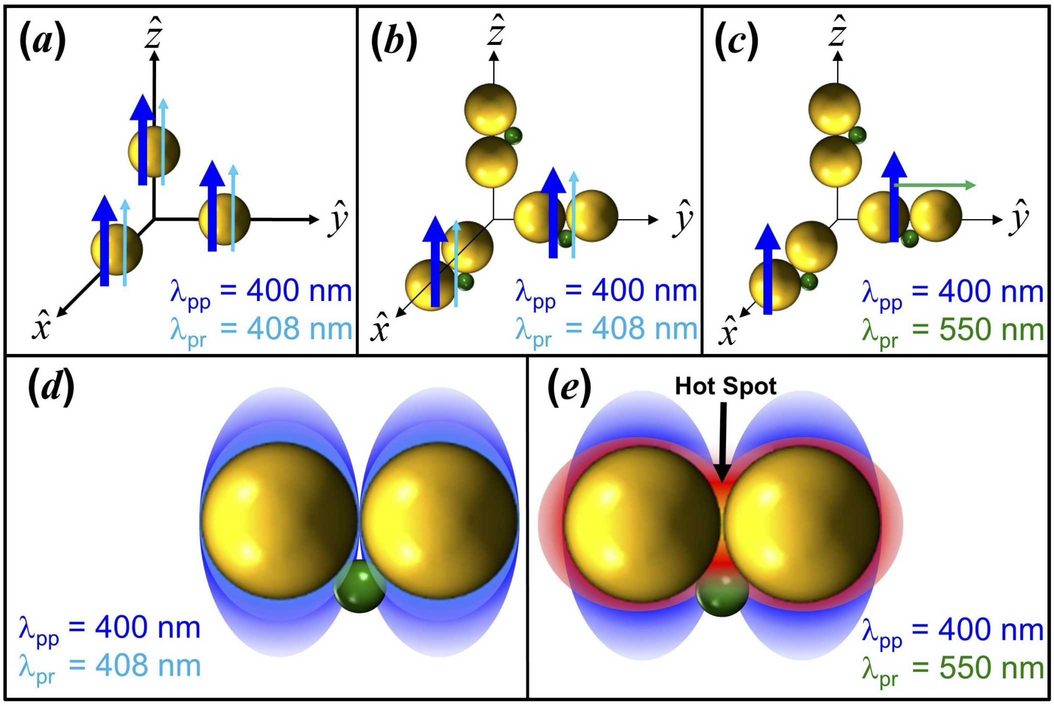

FIGURE 4.12: Schematic of particles oriented in three different directions along with polarization of pump and probe pulse. Blue thick line indicates polarization of pump pulse(400 nm) and thin line, blue(408 nm) and green(550 nm), indicates polarization of probe pulse.

The observed strengths of the LSPR peaks in the case of Ag\CdTe/Ag hybrid colloid can be explained by a simple model based on the orientation of the particles. Because of spherical symmetry, all the Ag NPs in the colloid absorbs the incident light irrespective of its polarization. Although in a colloidal sample all orientations of Ag\CdTe/Ag NP is possible, consider a more straight forward picture where all the particles are randomly aligned parallel to one of the three Cartesian directions with equal probability (inset of Fig.4.5). Such an assumption in the distribution of particles has been shown to match well with that of the measured optical response of colloid containing randomly oriented ellipsoids and nanoprisms[32, 113]. Let the electric field be aligned to one of the Cartesian directions such that about 66.7% ($\frac{2}{3}^{rd}$) of the particles will contribute to the T-LSPR peak (at 410 nm) because for these particles the polarization of light is oriented along the transverse axis. Whereas the rest 33.3% ($\frac{1}{3}^{rd}$) of the particles have their longitudinal axis aligned along the polarization and will show resonance at L-LSPR (535 nm) i.e. along the gap plasmon. The measured LSPR peak heights for Ag\CdTe/Ag hybrid colloid at 410 nm and 535 nm are 65% and 32% of that of Ag NP colloid at its LSPR peak which are very close to that predicted by the model. This also implies that the C_{ext} of an Ag\CdTe/Ag particle is exactly the same as that of two isolated Ag NPs if polarization is appropriately aligned. The random orientations of the particles mainly cause the reduction in C_{ext} of the Ag\CdTe/Ag hybrid colloid.

As discussed in the case of static optical response above, when the particle is aligned along the transverse axis, it's C_{ext} will remain nearly the same as that of two isolated Ag NPs. In Fig.4.12, schematic of particles oriented in three different directions along with the polarization of the pump and probe beams used in the experiments are shown. When excited at 400 nm, close to T-LSPR, nearly $\frac{2}{3}^{rd}$ of the Ag\CdTe/Ag hybrid particles will absorb the light, and the increase in temperature of free-electrons will also be nearly same as that of the isolated Ag NP for the same pump fluence. When probed at 408 nm, the factor $Im\left[f_j^2\right]$ (Eq.4.2) will also be finite and all the excited Ag\CdTe/Ag particles (which is only $\frac{2}{3}^{rd}$ of the total) will contribute to $|\Delta T/T|_{pk}$. Thus the $|\Delta T/T|_{pk}$ measured for Ag\CdTe/Ag hybrid colloid should be lesser by at least a factor of $\frac{2}{3}^{rd}$ compared to that of Ag NP colloid when probed at 408 nm. With a similar argument it can be shown that the $|\Delta T/T|_{pk}$ of Ag\CdTe/Ag hybrid colloid probed at 550 nm, close to L-LSPR, should be lesser by at least a factor of $\frac{1}{3}^{rd}$ compared to that of Ag NP colloid probed at 408 nm (Fig.4.12(c)). The $|\Delta T/T|_{pk}$ measured for the Ag\CdTe/Ag hybrid colloid is about $\sim$ 44% and 11% when probed at 408 nm and 550 nm, respectively, compared to that of Ag NP colloid at 408 nm. Thus, the measured $|\Delta T/T|_{pk}$ of Ag\CdTe/Ag hybrid colloid at these wavelengths was even lower than that estimated. For the metal nanoparticles, it is well known that the amount of energy absorbed by metal nanoparticle decides the $|\Delta T/T|_{pk}$. Based on above observation, the increase in temperature of free-electrons in the Ag NPs of Ag\CdTe/Ag hybrids should be same or lower than that of the particles in bare Ag NP colloid. Thus the electron-phonon relaxation time measured for Ag\CdTe/Ag hybrid colloid should have remained the same or reduced than that of Ag NP colloid, which is opposite to that of observed in the experiment. Hence, change in the absorbed power cannot explain the increase in the relaxation time measured for Ag\CdTe/Ag hybrid colloid.

4.5 Origin of Ultrafast Optical Response Ag\CdTe/Ag Hybrid Nanostructure

Prashant K. Jain *et al.* studied the transient change in the optical response of aggregated gold NPs when excited at 400 nm[127]. Their result shows that the electron-phonon relaxation time is shorter when probed at the longer-wavelength LSPR peak compared to that measured at the shorter wavelength. They attributed this reduction to the increased overlap of the longer wavelength LSPR with the phonon spectrum and the enhanced interfacial electron scattering[127]. A similar reduction in electron-phonon relaxation time has also been reported for other Au and Ag NP aggregates[128, 129]. This implies that the interaction between two metal NPs should lead to a reduction in the relaxation time of the $\Delta T/T$, which is again the opposite of what is observed in the present case. Thus, the presence of CdTe QD in between the Ag NPs is indeed playing a role in the dynamics observed in Ag\CdTe/Ag colloid.

When a metal NP is attached to a semiconductor, three main processes modifythe response of the combined superstructure. A direct metal-to-semiconductor interfacial charge transfer, which occurs through direct excitation of electron from metal NPs to empty states in semiconductor[130–132]. Such transfer is possible in hybrid systems where the semiconductor is in direct contact with the surface of the metal. In some hybrid cases, the metal NP absorbs the light creating hot-electrons, which then gets transferred to the empty levels in semiconductor. Signature of such hot-electron transfer from metal NP to semiconductor QD has been observed in several hybrid nanostructures[130, 131, 133]. Even if there is no direct contact between the metal and semiconductor, hot-carrier transport still occurs via the linking polymer/molecule[20]. In addition to the processes mentioned above, a direct energy transfer between metal and semiconductor is also possible, if the LSPR of metal NP overlaps with the absorption spectrum of semiconductor QD[93, 134].

Charge or energy transfer between the constituents of a hybrid strongly depends on the final superstructure formed by the metal-semiconductor nanostructures[20, 135]. When the Ag\CdTe/Ag hybrid colloid is pumped at 400 nm, T-LSPR is excited in the Ag NPs, and at the same time, it can also excite carriers in CdTe from valance band to conduction band. A comparison of temporal response of $\Delta T/T$ of Ag NP colloid and Ag\CdTe/Ag colloid when probed at 408 nm shows that the dynamics in this system is dominated by the plasmonic response of Ag NP. Even if carriers are excited in CdTe QDs, when probed well above the band edge, CdTe QDs do not show a significant change in its transient response[20]. Further, exciting at 400 nm, resonant with T-LSPR, does not create hot-spot between the Ag NPs where CdTe

QD is located since it does not excite gap plasmon (Fig.4.12(*d*)). Thus, probing the Ag\CdTe/Ag colloid at 408 nm strongly resembles the dynamics of Ag NP colloid (Fig.4.10). On the other hand, when probed at 550 nm, the probe pulse can sense the presence of CdTe QD because the probe field gets enhanced at the location of CdTe QD. Further, CdTe QD can also show a strong transient change in transmission when probed at 550 nm. Thus, although a significant contribution of metallic response is expected near to the gap plasmon, the Ag\CdTe/Ag hybrid colloid, when probed at 550 nm, shows a longer response time than that of bare Ag NP colloid.

4.6 Summary

When Ag NP colloid is mixed with TGA capped CdTe QD colloid such that in the mixed colloid the number ratio between the Ag NPs and CdTe QDs is 2:1, stable HNS with two Ag NPs and a CdTe could be formed. Optical spectra during growth and transient optical response suggests that the final structure has two touching Ag NPs with CdTe QD stuck in between them. The static optical response of the final hybrid colloid could be explained well by the electromagnetic interaction between these particles present in the structure. Assuming that the extinction cross-section of each Ag NP in the Ag\CdTe/Ag hybrid structure to be the same as that of an isolated Ag NP, the optical response of Ag\CdTe/Ag colloid could be explained by their random orientations in the host.When excited and probed near the T-LSPR, the ultrafast optical response of Ag\CdTe/Ag HNS resembles that of a bare Ag NP. On the other hand, when probing at the gap plasmon, a delayed recovery of transient transmission was observed. This is attributed to sensing the presence of CdTe QD in the hot-spot regime by the probe field tuned to the gap plasmon. Placing a semiconductor QD at or close to the hot-spot is a significant step towards using the enhanced local field in various applications such as plasmonic sensing, optoelectronics, energy harvesting, nanolithography and optical nano-antennas. A similar hybrid formation technique can be extended to other noble metals and II-VI SQDs capped with thiols. Therefore these studies are also crucial for the advancement in the area of colloidal self-assembly, with impacts on the dynamic properties of gap plasmon for specific needs[7, 136].

Chapter 5

Radiative and Non-radiative process in Ag nanosphere and CdTe quantum dot Hybrid Nanostructure

The ultrafast response of metal-semiconductor HNS can have both the plasmonic and excitonic contributions. These contributions have different physical origin and are usually described by different physical theories. In case of isolated MNPs, ultrafast optical response in explained by the increase in temperature of free electrons[85] while in isolated SQDs, both radiative and non-radiative processes contribute to the total carrier dynamics and is explained by band to band absorption, band filling, inter and intra band relaxation, etc[86]. Thus, the various dynamical processes that occurs in individual constituent materials of HNS as well as their synergistic interaction complicates the understanding of complete optical response of HNS. Nonetheless, it is important to comprehend the basic interactions between these individual constituents for designing an HNS focused toward a particular application. Mondal et al. has reported a detailed study on the ultrafast response of such Ag NP and CdTe QD HNS by exciting only the CdTe QDs and away from the LSPR of Ag NP in water[20]. Electron transport from CdTe QD to Ag NP could be revealed by their study. In this chapter[**], we study the origin of the optical response of Ag NP surrounded by CdTe QDs, namely Ag-nCdTe, under simultaneous excitation of plasmon and carriers in CdTe QD using ultrafast transient absorption, steady-state absorption and time-resolved photoluminescence spectroscopy. It was observed that the ultrafast optical response of the hybrid shows an initial (upto $<$ 3 ps) plasmonic response while the later times ($>$ 3 ps) shows CdTe QD response. Further, using steady-state and time-resolved photoluminescence, we also study the radiative property of this HNS. The emission from Ag-nCdTe is shown to be always quenching, irrespective of the excitation energy.

5.1 Ultrafast Optical Response of Ag-nCdTe Hybrid Nanostructure probed near LSPR

The individual colloidal solutions of Ag NPs and CdTe QDs dispersed in water were prepared and characterized separately(discussed in chapter 2). The volume fraction of CdTe QDs and Ag NPs in water in the individual colloids were of the order of 10^{-6} and 10^{-7}, respectively. Based on our study in Chapter 3, at the mixing ratio of γ = 0.56, each of the Ag NP is completely surrounded by 32 CdTe QDs (n=32) in the Ag-nCdTe hybrid[89]. Once these CdTe QDs surrounds the Ag NP surface, further attachment of CdTe QDs to the same Ag NP is prevented thus making a stable HNS in the mixed solution. Ideally, in the Ag-nCdTe HNS sample it is expected that there are only HNS with no individual particles.

Figure 5.1 shows the extinction spectra of Ag NP and CdTe QD colloids. The extinction spectrum of Ag NP colloid shows a well-known single LSPR peak at 413 nm, which is typical for small Ag spherical particles in water[31]. On the same

---

[**] This work is published by the author of this thesis as "Ultrafast Carrier Dynamics in Ag-CdTe Hybrid Nanostructure: Non-radiative and Radiative Relaxations”, **Sabina Gurung**, Durga Prasad Khatua, Asha Singh, J Jayabalan, Journal of Physics: Condensed Matter, **2021** 33 (18), 185702.

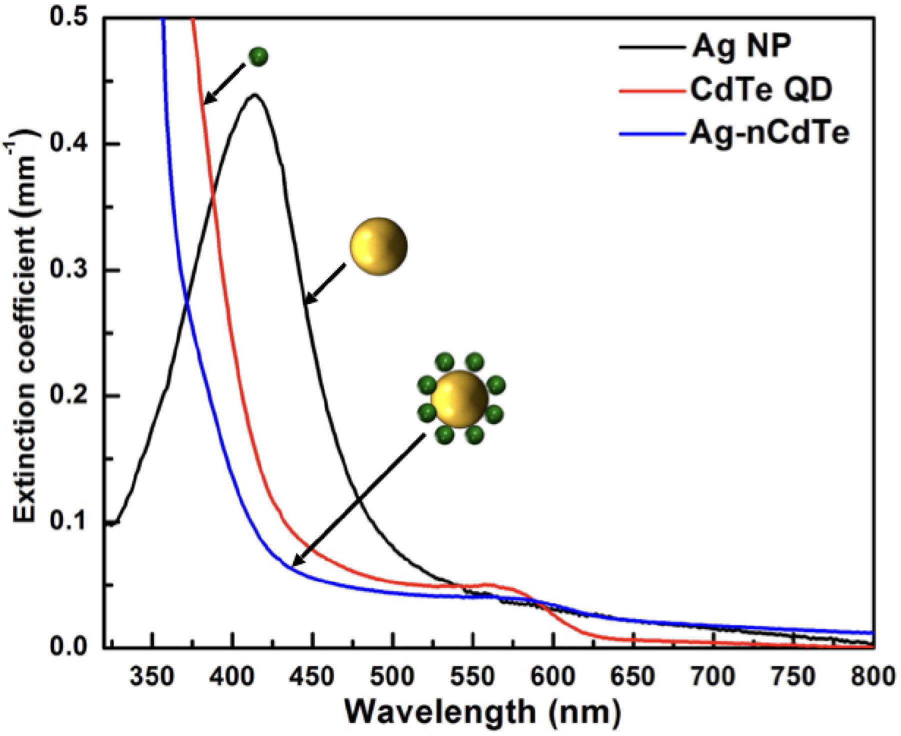

FIGURE 5.1: Extinction spectra of the colloidal solutions of Ag NP, CdTe QD and Ag-nCdTe hybrid.

figure, the extinction spectrum of CdTe QD colloid is also shown. The lowest energy excitonic peak of CdTe QD colloid, the 1s-1s transition is at 560 nm. Figure 5.1 also shows the measured extinction spectrum of Ag-nCdTe hybrid colloids and is different from that of both of its constituent colloids[89]. Unlike the Ag\CdTe/Ag case, the present sample, Ag-nCdTe hybrid, has an increasing absorption strength towards UV regime similar to that of a bare CdTe QD colloid. Additionally, the Ag-nCdTe hybrid has an increased absorption in the longer wavelength regime (starting from $\sim$ 600 nm). Further, the excitonic peak in case of Ag-nCdTe colloid got bleached compared to the bare CdTe QD colloid. Various groups have reported similar changes in the extinction spectrum in metal-semiconductor HNS when compared to that of individuals[1, 11, 75, 137, 138]. The increase in the absorption cross-section in the longer wavelength of Ag-nCdTe is attributed to the defect states created by the attachment of Ag NP to CdTe QD. On the other hand, the presence of

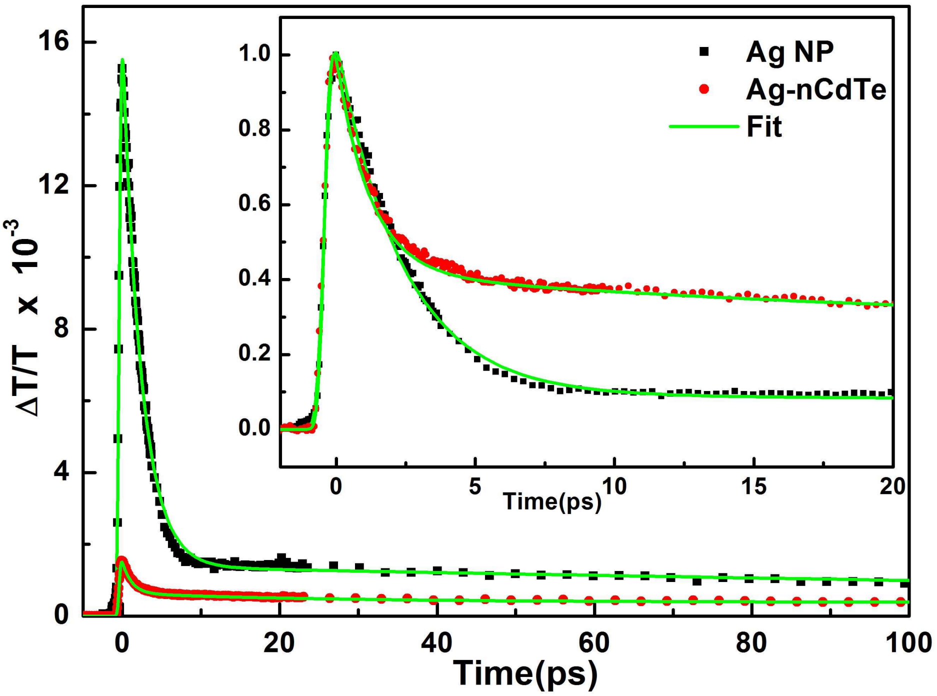

FIGURE 5.2: Transient transmission of Ag NPs and Ag-nCdTe colloidal samples when excited at 400 nm and probe at 408 nm. Inset shows the normalized curve of the same data.

MNP also dissociates the excitons in the semiconductor QD resulting in the reduction of exciton peak strength.

Figure 5.2 shows the transient transmission ($\Delta T/T$) measured for the colloidal samples of bare Ag NP and Ag-nCdTe hybrid colloid when probed at 408 nm. Both Ag NP and Ag-nCdTe hybrid colloids showed measurable change in the transmission of the sample at intensity used in the measurement. The magnitude of $\Delta T/T$ in both the colloids starts increasing with the arrival of the pump pulse, reaching a maximum by about 450 fs. At later time delay, $\Delta T/T$ reduces, leaving a residue even up to 100 ps. However, the peak of $\Delta T/T$ of Ag-nCdTe colloid when probed at 408 nm is only 10% of that of Ag NP colloid. Further, the reduction in the amplitude of fast component is much higher than that of the longer decay component. This difference in the reduction in the magnitudes can be clearly seen in the normalized plot of the $\Delta T/T$ (inset of Fig.5.2). Relatively, the long decay time component is much more in the case of Ag-nCdTe hybrid compared to that of bare Ag NP colloid. Since the extinction in Ag-nCdTe HNS (Fig.5.1) is strongly QD dominated, it is essential to isolate the contribution of bare CdTe QDs (the non-interacting volume of CdTe) to understand the contribution of metal and interaction between metal and semiconductor in hybrid. This will allow an easy interpretation of data with respect to that originating from interaction between metal and semiconductor. Therefore we used low concentration of CdTe QD such that for the number density of CdTe QD same as that in the Ag-nCdTe hybrid, CdTe QD colloid did not show any measurable $\Delta T/T$ signal. Thus, the finite $\Delta T/T$ measured for the Ag-nCdTe hybrid should be attributed to the contribution by the Ag NP and the synergistic interaction between Ag NP and CdTe QDs. The origin of transient transmission signal from Ag NP colloid has already been discussed in earlier Chapter 4(sec 4.3).

Let us now look at the origin of the ultrafast optical response of the Ag-nCdTe hybrid colloid. In a metal-semiconductor hybrid, when a MNP interacts with SQD, the optical response of the combined nanostructure is expected to be very different from that of the individual components. When excited at the LSPR, the LFE occur near the MNP which can be much higher than the applied; such a large enhanced field can increase the absorption in SQD[72, 139]. It is also possible that excited carriers may get transported from MNP to SQD or vice versa. Additionally, energy exchange processes like foester resonance energy transfer (FRET) and plasmon-induced resonance energy transfer (PIRET) are also possible in the hybrid system[19, 90]. Coupling between the MNP and SQD is also known to introduce additional defect states in the HNS[1, 11]. The individual contribution from each of these above mentioned processes to the optical response of the hybrid depends on the shape, size and material of the individual components, the properties of linking molecules and their spatial distribution. Since the temporal response of the Ag NP and Ag-nCdTe hybrid colloids are nearly similar and the bare Ag NP gave a strong transient signal at this wavelength (Fig.5.2), it is essential to understand the contribution of plasmonic response from Ag NP in the Ag-nCdTe HNS.

5.2 Effect of CdTe QD on the LSPR of a Ag NP

It is well known that the LSPR response of a metal NP depends strongly on the dielectric constant of the surrounding medium. To understand the effect of the presence of CdTe QD on the optical response of Ag NP, we have calculated the optical response of the combined HNS using the T-matrix technique. In the T-matrix calculations, we used the experimentally measured sizes of the Ag NP and CdTe QD. Figure. 5.3 shows the calculated extinction cross-section of a Ag NP surrounded by 32 CdTe QDs using T-matrix technique. For comparison, we have also shown the calculated extinction spectra of a single Ag NP in water and 32 non-interacting CdTe QDs. As expected, the optical response of Ag-nCdTe colloid is quite different with a strong red-shifted LSPR peak of about 75 nm compared to that of Ag NP colloid. Further, the peak strength of LSPR peak for Ag NP also reduces to about 65% of that of Ag NP. Thus, an excitation at 400 nm would only weakly excite the LSPR in case of Ag-nCdTe hybrid. It should be noted that the optical response calculated using the T-matrix technique considers only electromagnetic interaction between the Ag NP and CdTe QD. However, in a real metal-semiconductor hybrid, there is not only electromagnetic interaction but several other charge and energy exchange processes mentioned earlier. Thus, a calculation which assumes only the electromagnetic interaction between the metal and semiconductor would not mimic the true properties of the hybrid. Nevertheless, such calculation would give some insight into the contribution from electromagnetic interaction to the final optical response of the HNS.

It is well established that the peak change in $\Delta T/T$ directly depends on the amount of energy absorbed by the metal NP[85]. Any change in the amount of absorbed energy in presence of CdTe QDs should change the transient response of Ag NP in Ag-nCdTe hybrid. A comparison between the calculated extinction spectra of Ag NP and Ag-nCdTe hybrid can give an idea about the change in the absorbed energy when excited at 400 nm. The numerically calculated LSPR peak of Ag NP in water is at 393 nm while in the experiment, it is at 413 nm. Taking into account of

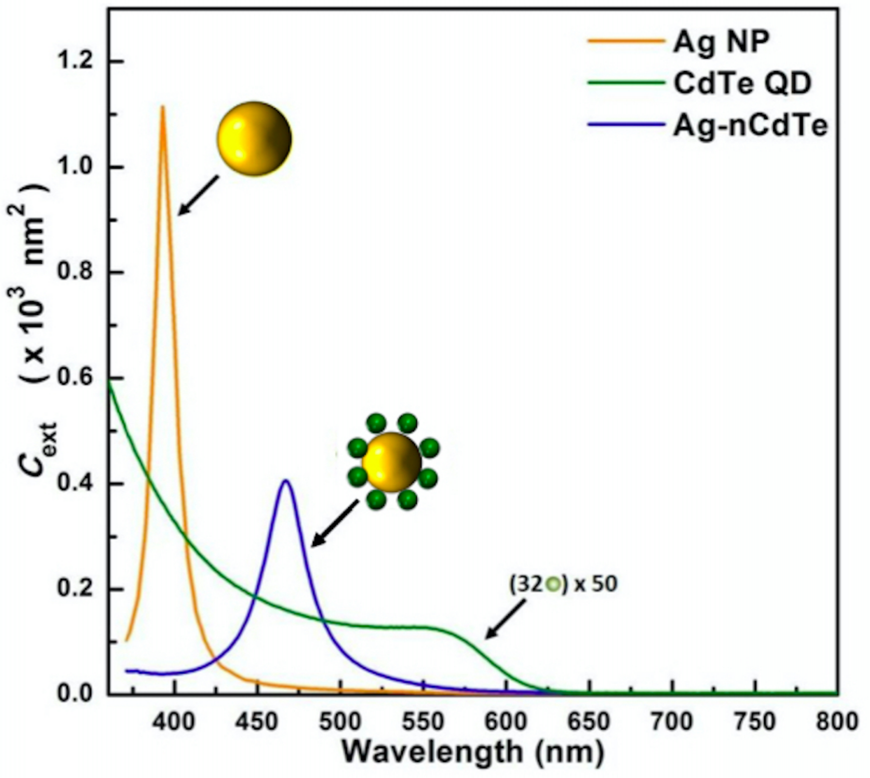

FIGURE 5.3: The extinction cross-section calculated using T-Matrix technique for a single Ag NP in water (orange), 32 non-interacting CdTe QDs and the Ag-nCdTe HNS (1 Ag surrounded in all directions by 32 CdTe QDs).

such shift, the absorption in Ag NP in the hybrid should be only 4% of that of bare Ag NP at 400 nm. The measured peak change in $\Delta T/T$ of Ag-nCdTe hybrid colloid is about 10% of that of Ag NP colloid (Fig.5.2). Further, an exponential decay fit to the measured $\Delta T/T$ in case of Ag-nCdTe gives 1.3 ps while it is 2.3 ps in case Ag NP colloid. The electron-phonon (e-ph) thermalization time depends on the absorbed energy in Ag NP. Thus, a reduction in absorbed energy should also reduce the decay time of $\Delta T/T$ as observed in the case of Ag-nCdTe hybrid. Therefore, it looks tempting to attribute the observed changes in $\Delta T/T$ to the reduction in absorbed energy in Ag NP when surrounded by CdTe QDs in the hybrid colloid.

5.3 Understanding Dynamics of Ag-nCdTe Hybrid Nanostructure using Two-Temperature Model

If the observed changes in $\Delta T/T$ is only due to such reduction in absorption as predicted by electromagnetic theory, the measured dynamics in Ag-nCdTe colloid can be explained using a two-temperature model (TTM), which works well for pure Ag NP colloid[85, 123, 124]. Under low excitation conditions, change in dielectric constant of Ag NP is proportional to the temperature of the electrons[85]. The relation between the electron temperature (T_e) and lattice temperature (T_l) in TTM is given by following differential equations:

$$\begin{aligned} \frac{\partial T_e}{\partial t} &= -\frac{g}{C_e}\left(T_e - T_l\right) + \frac{Q(t)}{C_e}, \qquad (5.1) \\ \frac{\partial T_l}{\partial t} &= \frac{g}{C_1}\left(T_e - T_l\right), \qquad (5.2) \end{aligned}$$

where, g represents e-ph coupling constant, $Q(t)$ is the absorbed power density, which is proportional to the pump intensity and C_e (=γT_e) and C_l is the specific heat capacities of the free electrons and lattice respectively. Using the typical values reported for g, C_l, and γ the Eq.5.1 and Eq.5.2 were solved numerically to obtain the time dependence of T_e. This estimated T_e multiplied with a proportionality constant C was then fit to the decay part of the measured $\Delta T/T$ with Q and C as fitting parameters. Figure. 5.4 shows the best fit obtained for the decay part of the measured $\Delta T/T$ of Ag NP colloid. To fit the $\Delta T/T$ of Ag-nCdTe colloid, we keep all the parameters same as that used in the fitting of Ag NP colloid including the constant C and reduce only $Q(t)$ until the peak $\Delta T/T$ matches that of the Ag-nCdTe colloid. The transient curve thus obtained is also shown in Fig.5.4. Clearly, for the corresponding peak change, the fast decay time should have been much smaller than that observed in the experiment. Further, the magnitude of the long decay component for Ag-nCdTe should also be much lower than that observed in the experiment

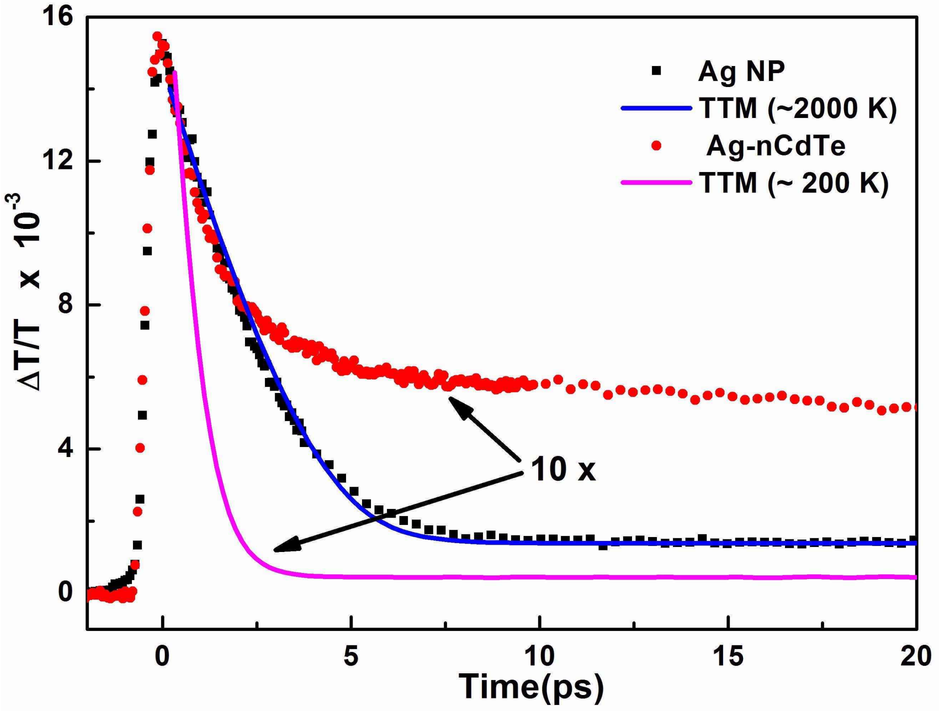

FIGURE 5.4: The TTM fit to the experimental $\Delta T/T$ measured for Ag NP colloid and Ag-nCdTe colloid. The data for Ag-nCdTe is increased by 10 times to make it comparable with the Ag NP.

(inset of Fig.5.2). Thus, although the transient response of Ag NP and Ag-nCdTe HNS looks similar, from the comparison with TTM it is clear that the measured transient signal in Ag-nCdTe HNS could not be just attributed to the weak plasmonic response from Ag NP. This suggests that other coupling mechanism between Ag NP and CdTe QDs like charge transfer is also playing a significant role in dictating the final optical response of Ag-nCdTe hybrid.

Several groups have measured the optical response of pure CdTe QDs [20, 140, 141]. When CdTe QD colloid is pumped at 400 nm and probed on the red-side close to 400 nm, it shows a small increase in transmission (positive $\Delta T/T$). This increase in the transmission is attributed to the band-filling effect when carriers are excited into the conduction band of CdTe QD from its valance band [86, 140]. Note that the bare CdTe QD colloid having same number density as that of Ag-nCdTe hybrid colloid, did not show any measurable signal. Nonetheless, an increased absorption in CdTe QD in presence of Ag NP near to it can contribute to the increased signal.

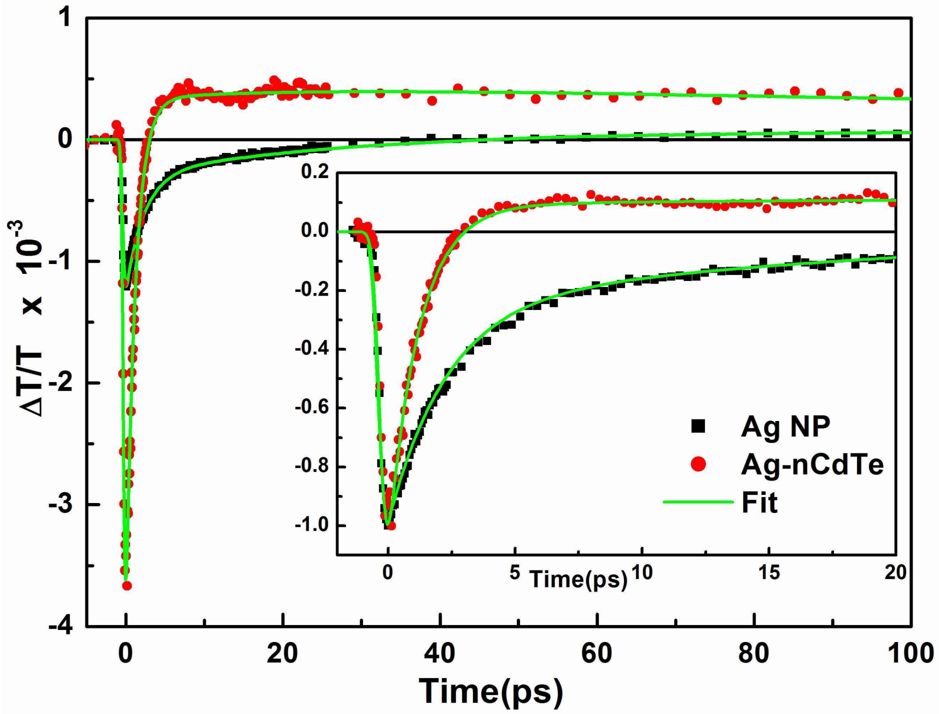

FIGURE 5.5: Transient transmission of Ag NPs and Ag-nCdTe colloidal samples when excited at 400 nm and probe at 550 nm. Inset shows the normalized curve of the same data.

Further, hot carriers from Ag NP can also get transported to CdTe QD in femtosecond time scale which can further increasing the transient response of CdTe QD in Ag-nCdTe hybrid. Thus, we attribute the transient response of Ag-nCdTe hybrid to that originate from two different processes, one that arising from the weak plasmonic response of Ag NP and an increased CdTe QD response in presence of Ag NP. Since both of these processes contributes positively to the measured $\Delta T/T$, it is difficult to distinguish between these two contributions.

When excited at 400 nm and probed close to the exciton peak ($\sim$ 550 nm), the CdTe QD colloid show a much larger positive $\Delta T/T$ signal when compared to that of probing near 400 nm[20, 140, 141]. On the other hand, the Ag NP will show a weak negative $\Delta T/T$ since it is away from LSPR and on the red side of the LSPR peak. Thus, unlike 408 nm probing, a measurement at 550 nm should show opposite contribution for Ag NP and CdTe QD response enableing us to isolate the origin from these two different contributions.

5.4 Ultrafast Optical Response of Ag-nCdTe Hybrid Nanostructure probed near Exciton

Figure.5.5 shows the transient transmission signal measured for the colloidal samples of bare Ag NP and Ag-nCdTe hybrid colloid when probed at 550 nm. The transmission of both the samples reduces with the arrival of the pump pulse ($\Delta T/T$ is negative). Once again a maximum of $|\Delta T/T|$ occurs by about 450 fs after the arrival of the pump pulse. Both the negative $\Delta T/T$ and the delayed maximum are the signature of plasmonic contribution from Ag NP. In the next few tens of picoseconds, the $\Delta T/T$ of Ag NP colloid recovers with a time constant of 2.4 ps which is nearly same as that of e-ph thermalization time observed at 408 nm probing. On the other hand, in case of Ag-nCdTe colloid, the $\Delta T/T$ changes sign near about 3 ps, becoming positive at later times. This positive signal is the signature of the band filling effect in CdTe QDs which remains more or less constant up to 100 ps[20, 140, 141]. The negative contribution of plasmonic response of Ag NP to the $\Delta T/T$ of Ag-nCdTe recovers within few picoseconds and is much faster than the positive contribution of CdTe QD. Thus, the negative plasmonic response of Ag-nCdTe HNS changes sign and becomes positive at delays more than 3 ps in Fig.5.5. To estimate the time constants the measured $\Delta T/T$ of Ag-nCdTe colloid at 550 nm was fit to the equation:

$$F(t) = \frac{1}{2}\mathcal{E}\left(t/\tau_r\right)\left[-Ae^{t/\tau_1} + B\left(1 - e^{t/\tau_1}\right) + C\right], \tag{5.3}$$

where, $\mathcal{E}$ is the error function. The first decay term corresponds to the plasmonic response of Ag NP and has a negative amplitude while the second term can be attributed to the positive contribution of band filling effect in CdTe QDs. We find that Eq.5.3 fits well to the measured $\Delta T/T$ with a time constant τ_1 = 1.3 ps. This time constant is same as that of the decay constant of Ag-nCdTe hybrid when probed at 408 nm. Thus, a model with enhanced absorption in CdTe QDs along with hot-carrier dynamics in Ag NP can explain the observed changes in the measured transient $\Delta T/T$ at these probe wavelengths. In the present case, where both Ag NP as well as CdTe QD are excited simultaneously, the transient signal has contribution from both of these different materials. Thus, the T-matrix calculation together with TTM showed that only part of the transient signal could be attributed to plasmonic response of Ag-nCdTe hybrid and rest has to be attributed to the synergistic interactions between Ag NP and CdTe QDs. The results obtained by probing at 550 nm confirms such observation. As mentioned before, the bare CdTe QD colloid could not give any measurable signal. However, in presence of Ag NP the Ag-nCdTe HNS colloid shows signature of transient response of CdTe QD. This indicates that the contribution from CdTe QDs is enhanced when coupled with Ag NP via electromagnetic interaction and hot carrier transport.

5.5 Emission Properties of Ag-nCdTe Hybrid Nanostructure

Now, let us look at the effect of presence of Ag NP on the photoluminescence (PL) properties of the CdTe QDs. Figure 5.6(*a*) and (*b*) shows the measured PL spectra of the bare CdTe QD and Ag-nCdTe colloids when excited at 405 nm and 550 nm, respectively. The PL spectra of both bare CdTe QD and Ag-nCdTe colloids are nearly Gaussian for both the excitation wavelength with a long tail on the higher wavelength side. It is observed that in Ag-nCdTe colloid, the PL peak intensity got quenched when compared to CdTe QD colloid, irrespective of the excitation wavelength. In the case of 550 nm wavelength photon excitation, the quenching is slightly less than when excited at 405 nm. Another notable observation is that, in Ag-nCdTe, the tail on the higher wavelength side got enhanced making the PL spectra more asymmetric. It is because when a hybrid is formed by ligand exchange, the

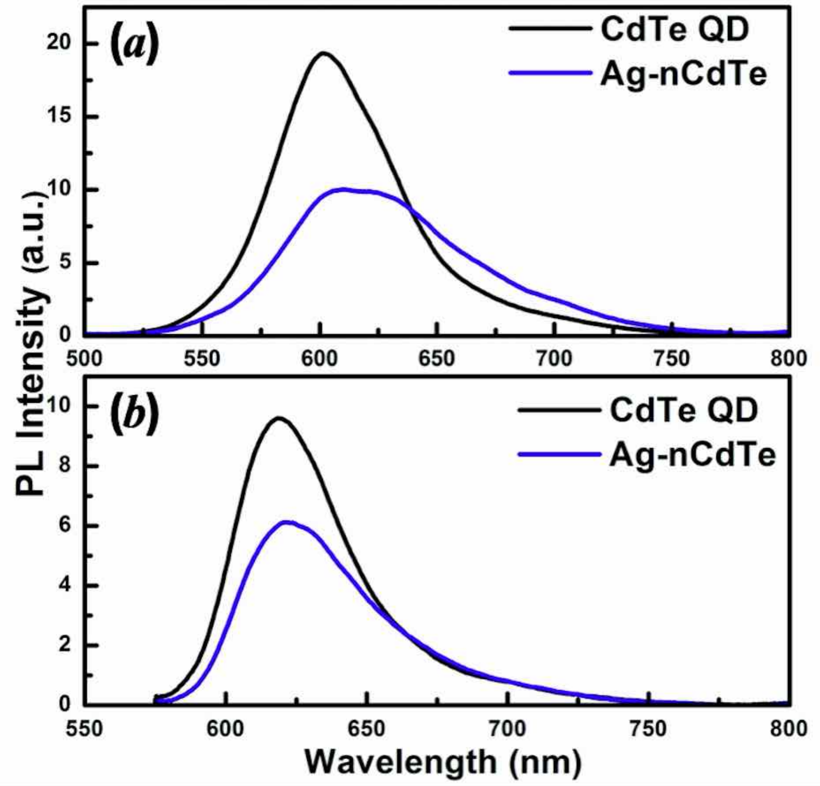

FIGURE 5.6: Photoluminescence spectra of CdTe QD and Ag-nCdTe colloids when excited at (*a*) 405 nm and (*b*) 550 nm.

MNP introduces additional defect states in the CdTe QDs. The band tailing at the higher wavelength is more enhanced when excited at 405 nm compared to 550 nm.

Figure 5.7 and Figure 5.8 shows that the temporal evolution of the PL of CdTe QD colloid when excited at 405 nm and 550 nm, respectively along with the measured IRF. With the arrival of the excitation pulse, the PL emission starts and over the next few tens of ns the PL decays at different rates. Depending on the number of processes that control PL emission, the II-VI semiconductor QD colloid shows a bi- or tri-exponential decay of the PL [110, 142–144]. We find that the temporal evolution of PL measured for CdTe QD colloid when excited at both the photon energies fits well to a tri-exponential decay function convoluted ($\otimes$) with the experimental IRF (I_{IRF}), given by

$$F(t) = \left(I_{IRF} \otimes \sum_{i=1,2,3} A_i e^{\frac{-t}{\tau_i}} \right) \tag{5.4}$$

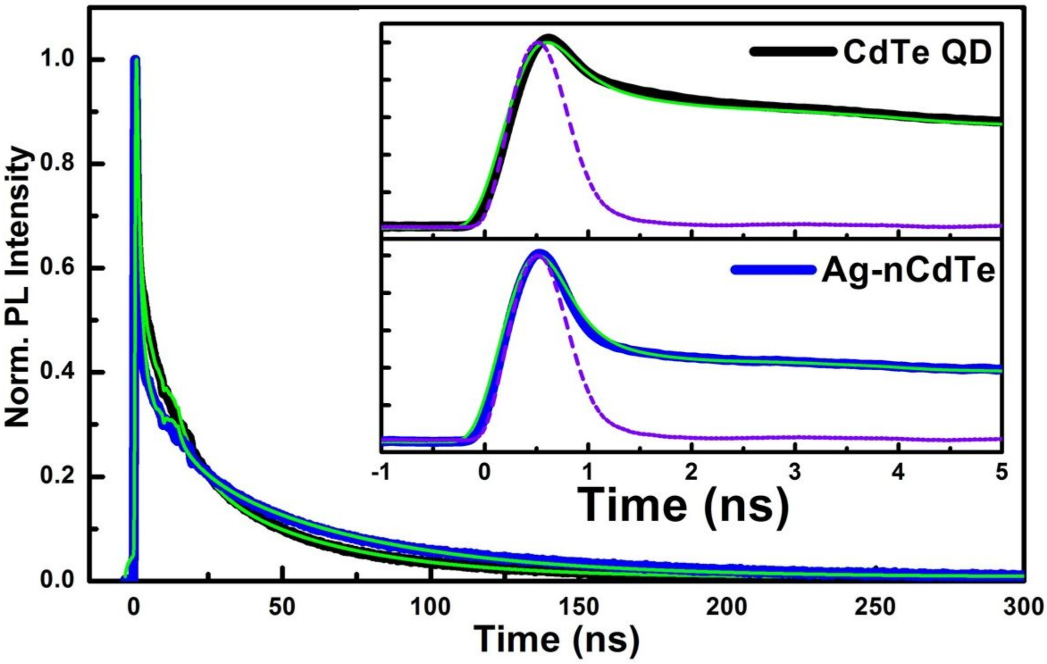

FIGURE 5.7: Time-resolved PL decay kinetics of CdTe QD and Ag-nCdTe colloids when excited at 405 nm. Inset shows the same time-resolved PL zoomed in time. The dotted line shows the measured IRF. The solid lines are the best fit to the corresponding data using Eq.5.4.

TABLE 5.1: Best fit parameters obtained by fitting Eq.5.4 to the experimental time-resolved PL of CdTe QDs and Ag-nCdTe colloid.

Sample	λ_{exc} (nm)	A_1 %	τ_1(ns)	A_2%	τ_2(ns)	A_3 %	τ_3 (ns)
CdTe QD	405	77	0.23± 0.02	14	7± 0.2	9	65± 2
	550	72	0.23± 0.01	17	7± 0.1	11	63± 2
Ag-nCdTe	405	87	0.21± 0.002	7	6.5± 0.2	6	235± 6
	550	87	0.19± 0.003	7	6± 0.2	6	150± 4

where A_i is the i^{th} signal amplitude corresponding to the time constant (decay time) τ_i. The best fit parameters obtained by fitting Eq.5.4 to the experimental CdTe QD PL is summarized in Table-5.1 and the best fit curves are shown in Fig.5.7 and Fig.5.8.

At excitation photon wavelength 405 nm, a strong portion of the PL, 77%, decays with a time constant of 0.23 ns, 14% decays with a time constant of 7 ns, and about 9% of the PL decays with a much longer lifetime of $\sim$ 65 ns. The best-fit parameters (decay times and amplitudes) for the bare CdTe QDs at 550 nm also remain almost similar to that of 405 nm excitation. This similarity indicates that the PL relaxation processes do not depend on the excitation photon energy. A similar observation was

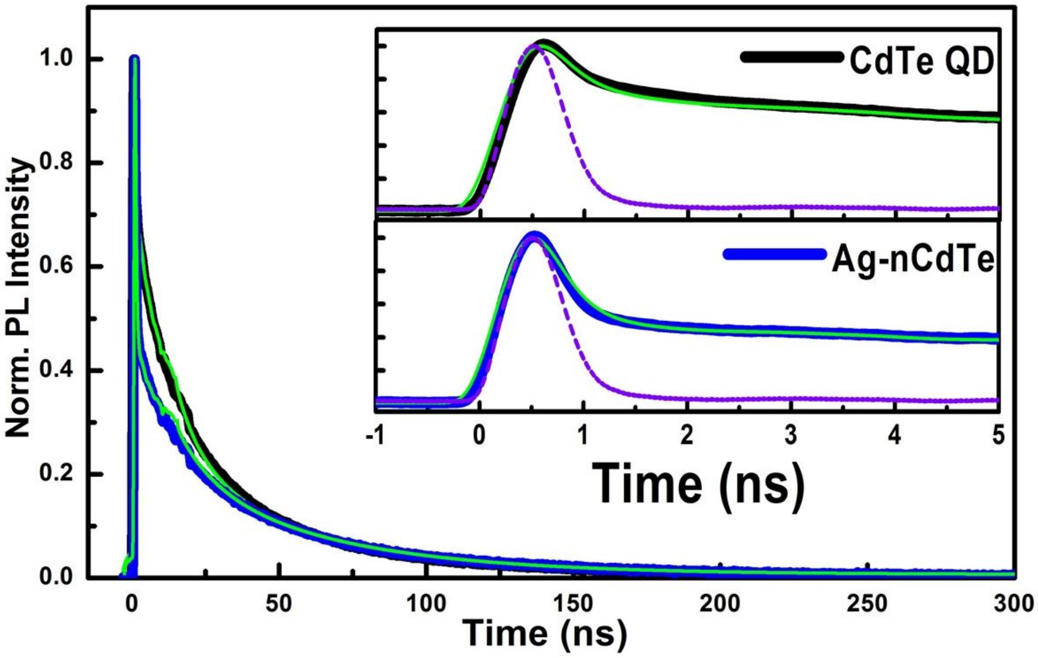

FIGURE 5.8: Time-resolved PL decay kinetics CdTe QD and Ag-nCdTe colloids when excited at 550 nm. Inset shows the same time-resolved PL zoomed in time. The dotted line shows the measured IRF. The solid lines are the best fit to the corresponding data using Eq.5.4.

also reported by Dey *et al.* and can be explained by the anti-bunching nature of the photons emitted from single QD [145]. Figure 5.7 also shows the time dependence of the PL measured for the hybrid sample, Ag-nCdTe, when excited at 405 nm. The PL measured for this case also fits well with the tri-exponential decay function given by Eq.5.4 (Table-5.1). In case of Ag-nCdTe, the three different time constant, τ_1, τ_2 and τ_3 turns out to be 0.21 ns, 7 ns and 150 ns, respectively. The τ_1 and τ_2 of Ag-nCdTe remained same compared to that of the bare CdTe QD, while the τ_3 became longer. The amplitude of each decay component, A_i's, has also changed compared to the bare CdTe QD colloid (shown in Fig.5.9). The amplitude of the fast lifetime component (A_1) has increased slightly while the other two amplitudes, A_2 and A_3, have reduced. The amplitude and the lifetime showed only small change when excited by photon corresponding to 550 nm wavelength. Lastly, it has been observed from Fig.5.10 that PL decay kinetics of CdTe QD and Ag-nCdTe remains same for both the excitation wavelength. This kind of excitation dependent PL is in agreement with

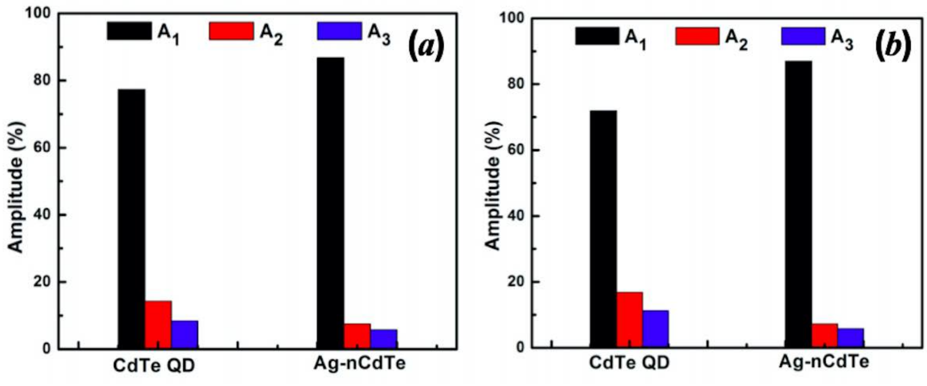

FIGURE 5.9: The amplitudes of the best fit parameters obtained by fitting Eq.5.4 to the experimental data of CdTe QD and Ag-nCdTe colloid when excited at (*a*) 405 nm and (*b*) 550 nm

Kasha's rule which states that PL should be independent of the excitation photon energy.

Several groups have studied the origin of PL and the decay process in bare CdTe QDs [110, 142, 144]. When the QD is illuminated by a light pulse having photon energy above the bandgap, carriers are excited in the QD such that electrons and holes are excited to the conduction and valence bands respectively. In the present case, the 1s-1s exciton transition wavelength is about 560 nm (Fig.5.1). When illuminated by photons corresponding to 405 nm wavelength, electrons and holes are excited deep into the conduction band and valence band, respectively. In the next few hundreds of femtoseconds, these electrons and holes relax non-radiatively to the corresponding band edge to finally form excitons. These excitons relax by the emission of photons. Such radiative recombination takes place over a period of several nanoseconds in similar QDs [1–3]. During this radiative recombination, a part of the carriers may relax to defect states present in the sample. Such transfer of carriers from the band edge to the defect state will reduce the excitonic emission. If the carrier transfer rate to the defect state is lower than the radiative recombination lifetime, the PL kinetics will also show the signature of this relaxation. A fast decay time in the order of 0.1 ns to 1.5 ns has been observed in CdTe QD and has been attributed to fast non-radiative recombination[144, 146]. The excitation intensity used

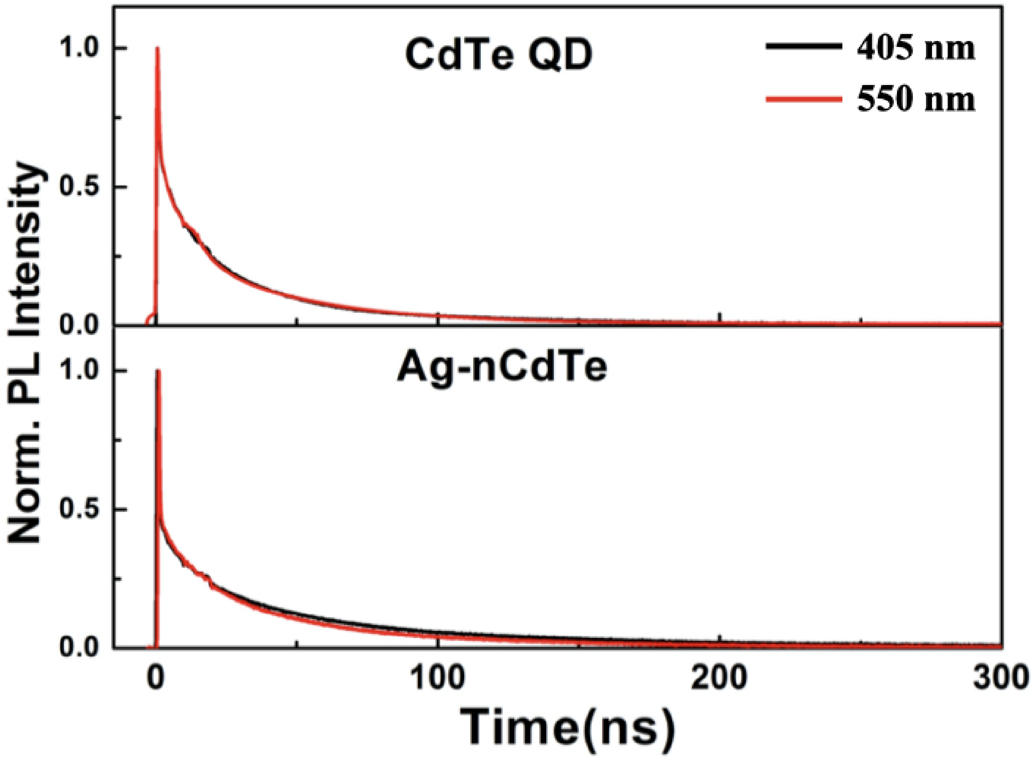

FIGURE 5.10: Comparison of time-resolved PL decay kinetics of CdTe QD and Ag-nCdTe colloids when excited at 405 nm and 550 nm.

to excite the sample in this work corresponds to the order of 10^{13} photon per cm^{-2}. At this excitation intensity Auger mechanism has been observed in CdTe and CdS QDs [146–148]. Therefore, in the present case, we attribute the shortest relaxation time observed, τ_1, in the case of CdTe QD colloid to the Auger like recombination. The process responsible for the decay times, τ_2 and τ_3, are attributed to the radiative electron-hole recombination and trap-state emission respectively[143, 144, 149]. In case of hybrid, increase in A_1 with a simultaneous reduction in A_2 and A_3, at 405 nm is due to the weak excitation of LSPR that increases the carrier density in CdTe QD and thus leads to increase in Auger recombination. As a result, the amplitude of radiative recombination reduces. When excited at 550 nm, although LSPR is not excited, but the hot electron transport reduces A_2 and A_3, resulting in fast quenching of PL,. Therefore the total integrated area under the PL spectrum quenches to nearly 70% for both 405 nm and 550 nm excitation compared to that of corresponding CdTe

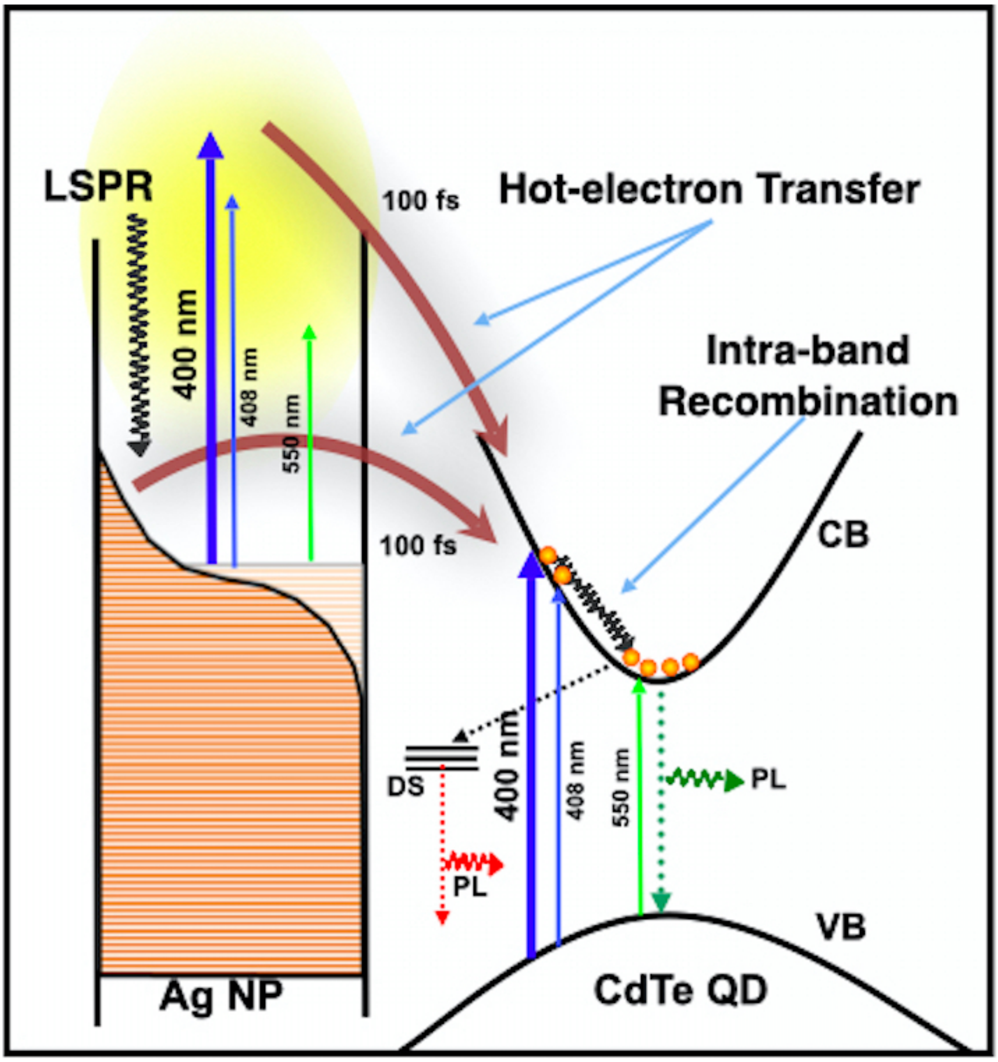

FIGURE 5.11: Schematic illustration of radiative and non-radiative relaxation in Ag-nCdTe HNS.

QD colloid. A schematic of the excitation and both radiative and non-radiative relaxation in the Ag-nCdTe HNS is shown in Fig.5.11.

5.6 Summary

Hybrid formation between a metal and semiconductor is shown to significantly alter the static optical responses like absorption and PL spectra. We find that both non-radiative and radiative components of the individual entities also gets significantly altered when Ag NP and CdTe QD are brought in close contact. Transient transmission measurements performed by exciting at 400 nm and probing at two different wavelengths shows that the contribution of CdTe QD to the transient response got increased in presence of Ag NP. However, the PL and time-resolved PL measurements did not result in increasing of the radiative emission from the CdTe QDs. The hot electron transport resulted in PL quenching in hybrid in comparison to CdTe QD irrespective of the excitation energy. This work provides significant insight into the various relaxation processes that leads to the charge transport and PL quenching mechanisms in metal-semiconductor hybrids.

Chapter 6

Quantifying Charge Transport between Ag nanoplate and CdTe quantum dot in a Hybrid Nanostructure

Metal-semiconductor HNS can be made to make use of advantages in both individual materials for device applications[12, 24–30]. A metal nanoparticle can directly increase the absorption efficiency of an adjacent semiconductor or it can absorb light and inject carriers into the semiconductor there by increasing light-matter interaction in semiconductor. However, for designing such hybrid material targeted towards a specific application, it is essential to understand the possible interactions between the individual constituents. In this chapter**, using an appropriate AgPT-nCdTe HNS (Ag nanoplate surrounded by CdTe QD), such that the LSPR of Ag nanoplate (PT) is well below the bandgap of CdTe QDs, we develop a formalism to get a fair estimate of the number of electrons getting transported from the Ag NP to the CdTe QD. We also study the PL spectrum and time-resolved PL to understand the emission property of AgPT-nCdTe HNS.

This work is published by the author of this thesis as "Counting the Electrons Hopping in Ultrafast Time Scales in an Ag–CdTe Hybrid Nanostructure", Asha Singh, **Sabina Gurung, Rama Chari, J. Jayabalan, The Journal of Physical Chemistry, **2019**, 123(47), 28584-28592.

6.1 Theory of Transient Optical Response of Metal Nanocolloids

Consider a composite medium composed of aligned noninteracting ellipsoidal metal particles, having homogeneous and isotropic dielectric constant ε_m, dispersed in a transparent host medium of dielectric constant ε_s. When the dimensions of the particle are much smaller than the wavelength of light, the effective dielectric constant of the colloidal medium (ε_{cm}) for each of its principle semi-axis, j (= 1, 2, 3), is given by,[31, 150]

$$\varepsilon_{cm,j} = \varepsilon_s + \frac{p}{3} f_j \left(\varepsilon_m - \varepsilon_s\right), \tag{6.1}$$

where p is the fraction of volume occupied by the particles in colloid. The function, f_j, also known as the field enhancement factor, is given by,

$$f_j = \frac{a_j \varepsilon_s}{\varepsilon_m + b_j \varepsilon_s}, \tag{6.2}$$

with $a_j = 1/L_j$ and $b_j = (1 - L_j)/L_j$. Here L_j's are the shape dependent depolarization factors for the ellipsoidal particles [31, 150]. The absorption coefficient of the colloid is related to the imaginary part of dielectric constant of colloidal medium and is given by,[151]

$$\alpha(\lambda) = \frac{2\pi}{\lambda\sqrt{\varepsilon_s}} Im\{\varepsilon_{cm}\}, \tag{6.3}$$

where λ is the wavelength of light and c is velocity of light. The dielectric constant of a metal (ε_m) is complex, $\varepsilon_m = \varepsilon_m^{'} + i\varepsilon_m^{''}$, and for noble metals $\varepsilon_m^{'}$ can be negative in visible regime. Due to the dispersion of ε_m, it is possible that at certain wavelengths the condition,

$$b_j = -\frac{\varepsilon_m^{'}(\lambda)}{\varepsilon_s(\lambda)}, \tag{6.4}$$

is satisfied. A resonance occurs at these wavelengths in $\alpha(\lambda)$, which are known as localized surface plasmon resonances[31, 32]. For a sphere, all L_j's are same and equal to 1/3. Hence a metal nanosphere colloid show a single LSPR peak[31, 32]. However, in general, for an ellipsoidal particle where all the three principle semi-axes are different, the corresponding colloid can show three distinct LSPR peaks depending on the orientation of particle with respect to the direction of applied electric field[31, 150]. Using Eq.6.1 the absorption coefficient can be rewritten as

$$\alpha(\lambda) = -\frac{2\pi p\sqrt{\varepsilon_s}}{3\lambda} a_j Im\left[f_j(\lambda)\right]. \tag{6.5}$$

It is straight forward to extend this calculation for a colloid containing randomly oriented ellipsoidal particles[150]. This can be done by integrating the contributions from all possible orientations of the particle with respect to the applied field. When a metal nanocolloid is excited by a short pulse of wavelength close to any of its LSPR, the free-electrons in metal particle absorb part of the pulse energy creating a change in the dielectric constant of the metal. In case of silver excited with visible light only the real part of dielectric constant changes[124]. Let $\Delta\varepsilon_m^{'}$ be the change in dielectric constant due to this excitation. For sufficiently small $\Delta\varepsilon_m^{'}$ the change in absorption coefficient of the sample can be written as [85],

$$\Delta\alpha(\lambda) = -\frac{2\pi p}{3\lambda\sqrt{\varepsilon_s}} Im\left[f_j^2(\lambda)\right] \Delta\varepsilon_m^{'}(\lambda). \tag{6.6}$$

Thus, change in absorption measured in an experiment can be directly used to measure the change in the real part of dielectric constant of metal.

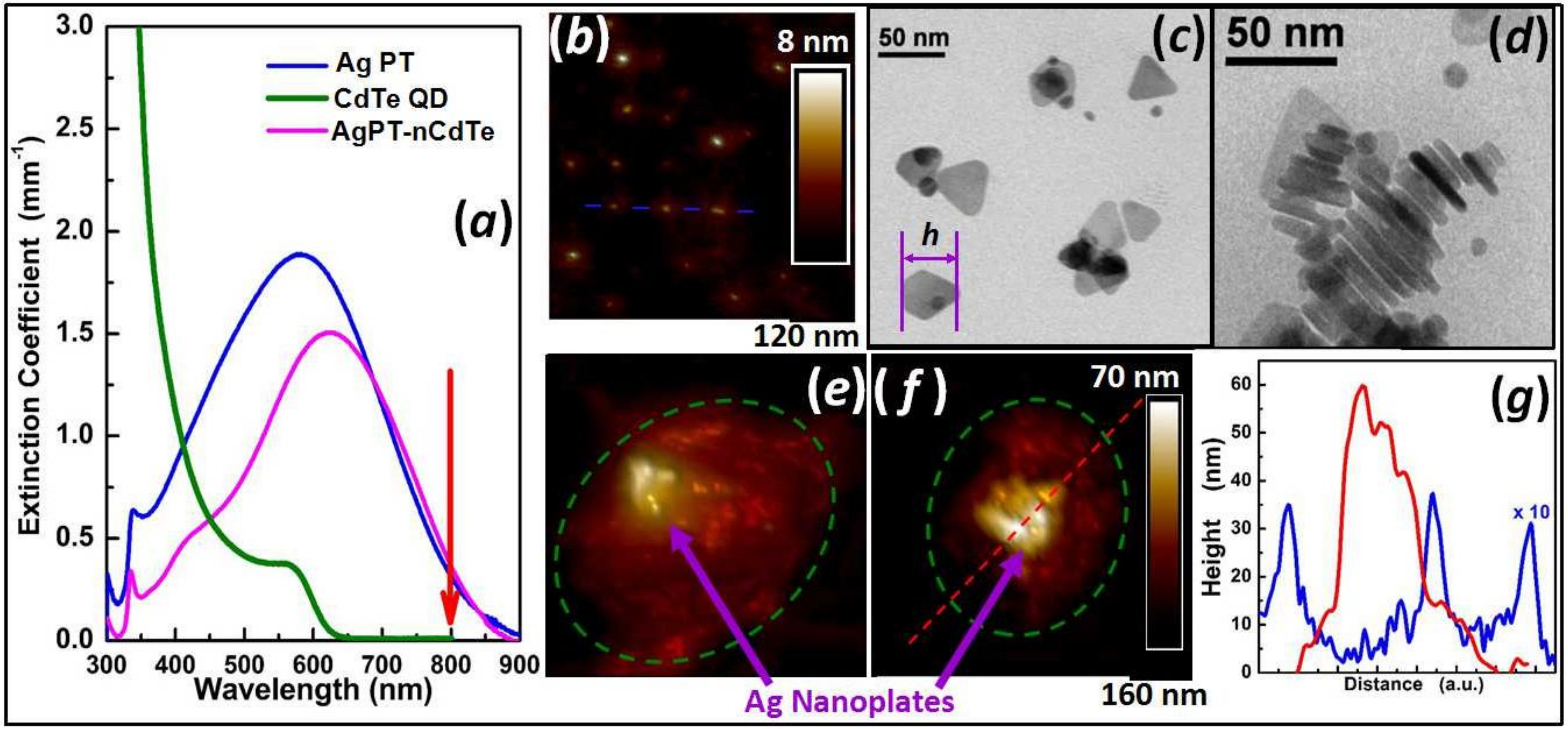

FIGURE 6.1: Optical and structural characterization of Ag PT, CdTe QD and AgPT-nCdTe colloids. (*a*) Extinction spectra of individual colloids and hybrids of mixing ratios ($\gamma = 2.5$). The vertical arrow shows the wavelength at which pump-probe experiment was performed. (*b*) pseudo color AFM topography image of pure CdTe colloid, (*c*) and (*d*) are TEM images of the pure Ag PTs, and (*e*) and (*f*) are the pseudo color AFM topography images of the AgPT-nCdTe HNS. The arrow shows possible location of the Ag PT. Dotted circle shows the area covered by the CdTe QDs. (*g*) the height profile along the straight lines marked in (*b*) and (*f*).

6.2 Optical Response and Structural Characterization of AgPT-nCdTe Hybrid Nanostructure

The optical and structural characterization of Ag PT colloid, CdTe QD colloid as well as AgPT-nCdTe hybrid colloids are shown in Fig.6.1. The overall volume fractions of the Ag PT or CdTe QDs in water were in the order of 10^{-6}. M_γ represents a Ag-CdTe hybrid nanocolloid with $\gamma = V_{NP}/V_{QD}$ formed by mixing V_{NP} volume of the as prepared Ag PT colloid and V_{QD} volume of as prepared CdTe QD colloid. The extinction spectrum of the as prepared CdTe QD colloid shows the 1s(e)-1s(h) excitonic transition at ∼570 nm (Fig.6.1(a)). The size of QDs estimated from this excitonic peak using Peng's empirical formula is 3.4 nm[107]. AFM images of the CdTe colloid shows well separated small particles of average size same as that estimated from the excitonic peak. The extinction spectrum of the Ag PT colloid shows a strong in-plane dipole peak at 582 nm and an out-of-plane quadrupole peak at 339 nm[32, 152]. It also has a broad peak near 430 nm which is due to in-plane quadrupole resonance. From the TEM images we estimate the average height (from middle of the base to maximum height as shown in Fig.6.1 (c)) and thickness of the triangular Ag PT to be ∼ 40 nm and 7 nm respectively.

The extinction spectrum of the hybrid sample $M_{2.5}$ differs from that of a Ag PT colloid (Fig6.1(a)) in some respects. The in-plane dipole peak is shifted by about 40 nm to 622 nm. Similarly, the out-of-plane quarupole peak is shifted to 335 nm, a 4 nm blue-shift. Such red-shift of in-plane dipole peak and blue shift of out-of-plane quadrupole peak is expected if the Ag PT is surrounded by a higher refractive index material compared to water[153]. There is also a overall reduction in the strength of in-plane dipole peak. The measured spectrum of hybrid does not match with that estimated for a colloid containing mixture of non-interacting Ag PT and CdTe QDs. Thus the optical response itself clearly indicates the existence of interaction between the Ag PT and CdTe QDs. The AFM topography measurement of the hybrid nanocolloid (Fig. 6.1(e) and (f)) shows a completely different structure compared to that of individual colloids. In the mixed sample, the AFM image shows presence of much larger aggregates which resemble a structure in which several smaller particles of size comparable to that of CdTe QDs are attached to a larger particle. Such aggregate like structures are expected if each Ag PT was surrounded by several smaller CdTe QDs. Note that the topography structure shown by AFM for the HNS is only indicative. This is due to the fact that the process of drying the sample will distort the true morphology present in the colloid.

Optical spectra of the hybrid nanocolloid sample can also give some information about the structure of AgPT-nCdTe HNS. For calculating the spectra of Ag PT colloid and AgPT-nCdTe hybrid colloid, the code developed by Drain and Flatau, DDSCAT, was used[154, 155]. In this calculation the given nanostructure is replaced by an appropriate lattice of small spherical dipoles. In the present case we replace the nanostructure by a lattice with dipoles greater than 4×10^4. Since Ag PT will be oriented in all possible angles in a colloid it is essential to do the extinction spectrum calculation for all possible orientations of particle. To closely mimic this situation, the extinction spectrum of a given particle is calculated by averaging over the three Cartesian directions [32, 152]. Figure. 6.2 shows the numerically calculated extinction spectrum of a single truncated PT of average experimental dimensions. Clearly the calculated response mimics well the measured optical spectra of Ag PT. The broadening observed in the experimental spectrum compared to the numerical calculation can be explained by the dispersion in particle dimensions present in the sample.

In an earlier experiment, when citrate capped Ag nanospheres were mixed with TGA capped CdTe a HNS is formed which consist of Ag nanosphere surrounded by CdTe QDs[89]. About 70% of the Ag surface was estimated to get covered by CdTe QDs. Assuming a similar coverage on the Ag surface and taking into account the particle diameters and volume factions of individual colloids we have estimated appropriate mixing ratio for the formation of Ag PT-nCdTe HNS. Inf act, the mixing ratio of γ = 2.5 was chosen to ensure such covering of Ag platelet surface by CdTe QDs. Using this model structure for the hybrid, we calculate the optical response of the coated Ag PT as follows.

The coating on top of the Ag PT is expected to be formed of a mixture contains CdTe QDs, the capping agents and water. The dielectric constant of the CdTe QDs coating layer is calculated as follows. First the dielectric constant of a single CdTe QD (ϵ_{qd}) is estimated by following the procedure reported by Marcelo Alves-Santos *et al.* using the measured absorption spectrum of CdTe QD colloid (see section 2.6.1)[102]. Assuming that the CdTe QDs are embedded in an almost water like environment we estimate the dielectric constant of the coating medium (ϵ_{coat}) using the Maxwell-Garnett mixing formula [38],

$$\epsilon_{coat} = \epsilon_s + 3f\epsilon_s \frac{\epsilon_{qd} - \epsilon_s}{\epsilon_{qd} + 2\epsilon_s - f(\epsilon_{qd} - \epsilon_s)}, \tag{6.7}$$

where ϵ_s is the dielectric constant of water and f is the fraction of volume occupied by the CdTe QDs. For the calculation, the thickness of the coating was taken to be 4.4 nm, which corresponds to a coating of one CdTe (3.4 nm) and 0.5 nm on its both sides to account for the TGA coating layer. Figure. 6.2 also shows the calculated extinction cross-section of the Ag PT surrounded by CdTe QDs. All the LSPR peaks, except the out-of-plane quadrupole peak show a strong red-shift. Specifically, the in-plane dipole peak red-shift from 593 nm to 642 nm, a shift of 49 nm. Further, the strength of all the LSPR peaks of hybrid also reduces when compared to that of the uncoated metal particle. Due to the reduction in LSPR strengths as well as red-shift of other LSPR peaks the background extinction reduces in the range 350 nm to 400 nm. This results in the apparent sharpening of the out-of-plane quadrupole peak observed in experimental spectrum of the hybrid. Although this calculation accounts for only the electromagnetic interaction between the CdTe QDs and the Ag

PT, still the changes observed experimental extinction spectra match well with that of calculated for Ag PT with and without CdTe QDs coating. Based on the calculations as well as preparation technique used in the formation of AgPT-nCdTe HNS, the hybrid superstructure (AgPT-nCdTe HNS) is composed of Ag PT surrounded by 180 CdTe QDs.

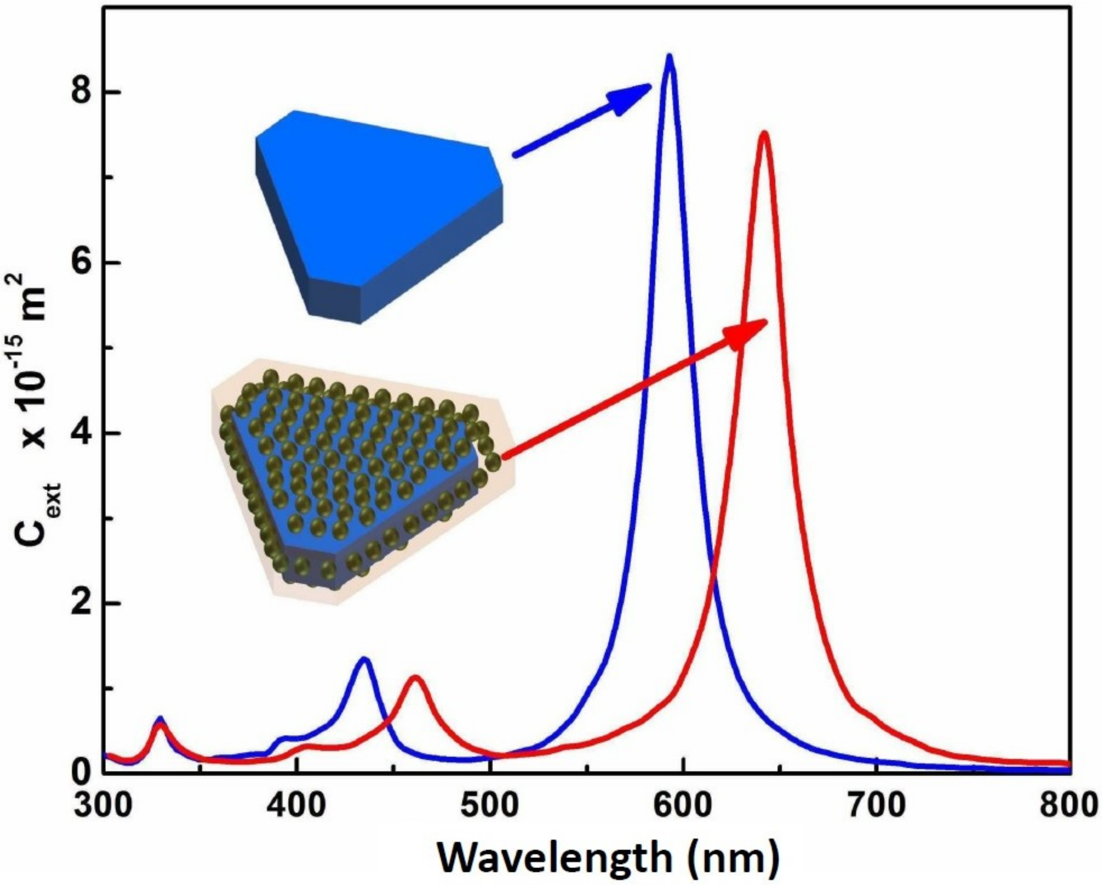

FIGURE 6.2: The numerically calculated extinction cross-section spectra of a single Ag PT with and without coating of CdTe QD embedded layer.

6.3 Ultrafast Transient Absorption of AgPT-nCdTe Hybrid Nanostructure

Having discussed the structural and linear optical response of the Ag PT with and without coating let us now look at their transient response. Transient absorption

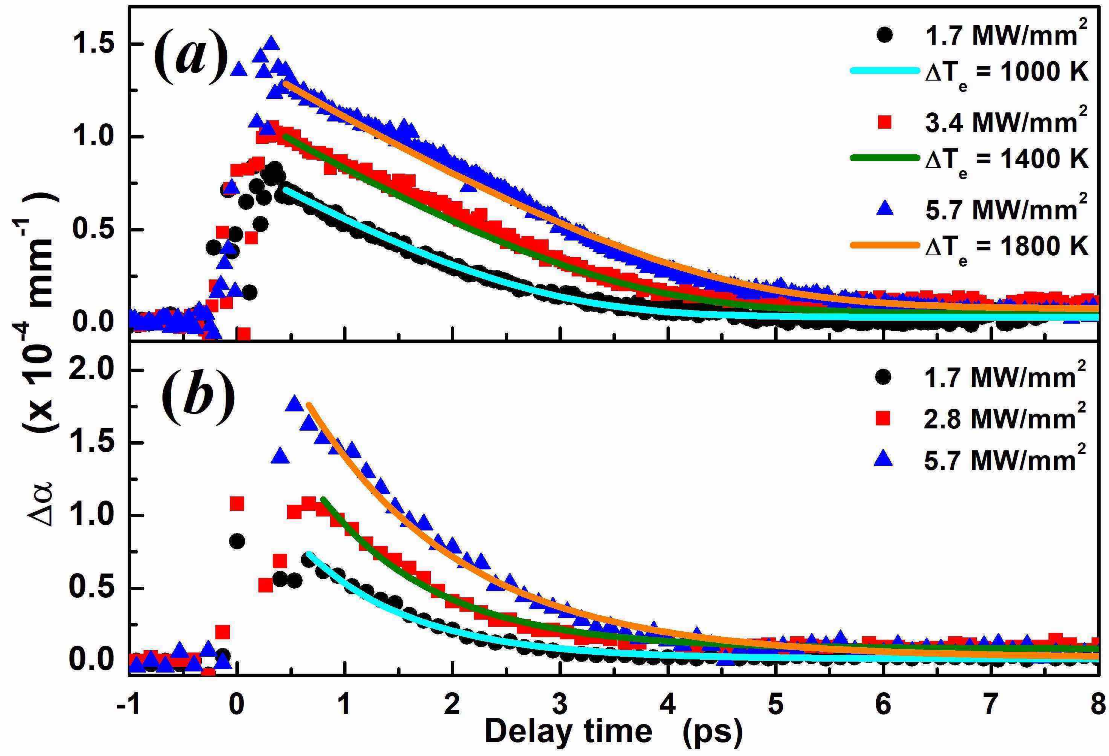

FIGURE 6.3: Transient absorption signal measured at different pump intensities: (*a*) dots are experimental data for pure Ag PT colloid and the solid lines are the best fit to data with TTM and (*b*) dots are experimental data for AgPT-nCdTe colloid and solid lines are the best fit to data with exponential decay function.

measurements were carried out in standard pump-probe geometry using a 80 MHz Ti:sapphire laser operated at 800 nm wavelength. The pulse width of the laser at the sample place was 220 fs. The wavelength at which the measurement was carried out, 800 nm, has energy much lower than that required for excitation of carriers in CdTe QD. However, it is within the inhomogeneously broadened in-plane dipole peak of the PT. Figure 6.3 shows the time evolution of change in absorption ($\Delta\alpha$) of the Ag PT colloid and the hybrid colloid when excited at different pump peak intensities. To ensure identical experimental geometry, the measurements were first performed on Ag PT colloid and then a measured amount of CdTe colloid was added to it. This results in addition of certain amount of water to the Ag PT colloid along with CdTe QDs. The transient absorption of the hybrid has been corrected for this additional dilution so that it can be directly compared with the Ag PT colloid. In both samples, just after arrival of pump pulse (zero delay) the $\Delta\alpha$ increases reaching its maximum within few hundreds of femtoseconds which then recovers within next few picoseconds. With increase in pump intensity the peak change in the $\Delta\alpha$ ($\Delta\alpha_{max}$) also increases. In case of pure Ag PT colloid, the recovery is exponential in nature at lower pump intensities while at higher it becomes non-exponential. However, in case of the hybrid colloid recovery remains exponential even at higher intensities. We find that such changes in the transient absorption response is not observed when only TGA is added to the Ag PT. A colloidal solution containing only the CdTe QDs does not show any transient absorption signal ($\Delta\alpha = 0$). This is expected since CdTe QDs does not absorb when excited at 800 nm. In addition to this we find that adding more CdTe QDs to the hybrid solution $M_{2.5}$ does not change the transient absorption signal substantially. As mentioned before Ag PT in the hybrid sample $M_{2.5}$ are covered fully with CdTe QDs. Adding more CdTe QDs to the sample would only increase the number of unattached CdTe QDs in the colloidal solution and not affect the absorption. Thus the observed changes in the transient absorption signal of Ag PT with and without CdTe QDs are arising due to the attachment of CdTe QDs to the Ag PT (Fig.6.3).

It is known that the dielectric constant of metal, ε_m, depends strongly on the temperature of electrons (T_e)[156]. In case of silver, an increase in the temperature of electrons results in red-shift of the inter-band absorption causing an increase in the real part of the dielectric constant of metal. For small changes in the temperature of electrons (compared to its Fermi temperature) the $\varepsilon_m^{'}$ is expected to change linearly with temperature[85, 125]. An increase in $\Delta\varepsilon_m^{'}$ will red-shift the in-plane dipole LSPR peak (Eq.6.4). Since in the present case probing is being done on the red-side of LSPR a rise in temperature of free electrons will result in increasing absorption[85, 125]. Thus $\Delta\alpha$ in case of a metal colloid can be directly correlated to the temperature of electrons.

$$\Delta\alpha(\lambda) = \eta(\lambda)\Delta T_e, \tag{6.8}$$

where η is a constant which depends on the type MNP and the wavelength of pump and probe beams.

Ultrafast excitation of the metal particle at its LSPR creates plasmon oscillations in coherence with the applied optical field. Once excited these plasmons decay to single particle states through Landau damping within the first few femtoseconds[122]. This results in the absorption of photons and redistribution of electrons in single particle states. Initially the energy distribution among electrons is nonthermal which subsequently undergoes thermalization through electron-electron scattering and the free electrons reaches its maximum temperature by few hundreds of femtoseconds[85, 157]. Thus after the arrival of pump pulse the $\Delta\alpha$ reaches its maximum by few hundreds of femtoseconds (Fig.6.3). At later times the hot-electrons heat the lattice through electron-lattice interaction. Since the specific heat capacity of electrons (C_e) is much lower than that of lattice (C_l), the temperature of free electrons drops which results in recovery of $\Delta\alpha$ (Fig.6.3). The energy exchange between the electrons and lattice can be modeled by the time dependence of electron (T_e) and lattice (T_l) temperatures using a two-temperature model (TTM) through coupled differential equations[158],

$$\frac{\partial T_e}{\partial t} = -\frac{g}{C_e}(T_e - T_l) + \frac{Q(t)}{C_e}, \text{ and} \tag{6.9}$$

$$\frac{\partial T_l}{\partial t} = \frac{g}{C_l}(T_e - T_l). \tag{6.10}$$

where g is the electron-lattice coupling constant and $Q(t)$ is the absorbed power density. In the present case since the pulse width of the laser is much shorter than the typical electron-lattice relaxation time, $Q(t)$ is directly proportional to the intensity of the pump pulse. In case of free electrons, the specific heat capacity depends linearly on its temperature ($C_e = \gamma_0 T_e$). By numerically solving Eqs.6.9 and 6.10, it is possible to estimate the temperature of electrons (T_e) at various pump and probe delays. Using the reported values of g, C_e and C_l, first the recovery of $\Delta\alpha$ for the excitation density 1.7 $\mathrm{MW/mm^2}$ was fit using TTM and Eq.6.8 to estimate the maximum change in temperature of electrons (ΔT_e^M) and η. Now, using the estimated η and only by varying $Q(t)$, which is proportional to the pump power, we obtain the $\Delta\alpha$ for other excitation power densities. The calculated $\Delta\alpha$ values are also shown in Fig.6.3. Clearly the transient changes in the absorption measured by the experiment match well with those estimated using TTM. The peak change in temperature of the electrons was estimated to be 1400 K and 1800 K corresponding to the pump intensities 3.4 and 5.7 $\mathrm{MW/mm^2}$ respectively. For small pump intensities where the change in specific heat capacity of the electrons is negligible, the change in electron temperature $\Delta T_e = T_e - T_0$, will decay exponentially with time. When the ΔT_e is large where the change in C_e cannot be neglected the thermalization takes more time and it is also non-exponential[85, 158]. Such change from exponential behavior to non-exponential can be clearly seen in the measured $\Delta\alpha$ and as well as in the estimated ΔT_e (Fig.6.3).

In Fig.6.4 we compare the transient absorption signals measured for hybrid and pure Ag PT colloids at a pump intensity 5.7 $\mathrm{MW/mm^2}$. Two significant changes are observed in transient absorption signal of Ag PTs when CdTe particles are attached; first, the peak change in $\Delta\alpha$ of hybrid increases by about 44% when compared to that of pure Ag PT colloid. The second is the non-exponential nature of $\Delta\alpha$ recovery observed in case of Ag PT colloid changes to exponential for the case of hybrid. A fit to the decay part of the transient data with a single exponential function gives a recovery time of $\sim$ 1.33 ps.

As discussed earlier the observed peak shift in the LSPR peaks can be attributed to the coating of CdTe surrounding the Ag PTs. Thus even in the case of hybrid colloid the free-carriers absorb incident light through plasmon resonance and the transient change in $\Delta\alpha$ should be attributed to the change in dielectric constant of metal. This is because the excitation at 800 nm cannot directly excite carriers in the CdTe QDs and would not change its properties. Another point to note is that though

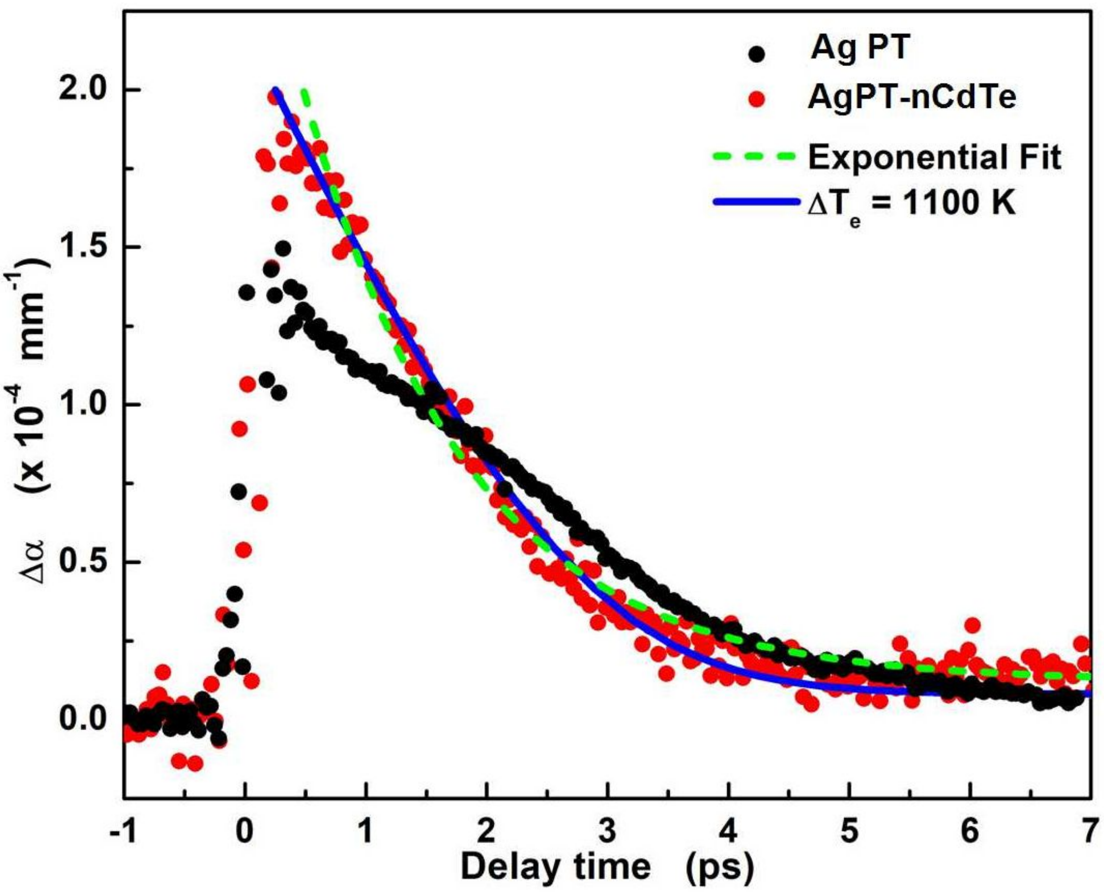

FIGURE 6.4: Comparison of transient absorption signal of pure Ag PT colloid and AgPT-nCdTe colloid at a given pump intensity 5.7 MW/mm^2. The solid lines are the fit to data with TTM for pure Ag nanoplate colloid and exponential fit for hybrid colloid.

there is a reduction in the in-plane LSPR peak of hybrid when compared to Ag PT colloid, at 800 nm the absorption coefficient of the hybrid is slightly more than that of pure Ag PT colloid due to the red shift (Fig.6.1). Thus under similar excitation condition the energy absorbed by the hybrid cannot be less than that of pure Ag PT colloid. Hence, even the hybrid should have shown a non-exponential behavior in the recovery of $\Delta\alpha$. However, this is not the case. If ΔT_e^M estimated using TTM is directly used for fitting the recovery of transient absorption of hybrid it fits well with a ΔT_e^M of 1100 K but with a different η. Thus the time dependence shows that the overall temperature increase in Ag PTs coated with CdTe QDs is clearly much lower than that of uncoated Ag PTs for same excitation power. The decay time, τ, estimated by fitting an single exponential decay function to each pump intensity is shown in Fig.6.5(*a*). At lower intensities the decay time increases with it while at higher intensities (> 4 MW/mm^2) the decay time does not increase much and gets saturated to about 1.35 ps.

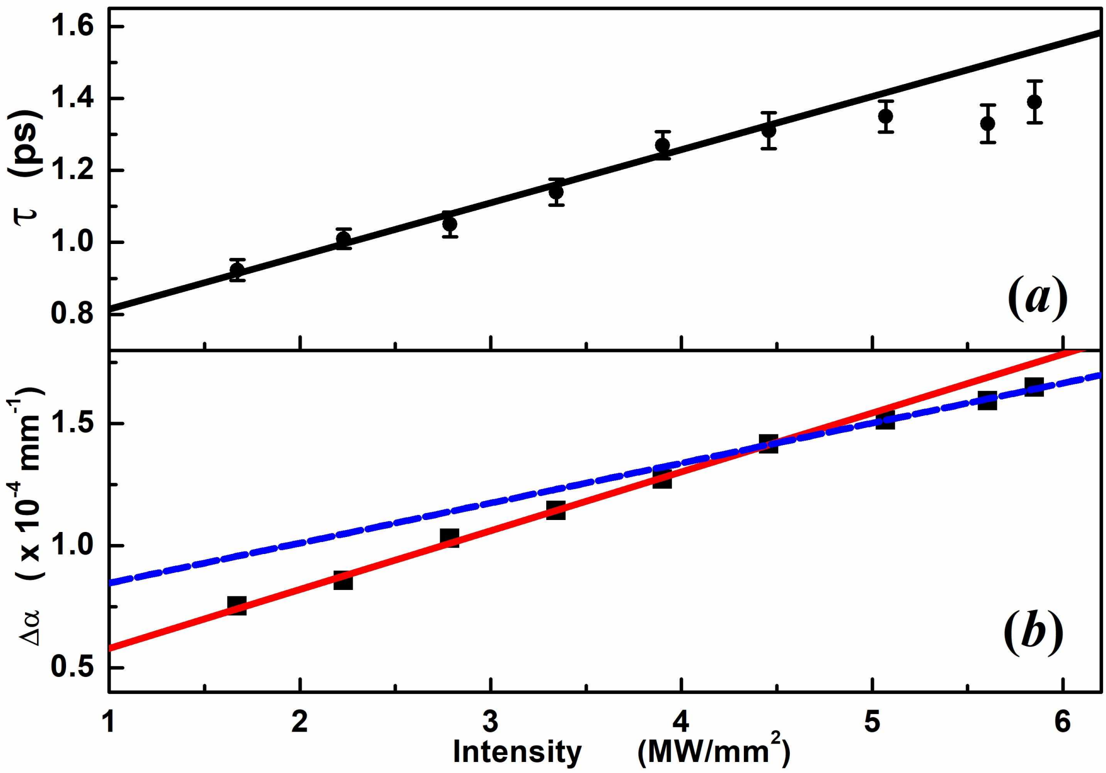

FIGURE 6.5: The dependence of (*a*) recovery time and (*b*) $\Delta\alpha_{peak}$ of transient absorption signal of AgPT-nCdTe colloid on pump intensity.

As mentioned earlier, in MNP, the plasmons decay by exciting electrons to higher energy single particle states within first few femtoseconds after excitation. However, when a semiconductor is in contact with metal, the incident photon may directly excite an electron from metal to the conduction band of semiconductor through the interface without exciting plasmon[63]. Another possible scenario is that the incident photon may excite a plasmon in the metal and the plasmon decay by exciting an electron from metal to the conduction band semiconductor through the interface[63]. However, in the present case both of these excitations are less likely since SQD are attached to metal through capping agents. The nonexistence of direct interface between metal and semiconductor will reduce the possibility of such spatially de-localized transitions. The plasmon induced hot-electron transfer is another well-known process that is possible when the metal nanoparticle is attached to a semiconductor QD. As in the unattached metal nanoparticle, the plasmon decays by exciting an electron to a higher energy state. This is then followed by the transfer of hot-electron to the semiconductor. Such transport of hot carriers can happen even before the thermalization of carriers within metal nanoparticle [17]. In the present case it is possible that once plasmons are excited, hot-electrons in Ag PT may move to the attached CdTe. However, these electrons cannot recombine inside CdTe since there are not that many hole states present there. In the hybrid sample we did not observe any emission even at the maximum intensity at which the pump-probe measurement was performed. N. Mondal and A. Samanta have shown that when carriers are excited in CdTe QDs the cold electrons in the conduction band edge are able to get transported to the attached Ag nanospheres within a few picoseconds [20].

A model based on transport of hot carriers from metal to semiconductor within first few hundreds of femtoseconds and their subsequent return after relaxation within conduction band of CdTe to metal nanoparticle in next few picoseconds can explain the observed change in the behavior of transient absorption in the HNS (Fig.6.6). If hot electrons which can increase the final temperature beyond 1100 K hop to semiconductor within first 0.45 ps (thermalization time for electrons) then the maximum temperature reached by the free electrons will remain close to this value. When excited with even higher intensities, more number of hot electrons will get generated inside the metal and will get transferred to CdTe QDs keeping the overall temperature clamped to 1100 K. This explains why the τ does not increase with pump intensity beyond ~ 1.35 ps (Fig.6.5(a)). This temperature threshold should depend on the band alignment between the metal and semiconductor as well as the properties of linking molecule [70, 159]. At later times the hopped carriers will relax and accumulate at the conduction band edge from where they will hop back to the

Ag PT. This is due to the fact that there are no holes present in CdTe QD and at the same time Ag is now positively charged. Such return of carriers for charge neutrality has also been observed earlier[20, 82]. The electron-lattice thermalization time guided by the final temperature reached by the free electrons in metal T_M and the relaxation time of electrons from CdTe to Ag PT will decide the final recovery time of $\Delta\alpha$.

As discussed earlier, $\Delta\alpha_{max}$ should be proportional to the maximum change in the temperature of free-electrons. If the final temperature reached by the free-electrons in the case of hybrid sample is clamped at 1100 K then the $\Delta\alpha_{max}$ should not increase at higher intensities. For example, at a pump intensity 5.7 MW/mm^2, the estimated temperature of free electrons in Ag PT is 1800 K whereas the expected temperature reached by hybrid is close to 1100 K. Thus it is expected that the $\Delta\alpha_{max}$ of hybrid sample should be much lower than that measured for Ag PT colloid at 5.7 MW/mm^2. On the other hand $\Delta\alpha_{max}$ measured for hybrid colloid (1.9×10^{-4} mm^{-1}) is much higher than that measured for pure Ag PT colloid (1.4×10^{-4} mm^{-1}). In fact when the maximum temperature reached by free-electrons in Ag PT is $\sim$ 1100 K the $\Delta\alpha_{max}$ is only 0.84×10^{-4} mm^{-1} (Fig.6.3(a)).

According to Drude model the contribution to dielectric constant of the metal from free-electrons (ε_m^{free}) at the probe frequency ω is given by

$$\varepsilon_m^{free} = 1 - \frac{\omega_0^2}{\omega^2 + i\omega\gamma}. \tag{6.11}$$

where the bulk plasma frequency ω_0 is given by,

$$\omega_0 = \sqrt{\frac{Ne^2}{\epsilon_0 m}}, \tag{6.12}$$

where N is the number density of free-electrons in the metal, e and m are elementary charge and mass of electron and ϵ_0 is the permittivity of free space. If some of the electrons move out of metal nanoparticle then the number density of free-electrons will reduce the bulk plasma frequency (Eq.6.12). Reducing the effective density of free-electrons to red-shift the plasma frequency has been used earlier for tuning optical response of metamaterials for applications in low frequency regimes [160, 161]. Using Eq.6.11 the change in real part of dielectric constant of metal due to a change in number density ΔN can be written as

$$\Delta\varepsilon_m^{'}(\lambda) = -\frac{e^2}{4\pi^2 c^2 m\epsilon_0}\lambda^2\Delta N = C\lambda^2\Delta N. \tag{6.13}$$

Here C is a constant (= - $e^2/4\pi^2c^2m\epsilon_0$). Now the condition for LSPR given by Eq.6.4 will be satisfied at a slightly longer wavelength. This will result in a red-shift of LSPR peak. This is same as shifting the entire spectrum of the hybrid slightly towards longer wavelength. Clearly once again any reduction in the number density, say by ΔN, will lead to an increase in absorption. Thus the overall change in the absorption should not only depend on the ΔT_e as given by Eq.6.8 but should also depend on ΔN. Using Eq.6.6, the total change in $\Delta\alpha$ can be written as,

$$\Delta\alpha(\lambda) = \eta(\lambda)\Delta T_e + C\xi(\lambda)\lambda\Delta N \tag{6.14}$$

where ξ is a constant which depends on the wavelength. A functional form of the ξ can be obtained using Eq.6.6 and Eq.6.16. We attribute the increase in $\Delta\alpha_{Max}$ observed in case of hybrid to this additional contribution that comes from electrons hoping out of metal nanoparticle. At higher pump intensities, although the increase in temperature is now clamped to a particular value, a larger number of hot carriers will get transfered to CdTe increasing the $\Delta\alpha_{Max}$. Thus in a hybrid sample at lower pump intensities the increase in $\Delta\alpha_{Max}$ is largely governed by the contribution through ΔT while at higher pump intensities ΔN also contributes to increase $\Delta\alpha_{Max}$. In Fig.6.5(b) we show the dependence of $\Delta\alpha_{peak}$ of Ag-CdTe hybrid sample on the pump intensity. The $\Delta\alpha_{Max}$ always increases with pump intensity but at different rates above and below 4 MW/mm^2. Linear fit to the data at these two different intensity regimes, one for the intensities lower than 3.5 MW/mm^2 and one for that larger than 4 MW/mm^2 are also shown in Fig.6.5(b). Clearly the slopes of these two lines are different indicating the difference in origin of their processes. When carriers are excited in TiO$_2$ of an Ag-TiO$_2$ core-shell HNS, its LSPR peak was found to shift due to transient changes in the dielectric constant of the coating[162]. In the present case LSPR shifts due to the changes in dielectric constant of metal due to carriers moving out of it. It would be very useful if it is possible to estimate the actual number of electrons hopping to CdTe QDs.

6.4 Counting the electrons hopping in AgPT-nCdTe Hybrid Nanostructure

Let us calculate the number of electrons hopping out of Ag PT in case of the hybrid nanoparticle when the pump intensity is 5.7 MW/mm^2. First we estimate the contribution to $\Delta\alpha_{Max}$ only from the change in number density by subtracting the $\Delta\alpha_{Max}$ of pure Ag PTe colloid when it T_M is $\sim$ 1100 K. The contribution of change in number density to the change in absorption ($\Delta\alpha_{\Delta N}(\omega)$) is (i.e. only the second term in Eq.6.15),

$$\Delta\alpha(\omega, \lambda, \Delta N) = C\xi(\omega)\lambda\Delta N \tag{6.15}$$

As mentioned earlier the change in number density when electrons hop out of Ag PT results in shifting the LSPR peak of the Ag particle. Then the overall change in $\Delta\alpha$ caused by ΔN for a given λ can be estimated using the $\Delta\alpha$ caused by a small change in wavelength near λ for a given N. For a small change in wavelength, $\Delta\lambda$, the change in real part of dielectric constant can be estimated using Eq.6.11 and is given by,

$$\Delta\varepsilon_m^{'}(N, \Delta\lambda) = -2\frac{e^2}{4\pi^2 c^2 m\epsilon_0}\lambda N\Delta\lambda \tag{6.16}$$

Thus the dependence of absorption on $\Delta\lambda$ can be written as,

$$\Delta\alpha(\omega, \Delta\lambda, N) = -2C\xi(\omega)N\Delta\lambda. \tag{6.17}$$

For small change in absorption the dependence of linear absorption coefficient on wavelength near the λ_p can be used to determine the constant that defines $\Delta\alpha(\omega, \lambda, \Delta N)$. In other words,

$$\Delta\alpha(\omega, \lambda, \Delta N) = \frac{m_{exp}\lambda}{2N}\Delta N. \tag{6.18}$$

where m_{exp} is the ratio between $\Delta\alpha$ and $\Delta\lambda$. The number of electrons moving out of a single Ag PT (Δn) of volume V can be estimated using,

$$\Delta n = \frac{2N}{m_{exp}\lambda}\Delta\alpha(\omega, \lambda, \Delta N)V. \tag{6.19}$$

Using the variation of linear absorption spectrum of the hybrid sample around 800 nm, we estimate the slope m_{exp}. Based on this, we find that about 200 electrons are moving out & in of the Ag PT when the hybrid is excited at 5.7 MW/mm^2. Similarly for a pump intensity of 3.4 MW/mm^2, this number is about 70. This method of estimating number of electron hopping in and out of MNP is useful for quantifying charge transport process in HNS. This in turn will help is optimizing the HNS for several application. Having studied charge exchange between Ag PT and CdTe QD, it is also important to study the effect of charge transport on PL properties of AgPT-nCdTe HNS.

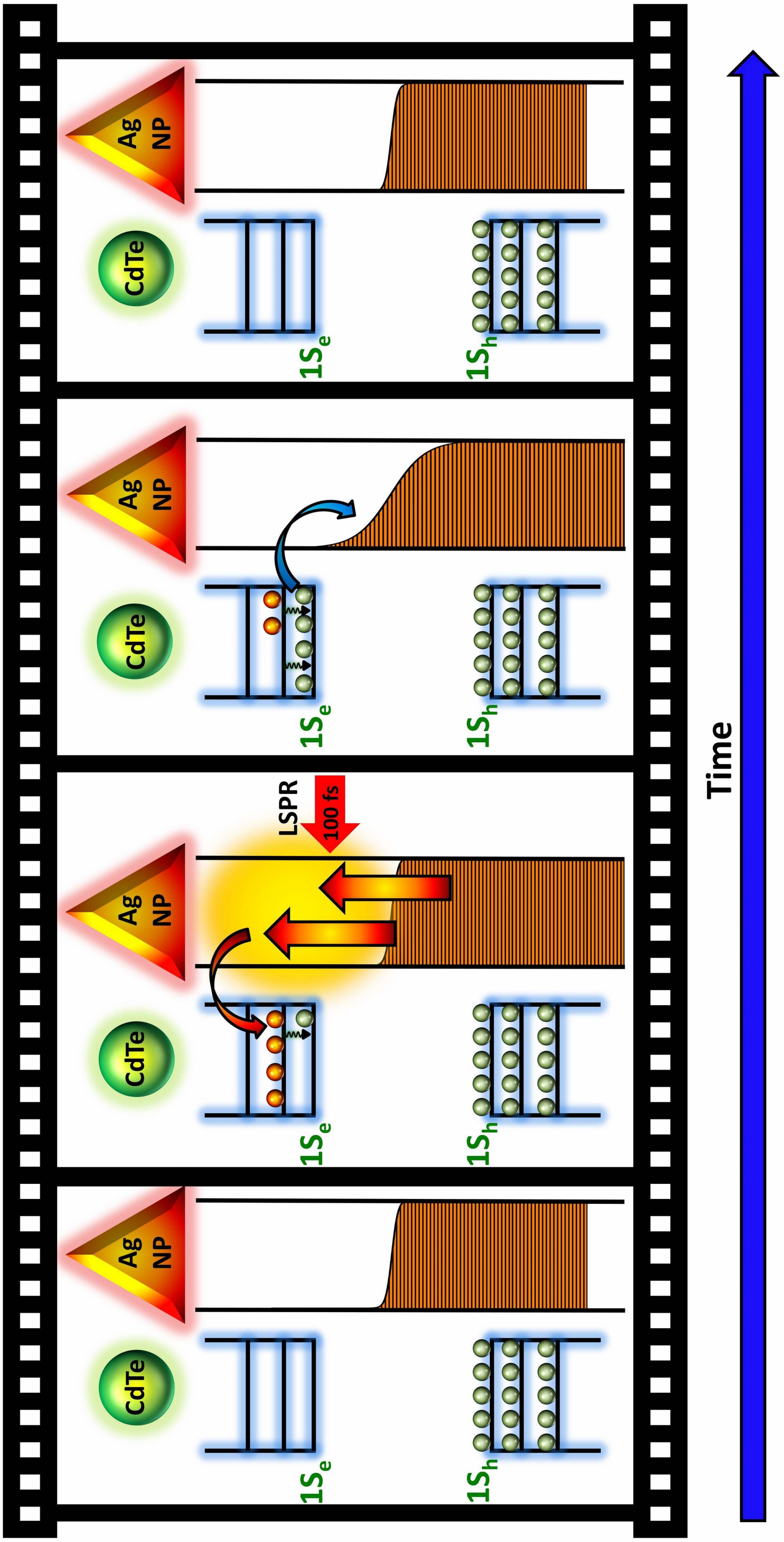

FIGURE 6.6: Schematic illustration of the photo-induced electron transfer process from metal to semiconductor (red arrow) and from semiconductor to metal (blue arrow).

6.5 Radiative Properties of AgPT-nCdTe Hybrid Nanostructure

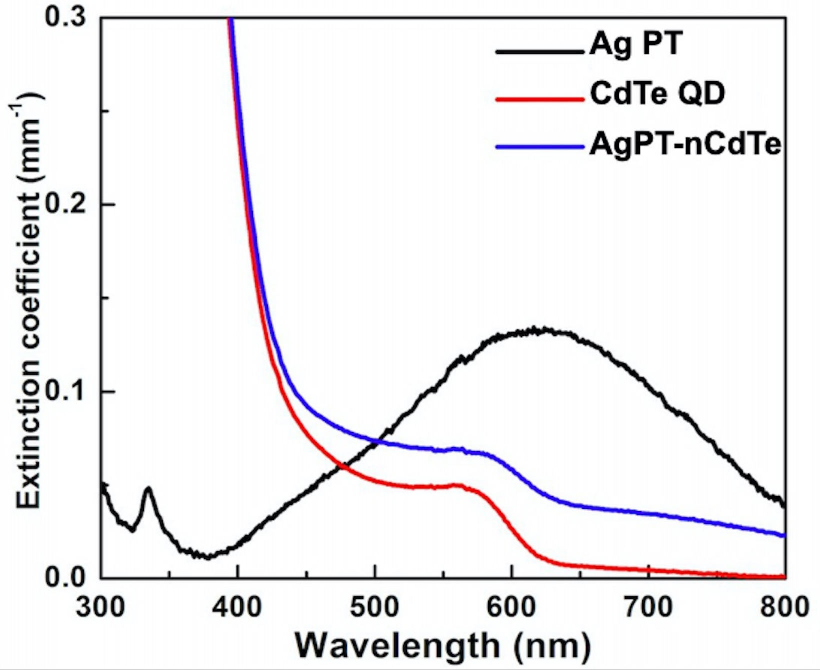

FIGURE 6.7: (*a*) Extinction spectrum of the colloidal solutions of Ag PT, CdTe QD and AgPT-nCdTe colloid ($M_{0.5}$).

The extinction coefficient of AgPT-nCdTe HNS, $M_{2.5}$, is dominated by Ag PT most probably due to its large volume, hence we did not get any measurable PL emission. Therefore, to study the radiative property of HNS formed by Ag PT and CdTe QDs, we prepared Ag PT of smaller volume and HNS was formed by mixing it with CdTe QDs at γ = 0.5. Figure 6.7(*a*) shows the extinction spectra of the colloidal solutions of Ag PT and CdTe QD in the mixing ratio, γ = 0.5. TEM measurement of Ag PT shows particles of an average diameter and thickness of 34 nm and 5.2 nm, respectively (Fig.6.8). The extinction spectra of the Ag PT colloid shows an in-plane dipole LSPR peak around 604 nm and an out-of-plane quadruple peak at 335 nm (Fig.6.7)[152].

Figure 6.9(*a*) and (*b*) shows the measured PL spectra of the bare CdTe QD and

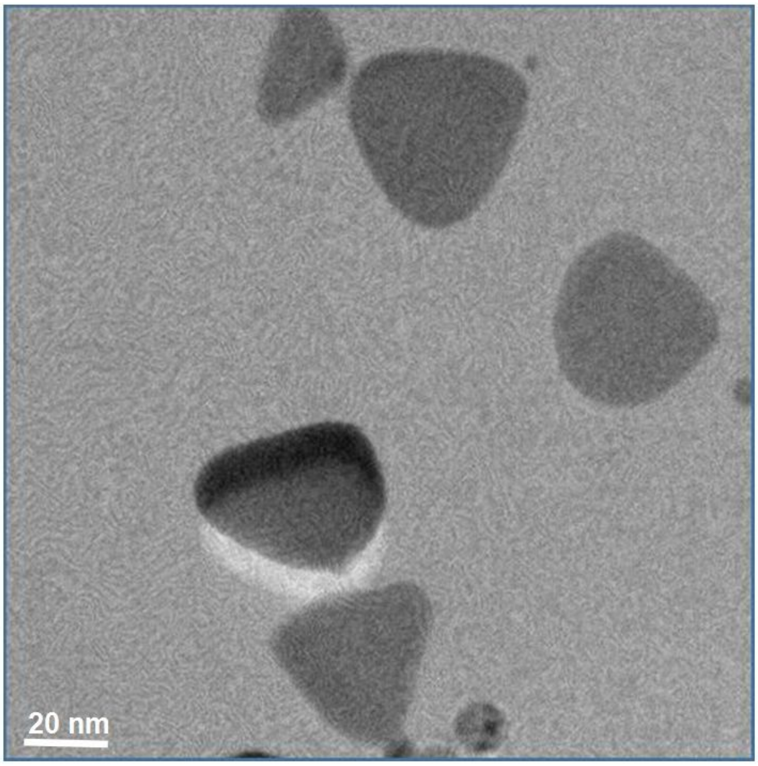

FIGURE 6.8: TEM image of a comparatively smaller Ag PT particles.

AgPT-nCdTe colloids when excited at 405 nm and 550 nm, respectively. PL measurement was done with the setup described in Chapter 2 (sec.2.4). We have used the same PL measurement setup under same excitation conditions for all the samples. The PL spectrum is nearly Gaussian with a long tail on the higher energy side. When compared to the PL emission from CdTe QD, the hybrid sample AgPT-nCdTe shows three well distinct changes: (i) the strength of the PL at its peak emission got quenched at both these excitation wavelengths, (ii) there is an enhancement in the PL emission at the higher wavelength side and (iii) the total integrated area under the PL spectrum remains nearly same compared to that of CdTe QD colloid i.e.102% and 96% for 405 nm and 550 nm excitation, respectively. Due to variation in size, the CdTe QDs present in the sample are expected have PL peak at slightly different wavelengths. This contributes to a broadened PL spectrum for the CdTe QD colloid. The PL measured for excitation at 405 nm showed a finite emission at 550 nm. Thus, when excited at 550 nm, QDs having emission above this energy would

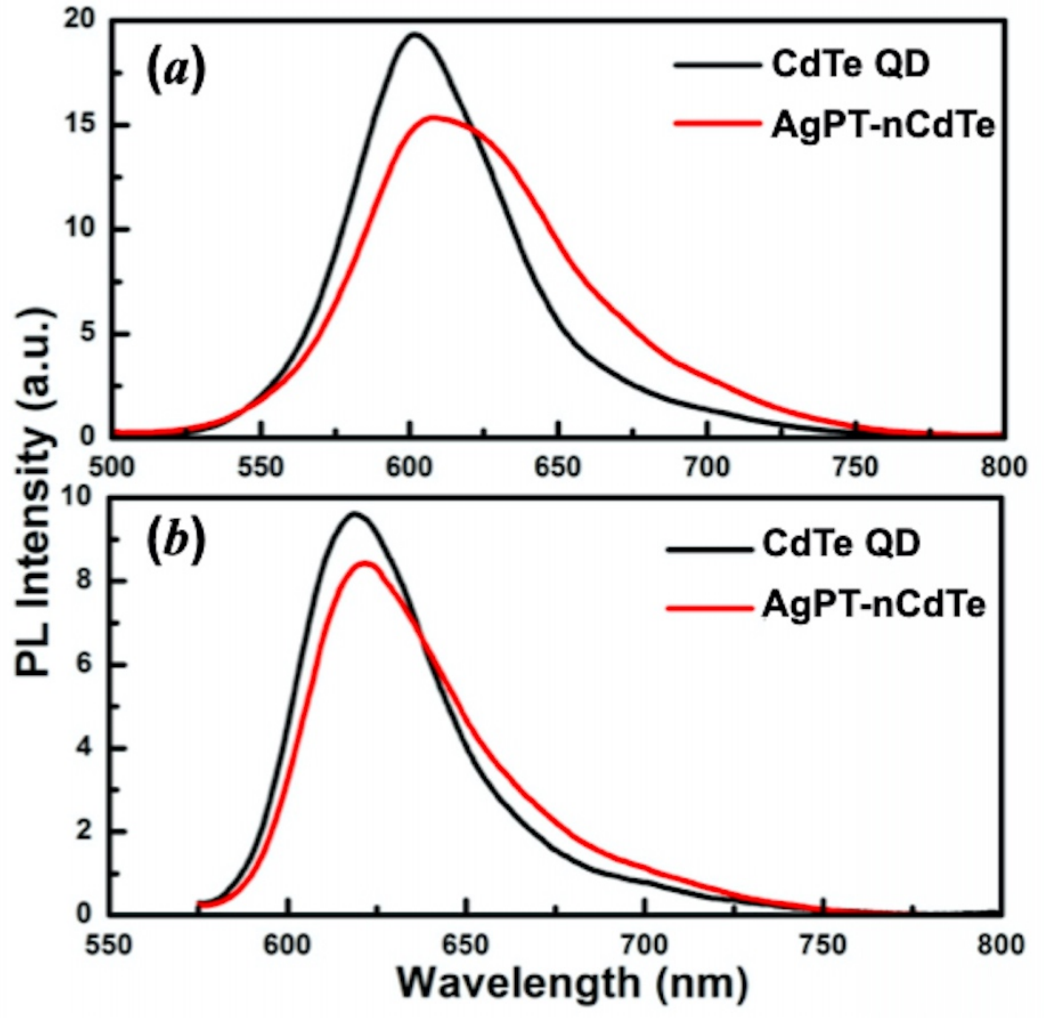

FIGURE 6.9: Photoluminescence spectrum of CdTe QD and AgPT-nCdTe colloids when excited at (*a*) 405 nm and (*b*) 550 nm.

not contribute to the emitted PL spectrum. Hence, a spectral narrowing is expected when excited close to the absorption edge. However, such spectral narrowing remains same for the AgPT-nCdTe hybrid sample also. Since we are comparing both the samples for each excitation wavelength the change in the PL spectrum should be attributed to the hybrid formation only.

It is well known that the presence of MNP can lead to quenching or enhancement in the PL emission from an SQD placed nearby. Several factors like nature of the individual materials, the shape of the final nanoaggregate, the distance between the metal and semiconductor, the nature of junction between them and linking medium are known to play a role in enhancing or quenching the PL emission[17, 70, 87].

Presence of MNP is also known to introduce additional defects states in CdTe QD due to ligand exchange while forming the HNS[69, 71]. In the present case, the quenching of PL strength at the peak along with an enhancement in the PL at the lower energy side clearly indicates that part of the charge carriers from the band edge are relaxing to the newly formed defect states from which they further decay radiatively. The fact that the integrated area under the PL spectrum of AgPT-nCdTe remains nearly the same as that of bare CdTe QD colloids indicates that nearly all carriers relaxed to the defect states can relax radiatively.

Figure 6.10 and Figure 6.11 shows that the temporal evolution of the PL of CdTe QD colloid when excited at 405 nm and 550 nm respectively along with the measured IRF. The temporal evolution of PL measured for CdTe QD colloid when excited at both the photon energies fits well to a tri-exponential decay function convoluted ($\otimes$)

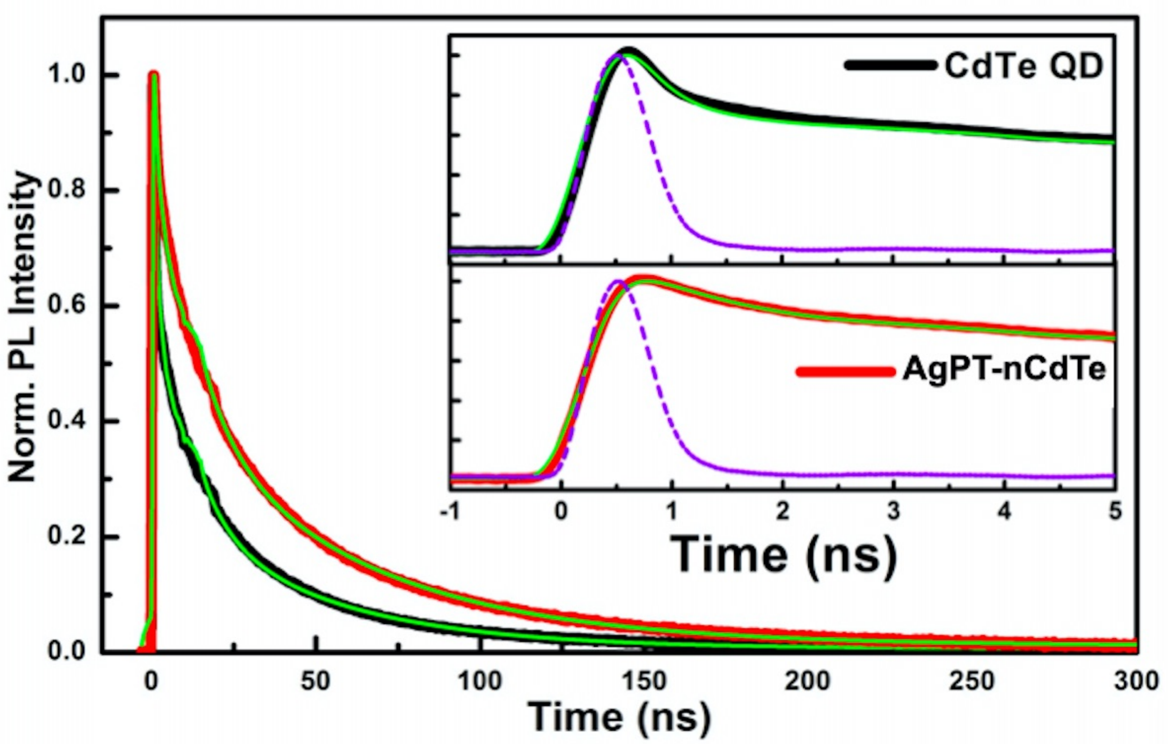

FIGURE 6.10: Time-resolved PL decay kinetics of CdTe QD and AgPT-nCdTe colloids when excited at 405 nm. Inset shows the same time-resolved PL zoomed in time. The dotted line shows the measured IRF. The solid lines are the best fit to the corresponding data using Eq.6.20.

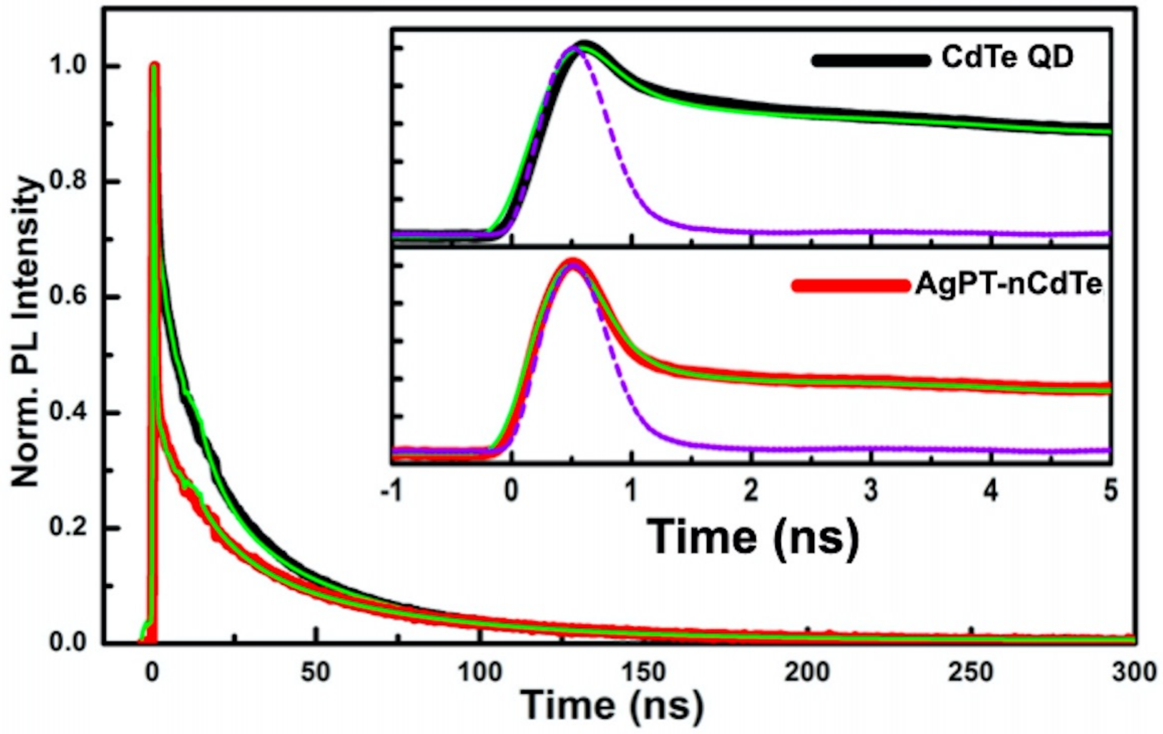

FIGURE 6.11: Time-resolved PL decay kinetics of CdTe QD and AgPT-nCdTe colloids when excited at 550 nm. Inset shows the same time-resolved PL zoomed in time. The dotted line shows the measured IRF. The solid lines are the best fit to the corresponding data using Eq.6.20.

with the experimental IRF (I_{IRF}), given by

$$F(t) = \left(I_{IRF} \otimes \sum_{i=1,2,3} A_i e^{\frac{-t}{\tau_i}} \right) \tag{6.20}$$

where A_i is the i^{th} signal amplitude corresponding to the time constant (decay time) τ_i.

The best fit parameters obtained by fitting Eq.6.20 to the experimental CdTe QD PL is summarized in Table-6.1 and the best fit curves are shown in Fig.6.10 and Fig.6.11. In case of AgPT-nCdTe, when excited at 405 nm, the three different time constant, τ_1, τ_2 and τ_3 turns out to be 0.70 ns, 8.7 ns and 200 ns respectively. The shortest and longest decay times of AgPT-nCdTe increased by approximately three times compared to that of the bare CdTe QD, while the τ_2 showed only a slight

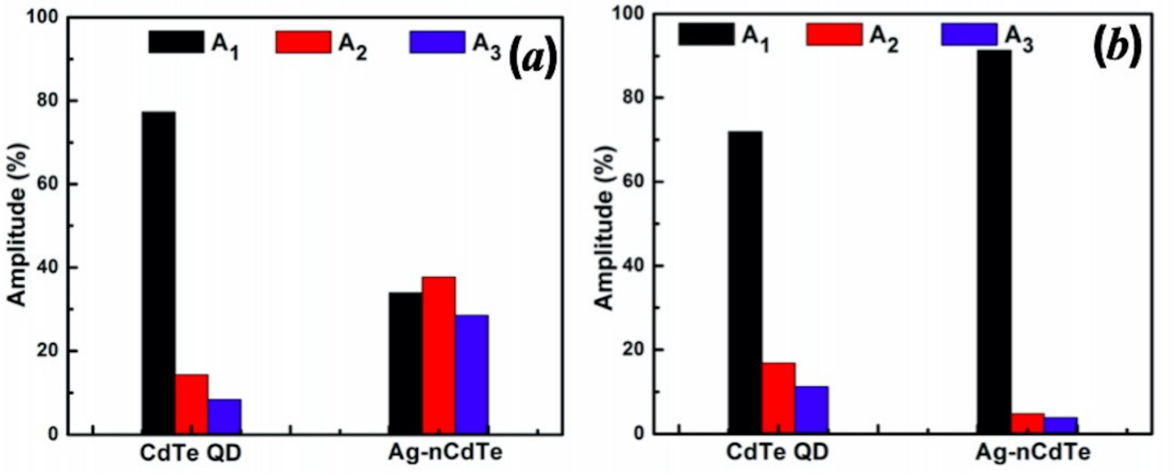

FIGURE 6.12: The amplitudes of the best fit parameters obtained by fitting Eq.6.20 to the experimental data of CdTe QD and AgPT-nCdTe colloid when excited at (*a*) 405 nm and (*b*) 550 nm.

TABLE 6.1: Best fit parameters obtained by fitting Eq.6.20 to the experimental time-resolved PL of CdTe QDs and AgPT-nCdTe colloids.

Sample	λ_{exc} (nm)	A$_1$ %	τ_1(ns)	A$_1$%	τ_2(ns)	A$_1$ %	τ_3 (ns)
CdTe QD	405	77	0.23± 0.02	14	7± 0.2	9	65± 2
	550	72	0.23± 0.01	17	7± 0.1	11	63± 2
AgPT-nCdTe	405	34	0.7± 0.02	38	8.7± 0.2	28	215± 5
	550	91	0.15± 0.001	7	6.5± 0.4	4	120± 3

increase. The amplitude of each decay component, A_i's, has also changed dramatically compared to the bare CdTe QD colloid. The amplitude of the fast lifetime component (A_1) has substantially decreased while the other two amplitudes, A$_2$ and A$_3$, have increased (shown in Fig.6.12). Figure 6.11 shows the temporal evolution of the PL of AgPT-nCdTe colloid when excited at 550 nm (see Table-6.1 for best fit parameters). When compared to CdTe QD colloid, the τ_1 of AgPT-nCdTe becomes even shorter, 0.15 ns, with a strong increase in the corresponding amplitude A_1. This is completely opposite to that when excited at 405 nm, where it has become slower along with a reduction in amplitude compared to that of CdTe QD. The τ_2 once again shows only a slight change compared to that of CdTe QD, and the τ_3 has increased by a factor of two.

Figure 6.13 shows the comparison of PL decay kinetics for samples when excited

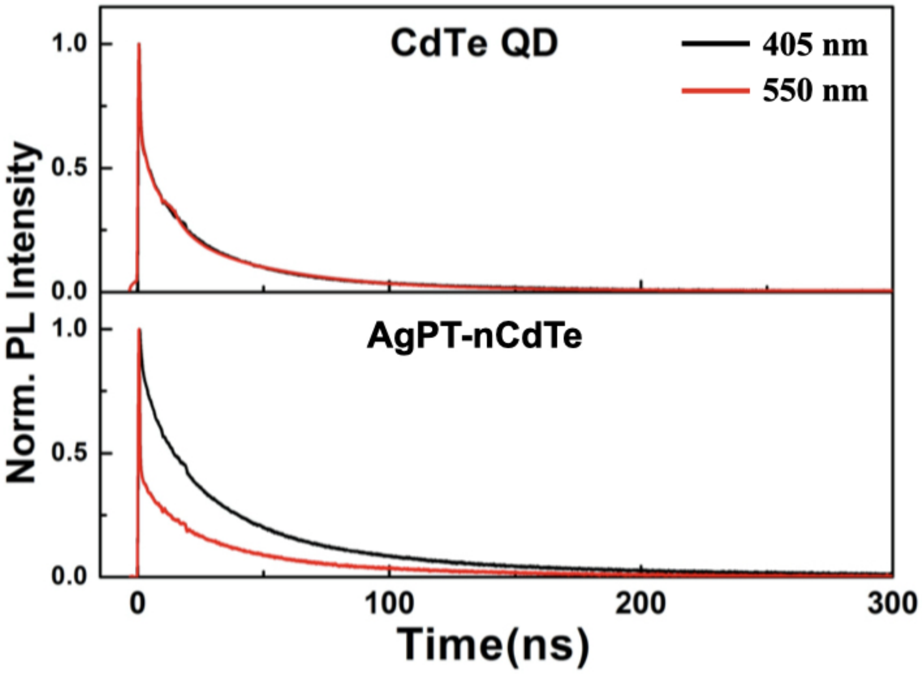

FIGURE 6.13: Comparison of time-resolved PL decay kinetics of CdTe QD and AgPT-nCdTe colloids when excited at 405 nm and 550 nm.

at different excitation wavelengths. It has been observed that PL decay kinetics of CdTe QD remains same for both the excitation wavelength. On the other hand, hybrid, AgPT-nCdTe shows variation in PL decay. This kind of excitation energy dependent PL violates the well known Kasha's rule. Similar violation of Kasha's rule has been observed in colloidal QDs attached to Au NP due to 'on" or "off" excitation of plasmon resonance that affects the plasmon-exciton interaction[145, 163].

As mentioned earlier, when an MNP is brought close to the SQD, several charge and energy transfer processes occur between these two materials. In such a hybrid, it is known that when carriers are excited in SQD, it can get transported to the neighboring MNP[20, 164]. Any such carrier transport would result in quenching of the radiative emission and show up as an increase in the amplitude of the fast decay component, A_1, and the reduction in A_2 and A_3. Although this matches well to the observed kinetics (Table-6.1) when excited at 550 nm, at 405 nm excitation we find a completely opposite situation where A_1 reduces with an increase in A_2 and A_3. Hence a simple charge transport model cannot consistently explain both the observed changes. In addition, several groups have also reported energy transfer between the metal and semiconductor components of the hybrid like foster resonance energy transfer (FRET) and plasmon-induced resonance energy transfer (PIRET) [90–94]. In these process, energy get transferred non-radiatively from an emitter to an absorber by dipole-dipole coupling which occur when the emitter and absorber spectrally overlap[90–94]. Similar to the charge transport case, these processes would also result in increasing A_1 with the reduction of A_2 and A_3. Once again, these processes also cannot explain the observed kinetics at 405 nm, excitation. Further, the presence of MNP would also create additional defect states at the surface of SQD[22, 40, 43, 88]. The excited charge carriers in SQD can get transported to these defect states and can relax further down radiatively. Such relaxation would result in a reduction of A_2, the amplitude of radiative recombination, coupled with a PL emission having a long lifetime. Such changes are also not observed in the present case. Thus all these reported processes cannot consistently explain our experimental observations.

In the present case, the aspect ratio of Ag PT is such that its in-plane dipole LSPR peak overlaps with that of CdTe QD emission wavelength. When AgPT-nCdTe is excited at 405 nm, the LSPR does not get excited in Ag PT; however, excitation the photon energy is sufficient to excite carriers in the CdTe QD. Ultrafast pump-probe measurements on such Ag nanoparticle-CdTe QD hybrid systems when excited away from the LSPR, showed that electrons excited deep into the conduction band can get transported to Ag NP in subpicosecond and picosecond time scales creating a charge imbalance between them[20]. These carriers, which are now in Ag nanoparticle, return to CdTe QD through defect states in a few picoseconds time scale. Besides, the electrons in the CdTe QD can also relax to the newly formed defect states from which they can decay further down. Similarly, in this case, at 405 nm, LSPR in AgPT is not excited, therefore presence of AgPT will quickly reduce the number of carriers in the CdTe QD by electron transfer from CdTe QD to Ag PT. Such a reduction in the number of charge carriers in CdTe QD will strongly reduce the efficiency of the Auger like non-recombinations (as discussed in Chapter 5) and this results in reduction of the amplitude of fast lifetime component, A_1. The reduction in the efficiency of non-radiative recombination can increase the PL emission from the band to band recombination[18]. Spectral overlap between PL emission wavelength and LSPR peak can also enhance the PL emission strength of CdTe QD in the presence of MNP in a way like antenna effect [165, 166]. We attribute the increase in A_2 to the antenna effect and band to band recombination due to the reduction in non-radiative recombinations. The carriers which are transported to the defect states will also relax radiatively increasing the emission from defect states[20, 143]. The increase in A_3, the amplitude of the long time constant (τ_3), can be attributed to the radiative relaxation through the defect states. Note that the decay, τ_3, in the case of AgPT-nCdTe (215 ns) is different from that of CdTe QD (65 ns), indicating that the processes are different.

When the AgPT-nCdTe hybrid sample is excited at 550 nm, charge carriers are still excited in CdTe QDs, and simultaneously LSPR of Ag PT is also excited. Such simultaneous excitation can lead to mainly three different processes, which are as follows. First the excitation of LSPR will result in enhancement of local field increasing the excited carrier density in the CdTe QD[167, 168]. Secondly, the plasmon can relax by exciting carriers in CdTe QD, leading to PIRET[169, 170]. Third, the hot electrons that are formed after plasmon relaxation can also get transferred to CdTe QD in subpicosecond time scale[164]. All these three processes will result in a strong increase in the excited carrier density in CdTe QD. Such an increase in the density of carriers will actively facilitate an increase in non-radiative relaxations like, increasing the A_1. An increase in the non-radiative process will always reduce the strength of radiative recombinations, A_2 and A_3. This explains all the changes observed in the experiment when excited at 550 nm (Table-6.1). Consequently, the

PL from AgPT-nCdTe quenches when compared to CdTe QDs. Thus, we see that the excitation wavelength with respect to the overlapped emission spectrum and LSPR absorption could alter the PL kinetics drastically in Ag-CdTe HNS unlike to the case where these two would not overlap (Ag-CdTe hybrid in chapter 5) and always lead to overall quenching of PL.

6.6 Summary

Attaching CdTe QDs to Ag PT brings about strong changes in its static and dynamical optical response. Using the experimental linear optical response and numerical calculations, we have shown that the change in static optical response is brought about mainly by the change in the dielectric constant surrounding the Ag PT. The change in transient absorption signal is brought about by the attachment of CdTe QDs on Ag PT could not be explained simply by the change in the temperature of free electrons in Ag PT alone. It turns out that the presence of CdTe QDs does not allow the temperature of free electrons to rise beyond certain threshold. We have shown that change in the number density of free electrons in metal also would contribute to the change in transient absorption signal. We have also shown how this additional change in transient absorption can be used for estimating the number of electrons hopping from the metal nanoparticle to the semiconductor QDs attached to it. Similar estimate is also possible in samples where electrons are transported from the attached species to metal. In such cases the number density of free electrons in metal would increase resulting in a shift which is opposite to that observed here. Method to estimate the number of electrons getting transported at ultrafast time scales would provide a way to optimize the design of a metal-semiconductor hybrid system for charge transport applications like light harvesting, catalysis, light-controlled surface plasmon polariton switch etc. We have also studied radiative properties of similar HNS and found that PL kinetics in AgPT-CdTe hybrids was drastically altered by selective excitation. Excitation of a hybrid system well above an overlapped emission (of SQD) and LSPR (of MNP) could effectively suppress the non-radiative recombination while exciting right at the overlapped spectral regime enhances the non-radiative recombination. It opens up possibility of designing a material with suitable PL kinetics that is well suited for light-emitting devices

Bibliography

[1] Sander F Wuister, Floris Van Driel, and Andries Meijerink. "Luminescence of CdTe nanocrystals". In: *J. Lumin.* 102 (2003), pp. 327–332.

[2] Yury Rakovich et al. "Size-selective photoluminescence excitation spectroscopy in CdTe quantum dots". In: *Opto-Ireland 2002: Optics and Photonics Technologies and Applications*. Vol. 4876. International Society for Optics and Photonics. SPIE, 2003, pp. 432 –437.

[3] Jia Guo, Wuli Yang, and Changchun Wang. "Systematic Study of the Photoluminescence Dependence of Thiol-Capped CdTe Nanocrystals on the Reaction Conditions". In: *J. Phys. Chem. B* 109 (2005), pp. 17467–17473.

[4] S. Maier. *Plasmonics:Fundamentals and Applications*. Springer, 2007.

[5] Weiyang Li et al. "Dimers of silver nanospheres: facile synthesis and their use as hot spots for surface-enhanced Raman scattering". In: *Nano Lett.* 9.1 (2008), pp. 485–490.

[6] Pedro HC Camargo et al. "Measuring the SERS enhancement factors of dimers with different structures constructed from silver nanocubes". In: *Chem. Phys. Lett.* 484.4-6 (2010), pp. 304–308.

[7] Darya Radziuk and Helmuth Moehwald. "Prospects for plasmonic hot spots in single molecule SERS towards the chemical imaging of live cells". In: *Phys. Chem. Chem. Phys.* 17.33 (2015), pp. 21072–21093.

[8] Harry A Atwater and Albert Polman. "Plasmonics for improved photovoltaic devices". In: *Materials For Sustainable Energy: A Collection of Peer-Reviewed Research and Review Articles from Nature Publishing Group*. World Scientific, 2011, pp. 1–11.

[9] Alexander O. Govorov et al. "Exciton-Plasmon Interaction and Hybrid Excitons in Semiconductor-Metal Nanoparticle Assemblies". In: *Nano Letters* 6 (2006), pp. 984–994.

[10] Krishna Kanta Haldar, Tapasi Sen, and Amitava Patra. "Metal Conjugated Semiconductor Hybrid Nanoparticle-Based Fluorescence Resonance Energy Transfer". In: *J. Phys. Chem. C* 114 (2010), 4869–4874.

[11] Lamia Nahar et al. "Metal-Semiconductor Hybrid Aerogels:Evolution of Optoelectroni Properties in a Low Dimensional CdSe/Ag Nanoparticle Assembly". In: *ACS Nano* 9 (2015), 9810–9821.

[12] Parinda Vasa and Christoph Lienau. "Strong light–matter interaction in quantum emitter/metal hybrid nanostructures". In: *Acs Photonics* 5.1 (2017), pp. 2–23.

[13] Krishna Kanta Haldar et al. “Photophysical Properties of Au-CdTe Hybrid Nanostructures of Varying Sizes and Shapes”. In: *ChemPhysChem* 13.17 (2012), pp. 3989–3996.

[14] M. Haridas et al. “Photoluminescence spectroscopy and lifetime measurements from self-assembled semiconductor-metal nanoparticle hybrid arrays”. In: *Applied Physics Letters* 97.8 (2010), p. 083307.

[15] Yannick Salamin et al. “100 GHz Plasmonic Photodetector”. In: *ACS Photonics* 5.8 (2018), pp. 3291–3297.

[16] Harry A. Atwater and Albert Polman. “Plasmonics for improved photovoltaic devices”. In: *Nature Material* 9 (2010), 205–213.

[17] Ruibin et al. “Metal/Semiconductor Hybrid Nanostructures for Plasmon-Enhanced Applications”. In: *Advanced Materials* 26 (2014), pp. 5274–5309.

[18] Wan Ki Bae, Sergio Brovelli, and Victor I. Klimov. “Spectroscopic insights into the performance of quantum dot light-emitting diodes”. In: *MRS Bulletin* 38.9 (2013), 721–730.

[19] Scott K. Cushing et al. “Controlling Plasmon-Induced Resonance Energy Transfer and Hot Electron Injection Processes in Metal@TiO2 Core–Shell Nanoparticles”. In: *The Journal of Physical Chemistry C* 119.28 (2015), pp. 16239–16244.

[20] Navendu Mondal and Anunay Samanta. “Ultrafast Charge Transfer and Trapping Dynamics in a Colloidal Mixture of Similarly Charged CdTe Quantum Dots and Silver Nanoparticles”. In: *J. Phys. Chem. C* 120 (2016), pp. 650–658.

[21] KR Catchpole and Albert Polman. “Plasmonic solar cells”. In: *Opt. Express* 16.26 (2008), pp. 21793–21800.

[22] Scott K Cushing and Nianqiang Wu. “Plasmon-enhanced solar energy harvesting”. In: *Electrochem. Soc. Interface* 22.2 (2013), pp. 63–67.

[23] Wenguang Fan and Michael KH Leung. “Recent development of plasmonic resonance-based photocatalysis and photovoltaics for solar utilization”. In: *Molecules* 21.2 (2016), p. 180.

[24] Gabriel Lozano et al. “Metallic nanostructures for efficient LED lighting”. In: *Light: Science & Applications* 5.6 (2016), e16080.

[25] Liang Ma et al. “Improved Hydrogen Production of Au–Pt–CdS Hetero- Nanostructures by Efficient Plasmon-Induced Multipathway Electron Transfer”. In: *Advanced Functional Materials* 26.33 (2016), pp. 6076–6083.

[26] Zhijie Wang et al. “Manipulation of charge transfer and transport in plasmonic-ferroelectric hybrids for photoelectrochemical applications”. In: *Nature communications* 7 (2016), p. 10348.

[27] Sun Mi Kim et al. “The effect of hot electrons and surface plasmons on heterogeneous catalysis”. In: *Journal of Physics: Condensed Matter* 28.25 (2016), p. 254002.

[28] Elad Eizner et al. “Aluminum nanoantenna complexes for strong coupling between excitons and localized surface plasmons”. In: *Nano letters* 15.9 (2015), pp. 6215–6221.

[29] Alejandro Manjavacas, Francisco Javier Garcia de Abajo, and Peter Nordlander. "Quantum plexcitonics: strongly interacting plasmons and excitons". In: *Nano Lett.* 11.6 (2011), pp. 2318–2323.

[30] Tian Li et al. "Solar hydrogen generation by a CdS-Au-TiO2 sandwich nanorod array enhanced with Au nanoparticle as electron relay and plasmonic photosensitizer". In: *Journal of the American Chemical Society* 136.23 (2014), pp. 8438–8449.

[31] C. F. Bohren and Donald R. Huffman. *Absorption and Scattering of Light by Small Particles*. New York: John Wiley & Sons, 1983.

[32] K Lance Kelly et al. "The optical properties of metal nanoparticles: the influence of size, shape, and dielectric environment". In: *J. Phys. Chem. B* 107 (2003), pp. 668–677.

[33] Jack J Mock, David R Smith, and Sheldon Schultz. "Local refractive index dependence of plasmon resonance spectra from individual nanoparticles". In: *Nano Lett.* 3.4 (2003), pp. 485–491.

[34] Ronald Fuch. "Theory of the optical properties of ionic crystal cubes". In: *Phys. Rev. B* 11 (1975), pp. 1732–1740.

[35] B. K. Russell et al. "Experimental test of the Mie theory for microlithographically produced silver spheres". In: *Phys. Rev. B* 35 (1987), pp. 2151–2154.

[36] J Jayabalan. "Ultrafast third-order nonlinearity of silver nanospheres and nanodiscs". In: *Nanotechnology* 18 (2007), p. 31.

[37] Olivier J. F. Martin. "Plasmon resonances in nanowires with a non-regular cross section". In: *Optical Nanotechnologies - The Manipulation of Surface and Local Plasmons*. Ed. by J.Tominaga and D.P.Tsai. 1^{st}. Heidelberg: Springer, 2002. Chap. 13, pp. 203–228.

[38] Ari Sihvola. *Electromagnetic mixing formulas and applications*. Ed. by Ari Sihvola. London : Institution of Electrical Engineers, 1999.

[39] P. B. Johnson and R. W. Christy. "Optical Constants of the Noble Metals". In: *Phys. Rev. B* 6 (1972), pp. 4370–4379.

[40] Palash Bharadwaj, Pascal Anger, and Lukas Novotny. "Nanoplasmonic enhancement of single-molecule fluorescence". In: *Nanotechnology* 18.4 (2006), p. 044017.

[41] M Futamata, Y Maruyama, and M Ishikawa. "Local electric field and scattering cross section of Ag nanoparticles under surface plasmon resonance by finite difference time domain method". In: *J. Phys. Chem. B* 107.31 (2003), pp. 7607–7617.

[42] Katsuaki Tanabe. "Field Enhancement around Metal Nanoparticles and Nanoshells: A Systematic Investigation". In: *The Journal of Physical Chemistry C* 112.40 (2008), pp. 15721–15728.

[43] Julia A Ruemmele et al. "A localized surface plasmon resonance imaging instrument for multiplexed biosensing". In: *Anal. Chem.* 85.9 (2013), pp. 4560–4566.

[44] Yinghui Sun et al. “Non-symmetric hybrids of noble metal-semiconductor: Interplay of nanoparticles and nanostructures in formation dynamics and plasmonic applications”. In: *Prog. Mater Sci.: Materials International* 27.2 (2017), pp. 157–168.

[45] Heesang Ahn et al. “A localized surface plasmon resonance sensor using double-metal-complex nanostructures and a review of recent approaches”. In: *Sensors* 18.1 (2018), p. 98.

[46] Wen Xu et al. “A novel strategy for improving upconversion luminescence of NaYF4:Yb, Er nanocrystals by coupling with hybrids of silver plasmon nanostructures and poly(methyl methacrylate) photonic crystals”. In: *Nano Research* 6.11 (2013), pp. 795–807. ISSN: 1998-0000.

[47] Rohit Chikkaraddy et al. “Single-molecule strong coupling at room temperature in plasmonic nanocavities”. In: *Nature* 535.7610 (2016), pp. 127–130.

[48] Simon F. Becker et al. “Gap-Plasmon-Enhanced Nanofocusing Near-Field Microscopy”. In: *ACS Photonics* 3.2 (2016), pp. 223–232.

[49] Hongxing Xu et al. “Spectroscopy of single hemoglobin molecules by surface enhanced Raman scattering”. In: *Physical review letters* 83.21 (1999), p. 4357.

[50] Hongxing Xu et al. “Electromagnetic contributions to single-molecule sensitivity in surface-enhanced Raman scattering”. In: *Physical Review E* 62.3 (2000), p. 4318.

[51] Encai Hao and George C Schatz. “Electromagnetic fields around silver nanoparticles and dimers”. In: *J. Chem. Phys.* 120.1 (2004), pp. 357–366.

[52] Eleonora Petryayeva and Ulrich J Krull. “Localized surface plasmon resonance: Nanostructures, bioassays and biosensing—A review”. In: *Anal. Chim. Acta* 706.1 (2011), pp. 8–24.

[53] Charles Kittel. *Introduction to Solid State Physics*. 7^{th}. New York: John Wiley & Sons, Inc., 2004.

[54] Yun Tang and Min Ouyang. “Tailoring properties and functionalities of metal nanoparticles through crystallinity engineering”. In: *Nat. Mater.* 6.10 (2007), p. 754.

[55] Rolf Koole. “Nanoparticles Workhorses of Nanoscience”. In: ed. by Celso (Ed.) de Mello Donega. Springer, 2014. Chap. 2, pp. 13–51.

[56] Proefschrift. “Optical Properties of Semiconductor Quantum Dots”. PhD thesis. University of Pisa, Itali, 2011.

[57] A.A. Rajabi H. Hassanabadi. “Energy levels of a spherical quantum dot in a confining potential”. In: *Physics Letters A* 373 (2009), pp. 679–681.

[58] W Y Liang. “Excitons”. In: *Phys. Educ. 5, 226* 5 (2016), pp. 226–228.

[59] Jasprit singh. *Electronic and Optoelectronic Properties of Semiconductor Structures*. 1st. Cambridge University press, 2007.

[60] Ehud Shaviv et al. “Absorption Properties of Metal–Semiconductor Hybrid Nanoparticles”. In: *ACS Nano* 5.6 (2011), pp. 4712–4719.

[61] Yong Yanga and Masayuki Nogami. "Ultrafast electron dynamics and enhanced optical nonlinearities of CdS-capped AuBaTiO$_3 composite film$". In: *Journal of Applied Physics* 98 (2005), p. 033528.

[62] Koshin Hosoki et al. "Direct and Stepwise Energy Transfer from Excitons to Plasmons in Close-Packed Metal and Semiconductor Nanoparticle Monolayer Films". In: *Phys. Rev. Lett.* 100 (20 2008), p. 207404.

[63] Kaifeng Wu et al. "Efficient hot-electron transfer by a plasmon-induced interfacial charge-transfer transition". In: *Science* 349.6248 (2015), pp. 632–635.

[64] Bumsu Lee et al. "Fano Resonance and Spectrally Modified Photoluminescence Enhancement in Monolayer MoS2 Integrated with Plasmonic Nanoantenna Array". In: *Nano Letters* 15.5 (2015), pp. 3646–3653.

[65] Alexander O. Govorov et al. "ExcitonPlasmon Interaction and Hybrid Excitons in SemiconductorMetal Nanoparticle Assemblies". In: *Nano Letters* 6.5 (2006), pp. 984–994.

[66] DaeGwi Kim et al. "Precise control of photoluminescence enhancement and quenching of semiconductor quantum dots using localized surface plasmons in metal nanoparticles". In: *Journal of Applied Physics* 114.15 (2013), p. 154307.

[67] Yuval Ben-Shahar et al. "Optimal metal domain size for photocatalysis with hybrid semiconductor-metal nanorods". In: *Nature Communications* 7.1 (2016), p. 10413.

[68] Michael Volokh and Taleb Mokari. "Metal/semiconductor interfaces in nanoscale objects: synthesis, emerging properties and applications of hybrid nanostructures". In: *Nanoscale Adv.* 2 (2020), pp. 930–961.

[69] Jin Chang et al. "Ligand-dependent exciton dynamics and photovoltaic properties of PbS quantum dot heterojunction solar cells". In: *Phys. Chem. Chem. Phys.* 19.9 (2017), pp. 6358–6367.

[70] Christian Strelow et al. "Metal-Semiconductor Nanoparticle Hybrid Formed by Self-Organization:A Platform to Address Exciton-Plasmon Coupling". In: *Nano Letters* 16 (2016), 4811–4818.

[71] Shane A Gallagher et al. "Efficient quenching of TGA-capped CdTe quantum dot emission by a surface-coordinated europium (III) cyclen complex". In: *Inorg. Chem.* 52.8 (2013), pp. 4133–4135.

[72] Yi Luo and Jing Zhao. "Plasmon-exciton interaction in colloidally fabricated metal nanoparticle-quantum emitter nanostructures". In: *Nano Research* 12.9 (2019), pp. 2164–2171. ISSN: 1998-0000.

[73] Buil S Quelin X Hermier JP Dubertret B. Mahler B Spinicelli P. "Towards non-blinking colloidal quantum dots". In: *Nat Mater* 7.8 (2008), pp. 659–664.

[74] Dhananjay Bodas and Chantal Khan-Malek. "Direct patterning of quantum dots on structured PDMS surface". In: *Sensors and Actuators B: Chemical* 128.1 (2007), pp. 168–172. ISSN: 0925-4005.

[75] Yanfei Wang et al. "Optical properties of Ag/CdTe nanocomposite self-organized by electrostatic interaction". In: *Spectrochim. Acta, Part A* 64.1 (2006), pp. 101–105.

[76] A.E. Ragab et al. "Ag surface plasmon enhances luminescence of CdTe QDs". In: *Optics Communications* 314 (2014), pp. 86–89.

[77] Alberto Naldoni et al. "Pt and Au/TiO2 photocatalysts for methanol reforming: Role of metal nanoparticles in tuning charge trapping properties and photoefficiency". In: *Applied Catalysis B: Environmental* 130-131 (2013), pp. 239 –248.

[78] Zibin Hai et al. "Modification of TiO2 by bimetallic Au–Cu nanoparticles for wastewater treatment". In: *J. Mater. Chem. A* 1 (36 2013), pp. 10829–10835.

[79] K. Wu et al. "Efficient hot-electron transfer by a plasmon-induced interfacial charge-transfer transition". In: *Science* 349.6248 (2015), pp. 632–635.

[80] Ying Yu et al. "Ultrafast plasmonic hot electron transfer in Au nanoantenna/MoS2 heterostructures". In: *Advanced Functional Materials* 26.35 (2016), pp. 6394–6401.

[81] Pyng Yu et al. "Photoinduced ultrafast charge separation in plexcitonic CdSe/Au and CdSe/Pt nanorods". In: *The Journal of Physical Chemistry Letters* 4.21 (2013), pp. 3596–3601.

[82] Navendu Mondal, Sneha Paul, and Anunay Samanta. "Photoinduced 2-way electron transfer in composites of metal nanoclusters and semiconductor quantum dots". In: *Nanoscale* 8 (2016), pp. 14250–14256.

[83] Jayanta Dana, Partha Maity, and Hirendra N Ghosh. "Hot-electron transfer from the semiconductor domain to the metal domain in CdSe@ CdS {Au} nano-heterostructures". In: *Nanoscale* 9.27 (2017), pp. 9723–9731.

[84] Kong-Thon Tsen. *Non-equilibrium dynamics of semiconductors and nanostructures*. CRC Press, 2005.

[85] J Jayabalan. "Origin and time dependence of higher-order nonlinearities in metal nanocomposites". In: *J. Opt. Soc. Am. B* 28.10 (2011), pp. 2448–2455.

[86] Christopher R. Carey et al. "Ultrafast Transient Absorption Measurements of Charge Carrier Dynamics in Single IIVI Nanowires". In: *The Journal of Physical Chemistry C* 113.44 (2009), pp. 19077–19081.

[87] Pierre Viste et al. "Enhancement and Quenching Regimes in MetalSemiconductor Hybrid Optical Nanosources". In: *ACS Nano* 4.2 (2010), pp. 759–764.

[88] A. N. Emam et al. "Enhancement of the Collective Optical Properties of Plasmonic Hybrid Carbon Dots via Localized Surface Plasmon". In: *Journal of Luminescence* 200 (2018), pp. 287 –297. ISSN: 0022-2313.

[89] Sabina Gurung et al. "The optical response of self-organized Ag-CdTe metal-semiconductor hybrid nanostructures: Change in interaction vs number density variation". In: *J. Appl. Phys.* 124.20 (2018), p. 204305.

[90] Richard Wargnier et al. “Energy Transfer in Aqueous Solutions of Oppositely Charged CdSe/ZnS Core/Shell Quantum Dots and in Quantum Dot-Nanogold Assemblies”. In: *Nano Lett.* 4.3 (2004), pp. 4451–457.

[91] Ming Li et al. “Size-Dependent Energy Transfer between CdSe/ZnS Quantum Dots and Gold Nanoparticles”. In: *J.Phys.Chem.Lett.* 2.17 (2011), pp. 2125–2129.

[92] Yoshihiko Kanemitsu and Kazunari Matsuda. “Energy transfer between excitons and plasmons in semiconductor–metal hybrid nanostructures”. In: *Journal of Luminescence* 131.3 (2011), pp. 510 –514.

[93] Jamuna K Vaishnav and Tushar Kanti Mukherjee. “Long-Range Resonance Coupling-Induced Surface Energy Transfer from CdTe Quantum Dot to Plasmonic Nanoparticle”. In: *J. Phys. Chem. C* 122.49 (2018), pp. 28324–28336.

[94] Mani Prabha Singh and Geoffrey F. Strouse. “Involvement of the LSPR Spectral Overlap for Energy Transfer between a Dye and Au Nanoparticle”. In: *Journal of the American Chemical Society* 132.27 (2010), pp. 9383–9391.

[95] GUSTAV MIE. “Contributions to the optics of turbid media, particularly colloidal metal suspensions”. In: *Annalen der Physik* 25 (1908), pp. 377–445.

[96] Rongchao Jin et al. “Photoinduced conversion of silver nanospheres to nanoprisms”. In: *Science* 294.5548 (2001), pp. 1901–1903.

[97] Gabriella S Métraux and Chad A Mirkin. “Rapid thermal synthesis of silver nanoprisms with chemically tailorable thickness”. In: *Advanced Materials* 17.4 (2005), pp. 412–415.

[98] P. Eaton et al. “A direct comparison of experimental methods to measure dimensions of synthetic nanoparticles”. In: *Ultramicroscopy* 182 (2017), pp. 179–190. ISSN: 0304-3991. DOI: `https://doi.org/10.1016/j.ultramic.2017.07.001`. URL: `https://www.sciencedirect.com/science/article/pii/S0304399116302091`.

[99] Challa S.S.R. Kumar, ed. *UV-VIS and Photoluminescence Spectroscopy for Nanomaterials Characterization*. Springer, Berlin, Heidelberg, 2013.

[100] Joel Yuen-Zhou et al. “Conclusions”. In: *Ultrafast Spectroscopy*. 2053-2563. IOP Publishing, 2014, 7–1 to 7–2.

[101] Durga Prasad Khatua et al. “Filtering noise in time and frequency domain for ultrafast pump–probe performed using low repetition rate lasers”. In: *Review of Scientific Instruments* 91.10 (2020), p. 103901.

[102] Marcelo Alves-Santos, Rosa Di Felice, and Guido Goldoni. “Dielectric functions of semiconductor nanoparticles from the optical absorption spectrum: the case of CdSe and CdS”. In: *J. Phys. Chem. C* 114.9 (2010), pp. 3776–3780.

[103] MI Mishchenko. “Light scattering by randomly oriented axially symmetric particles”. In: *J. Opt. Soc. Am. A* 8.6 (1991), pp. 871–882.

[104] Daniel W Mackowski and Michael I Mishchenko. “Calculation of the T matrix and the scattering matrix for ensembles of spheres”. In: *J. Opt. Soc. Am. A* 13.11 (1996), pp. 2266–2278.

[105] C. R. Purcell E.M. & Pennypacker. “Scattering and Absorption of light by Nonspherical Dielectric Grains”. In: *Astrophys. J.* 186 (1973), pp. 705–714.

[106] David Paramelle et al. “A rapid method to estimate the concentration of citrate capped silver nanoparticles from UV-visible light spectra”. In: *Analyst* 139.19 (2014), pp. 4855–4861.

[107] W William Yu et al. “Experimental determination of the extinction coefficient of CdTe, CdSe, and CdS nanocrystals”. In: *Chem. Mater.* 15.14 (2003), pp. 2854–2860.

[108] Matthew R. Libera and Ray F. Egerton. “Advances in the Transmission Electron Microscopy of Polymers”. In: *Polymer Reviews* 50.3 (2010), pp. 321–339.

[109] A. H. Tsou and D. G. Yablon. *Scanning Probe Microscopy in Industrial Applications: Nanomechanical Characterization*. Wiley Online Library, 2013.

[110] Abhijit Mandal and Naoto Tamai. “Influence of Acid on Luminescence Properties of Thioglycolic Acid-Capped CdTe Quantum Dots”. In: *J. Phys. Chem. C* 112 (2008), pp. 8244–8250.

[111] Wei Chen, Alan G Joly, and David E McCready. “Upconversion luminescence from CdSe nanoparticles”. In: *J. Chem. Phys.* 122.22 (2005), p. 224708.

[112] Muthu Irulappan Sriram et al. “Antitumor activity of silver nanoparticles in Dalton’s lymphoma ascites tumor model”. In: *Int J Nanomedicine* 5 (2010), 753–762.

[113] J Jayabalan et al. “Aggregated nanoplatelets: optical properties and optically induced deaggregation”. In: *J. Phys. Condens. Matter* 20.44 (2008), p. 445222.

[114] Hafiz HM Salih et al. “Removal of Stabilized Silver Nanoparticles from Surface Water by Conventional Treatment Processes”. In: *Advances in Nanoparticles* 8 (2019), pp. 21–35.

[115] P. B. Johnson and R. W. Christy. “Optical constants of the noble metals”. In: *Phys. Rev. B* 6.12 (1972), p. 4370.

[116] L Genzel, TP Martin, and U Kreibig. “Dielectric function and plasma resonances of small metal particles”. In: *Z. Phys. B: Condens. Matter* 21.4 (1975), pp. 339–346.

[117] Kevin G Stamplecoskie and Juan C Scaiano. “Kinetics of the formation of silver dimers: early stages in the formation of silver nanoparticles”. In: *J. Am. Chem. Soc.* 133.11 (2011), pp. 3913–3920.

[118] Michael Grouchko et al. “Conductive inks with a “built-in” mechanism that enables sintering at room temperature”. In: *ACS Nano* 5.4 (2011), pp. 3354–3359.

[119] Michael Grouchko et al. “Merging of metal nanoparticles driven by selective wettability of silver nanostructures”. In: *Nat. Commun.* 5 (2014), p. 2994.

[120] Naomi J. Halas et al. “Plasmons in Strongly Coupled Metallic Nanostructures”. In: *Chemical Reviews* 111.6 (2011), pp. 3913–3961.

[121] Pascale Mariano et al. “Full-wave electromagnetic modes and hybridization in nanoparticle dimers”. In: *Scientific Reports* 9 (2019), p. 14524.

[122] Cyril Guillon et al. “Ultrafast surface plasmon resonance Landau damping and electron kinetics in metal nanoparticles”. In: *Ultrafast Phenomena in Semiconductors and Nanostructure Materials VIII* 5352 (2004), pp. 65–76.

[123] N Del Fatti et al. “Nonequilibrium electron dynamics in noble metals”. In: *Phys. Rev. B* 61.24 (2000), p. 16956.

[124] J-Y Bigot et al. “Electron dynamics in metallic nanoparticles”. In: *Chem. Phys.* 251.1-3 (2000), pp. 181–203.

[125] M Perner et al. “Observation of hot-electron pressure in the vibration dynamics of metal nanoparticles”. In: *Phys. Rev. Lett.* 85.4 (2000), p. 792.

[126] Rodrigo Sato et al. “Experimental investigation of nonlinear optical properties of Ag nanoparticles: Effects of size quantization”. In: *Phys. Rev. B* 90.12 (2014), p. 125417.

[127] Prashant K Jain, Wei Qian, and Mostafa A El-Sayed. “Ultrafast electron relaxation dynamics in coupled metal nanoparticles in aggregates”. In: *J. Phys. Chem. B* 110.1 (2006), pp. 136–142.

[128] Mark J Feldstein et al. “Electronic relaxation dynamics in coupled metal nanoparticles”. In: *J. Am. Chem. Soc.* 119.28 (1997), pp. 6638–6647.

[129] Xiu-Chun Yang et al. “Effects of thermal treatment on the third-order optical nonlinearity and ultrafast dynamics of Ag nanoparticles embedded in silicate glasses”. In: *Chem. Phys. Lett.* 475.4-6 (2009), pp. 256–259.

[130] Kaifeng Wu et al. “Efficient hot-electron transfer by a plasmon-induced interfacial charge-transfer transition”. In: *Science* 349.6248 (2015), pp. 632–635.

[131] Akihiro Furube and Shuichi Hashimoto. “Insight into plasmonic hot-electron transfer and plasmon molecular drive: new dimensions in energy conversion and nanofabrication”. In: *NPG Asia Materials* 9.12 (2017), e454.

[132] Bo Gao et al. “Charge transfer and retention in directly coupled Au-CdSe nanohybrids”. In: *Nano Research* 5.2 (2012), pp. 88–98. ISSN: 1998-0000.

[133] Yuxin Tang et al. “Efficient Ag@AgCl cubic cage photocatalysts profit from ultrafast plasmon-induced electron transfer processes”. In: *Adv. Funct. Mater.* 23.23 (2013), pp. 2932–2940.

[134] AE Ragab et al. “Photoluminescence and upconversion on Ag/CdTe quantum dots”. In: *Optics & Laser Technology* 63 (2014), pp. 8–12.

[135] Zhenfeng Bian et al. “Au/TiO_2 superstructure-based plasmonic photocatalysts exhibiting efficient charge separation and unprecedented activity”. In: *J. Am. Chem. Soc.* 136.1 (2013), pp. 458–465.

[136] Eva-Maria Roller et al. “Hotspot-mediated non-dissipative and ultrafast plasmon passage”. In: *Nat. Phys.* 13.8 (2017), p. 761.

[137] Yun-Sheng Xia, Chun Cao, and Chang-Qing Zhu. “Two distinct photoluminescence responses of CdTe quantum dots to Ag (I)”. In: *Journal of Luminescence* 128.1 (2008), pp. 166 –172.

[138] L. M. An et al. “Enhanced Fluorescence from CdTe Quantum Dots Self-Assembled on the Surface of Silver Nanoparticles”. In: *Journal of Nanoscience and Nanotechnology* 10.3 (2010), pp. 2099–2103.

[139] Eyal Cohen-Hoshen et al. “Exciton–plasmon interactions in quantum dot–gold nanoparticle structures”. In: *Nano Lett.* 12.8 (2012), pp. 4260–4264.

[140] Sreejith Kaniyankandy et al. “Charge carrier dynamics in thiol capped CdTe quantum dots”. In: *Phys. Chem. Chem. Phys.* 12 (16 2010), pp. 4210–4216.

[141] Sachin Rawalekar et al. “Ultrafast Charge Carrier Relaxation and Charge Transfer Dynamics of CdTe/CdS CoreShell Quantum Dots as Studied by Femtosecond Transient Absorption Spectroscopy”. In: *The Journal of Physical Chemistry C* 114.3 (2010), pp. 1460–1466.

[142] Andrey L. Rogach et al. “Aqueous Synthesis of Thiol-Capped CdTe Nanocrystals: State-of-the-Art”. In: *The Journal of Physical Chemistry C* 111.40 (2007), pp. 14628–14637.

[143] Xiaoyong Wang et al. “Surface-Related Emission in Highly Luminescent CdSe Quantum Dots”. In: *Nano Letters* 3.8 (2003), pp. 1103–1106.

[144] Daniel Espinobarro-Velazquez et al. “Effect of Chloride Passivation on Recombination Dynamics in CdTe Colloidal Quantum Dots”. In: *ChemPhysChem* 16.6 (2015), pp. 1239–1244.

[145] Swayandipta Dey et al. “Excitation wavelength dependent photon anti-bunching/bunching from single quantum dots near gold nanostructures”. In: *Nanoscale* 10 (3 2018), pp. 1038–1046.

[146] Gabriel Sagarzazu et al. “Auger recombination dynamics in hybrid silica-coated CdTe nanocrystals”. In: *Phys. Chem. Chem. Phys.* 13 (8 2011), pp. 3227–3230.

[147] Yoichi Kobayashi et al. “Effect of Surface Defects on Auger Recombination in Colloidal CdS Quantum Dots”. In: *The Journal of Physical Chemistry Letters* 2.9 (2011), pp. 1051–1055.

[148] Simon C. Boehme et al. “Density of Trap States and Auger-mediated Electron Trapping in CdTe Quantum-Dot Solids”. In: *Nano Letters* 15.5 (2015), pp. 3056–3066.

[149] Xiaoyong Wang et al. “Photoluminescence upconversion in colloidal CdTe quantum dots”. In: *Phys. Rev. B* 68 (12 2003), p. 125318.

[150] Stefano Giordano and Walter Rocchia. “Shape-dependent effects of dielectrically nonlinear inclusions in heterogeneous media”. In: *J. Appl. Phys.* 98 (2005), p. 104101.

[151] D. Ricard, Ph. Roussignol, and Chr. Flytzanis. “Surface-mediated enhancement of optical phase conjugation in metal colloids”. In: *Opt. Lett.* 10 (1985), pp. 511–513.

[152] J. Jayabalan, Asha Singh, and Rama Chari. “Effect of edge smoothening on the extinction spectra of metal nanoparticles”. In: *Applied Physics Letters* 97.4 (2010), p. 041904.

[153] Xiaotong Liu et al. "Tunable dipole surface plasmon resonances of silver nanoparticles by cladding dielectric layers". In: *Scientific reports* 5 (2015), p. 12555.

[154] Bruce T. Draine and Piotr J. Flatau. "Discrete-dipole appriximation for scattering calculations". In: *J. Opt. Soc. Am. A* 11 (1994), pp. 1491–1499.

[155] Bruce T. Draine and Piotr J. Flatau. *User Guide for the Discrete Dipole Approximation Code DDSCAT (Version 7.3)*. http://arxiv.org/abs/astro-ph/0409262.

[156] N Del Fatti et al. "Non-equilibrium electron dynamics in noble metals". In: *Phys. Rev. B* 61 (2000), pp. 16956–16966.

[157] Christophe Voisin, Natalia Del Fatti andâ€ Dimitris Christofilos, and Fabrice VallÃ©e. "Ultrafast Electron Dynamics and Optical Nonlinearities in Metal Nanoparticles". In: *J Phys. Chem. B* 105.12 (2001), pp. 2264–2280.

[158] Fabrice Vallee. "Non-Equilibrium Dynamics of Semiconductors and Nanostructures". In: ed. by Kong-Thon Tsen. CRC Press: New York, 2005. Chap. 5, pp. 101–142.

[159] Christophe Bauer et al. "Ultrafast chemical interface scattering as an additional decay channel for nascent nonthermal electrons in small metal nanoparticles". In: *The Journal of chemical physics* 120.19 (2004), pp. 9302–9315.

[160] John B Pendry et al. "Extremely low frequency plasmons in metallic mesostructures". In: *Physical review letters* 76.25 (1996), p. 4773.

[161] Richard A Shelby, David R Smith, and Seldon Schultz. "Experimental verification of a negative index of refraction". In: *science* 292.5514 (2001), pp. 77–79.

[162] Hari P Paudel and Michael N Leuenberger. "Light-controlled plasmon switching using hybrid metal-semiconductor nanostructures". In: *Nano letters* 12.6 (2012), pp. 2690–2696.

[163] Terianna J. Wax et al. "Excitation Wavelength-Dependent Photoluminescence Decay of Hybrid Gold/Quantum Dot Nanostructures". In: *ACS Omega* 3.10 (2018), pp. 14151–14156.

[164] Asha Singh et al. "Counting the Electrons Hopping in Ultrafast Time Scales in an Ag-CdTe Hybrid Nanostructure". In: *J. Phys. Chem. C* 123 (2019), pp. 28584–28592.

[165] M. Haridas et al. "Photoluminescence decay rate engineering of CdSe quantum dots in ensemble arrays embedded with gold nano-antennae". In: *Journal of Applied Physics* 114.6 (2013), p. 064305.

[166] A. Kucherik et al. "Nano-Antennas Based on Silicon-Gold Nanostructures". In: *Scientific Reports* 9 (2019), p. 338.

[167] Sharonda J. LeBlanc et al. "Enhancement of Multiphoton Emission from Single CdSe Quantum Dots Coupled to Gold Films". In: *Nano Letters* 13.4 (2013), pp. 1662–1669.

[168] Hiroyuki Naiki et al. "Single-Photon Emission Behavior of Isolated CdSe/ZnS Quantum Dots Interacting with the Localized Surface Plasmon Resonance of Silver Nanoparticles". In: *The Journal of Physical Chemistry C* 115.47 (2011), pp. 23299–23304.

[169] Monica Focsan et al. "Controlling the Luminescence of Carboxyl-Functionalized CdSe/ZnS Core–Shell Quantum Dots in Solution by Binding with Gold Nanorods". In: *The Journal of Physical Chemistry C* 118.43 (2014), pp. 25190–25199.

[170] Swayandipta Dey et al. "An experimental and theoretical mechanistic study of biexciton quantum yield enhancement in single quantum dots near gold nanoparticles". In: *Nanoscale* 7 (15 2015), pp. 6851–6858.

Thesis Highlight

Name of the Student: Sabina Gurung
Name of the CI/OCC: Raja Ramanna Centre for Advanced Technology, Indore
Enrolment No.: PHYS03201504003
Thesis Title: Static and Ultrafast Optical Response of Metal-Semiconductor Hybrid Nanostructures
Discipline: Physical Sciences **Sub-Area of Discipline:** Nanoscience
Date of viva voce:

Metal-semiconductor hybrid nanostructure (HNS) is an emerging paradigm for construction of advanced materials having multiple functionalities that are derived from synergistic interactions between metal nanoparticles (MNPs) and semiconductor quantum dots (SQDs). Appropriately designed HNS materials can show better performance as sensors, energy harvesters, efficient emitters and as better photocatalyst.

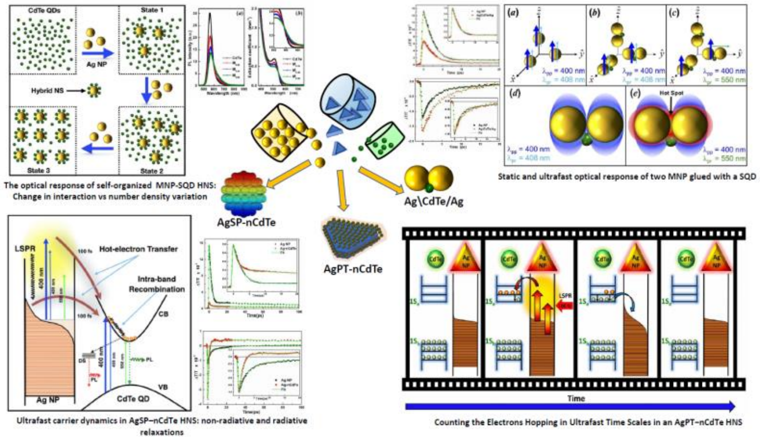

Figure 1: Physical insight that provides explanation of phenomenon that occurred in different HNS.

In this thesis, it has been demonstrated that in a mixed colloid of MNP and SQD, the properties of hybrid samples prepared by self-organized growth is decided by the variation in number density of hybrid vs unattached particles and not due to a continuous change in the interaction between them. This allowed structural characterization of self-organized HNS by optical measurements itself. These studies are crucial for the advancement in the area of colloidal self-organization. Using this method, a semiconductor quantum dot could be placed between two Ag nanospheres in the hot-spot region. This assembly technique can be extended to other noble metals and semiconductor quantum dots capped with thiols. This is an important step for the applications of hot-spot. The underlying mechanism of ultrafast response in HNS is modelled using electromagnetic theory, two-temperature model and hot-electron transport. Each of these variation plays an important role depending on the structure of Ag-CdTe hybrid. To quantify the hot-electron transport in HNSs, a method is developed that estimates the number of electrons hopping between the two constituents of the hybrid at ultrafast time scales. This provides a way to optimize the design of a metal-semiconductor hybrid system for optoelectronic and catalytic applications. Photoluminescence (PL) spectroscopy on this HNS revealed that PL kinetics depends on the excitation photon energy when the PL emission spectrum overlaps with plasmom peak. This opens up possibility of designing a material that is well suited for light-emitting devices. In summary, this thesis offers a physical insight into a problem regarding the coupling mechanism in HNS at different time scales and energies while providing an approximate quantitative solution that can be extented to other HNS system.